CMS Draft Analysis Note

The content of this note is intended for CMS internal use and distribution only

November 17, 2008
Archive Id:
Archive Date:

Transverse Momentum Distribution within Jets in pp Collisions at 14 TeV

Pelin Kurt[1], Anwar Bhatti[2], and Marek Zielinski[3]

[1] Cukurova University, Adana, Turkey
[2] The Rockefeller University, New York NY 10065
[3] University of Rochester, Rochester NY 14627

DRAFT

Abstract

The CMS (Compact Muon Solenoid) detector will observe high transverse momentum jets produced in the final state of proton-proton collisions at the center of mass energy of 14 TeV. These data will allow us to measure jet shapes, defined as the fractional transverse momentum distribution as a function of the distance from the jet axis. Since jet shapes are sensitive to parton showering processes they provide a good test of Monte Carlo event simulation programs. In this note we present a study of jet shapes reconstructed using calorimeter energies where the statistics of all distributions correspond to a CMS data set with 10 pb^{-1} of integrated luminosity. We compare the predictions of the Monte Carlo generators PYTHIA and HERWIG++.

DRAFT

Contents

1 Introduction . . . 2
2 CMS Detector . . . 2
3 Jet Clustering Algorithms . . . 3
4 Data Samples . . . 5
5 Data Selection . . . 5
5.1 Missing E_T Significance . . . 6
5.2 Event Electromagnetic Fraction . . . 6
5.3 Event Charge Fraction . . . 6
6 Multiplicity of Jet Constituents . . . 6
7 p_T Distributions of Particles, Tracks and Towers In a Jet . . . 6
8 Definition of Jet Shapes . . . 11
9 Raw Jet Shapes . . . 12
10 Jet Shape Corrections . . . 12
11 Corrected Jet Shapes . . . 13
12 Sensitivity of Jet Shapes to Underlying Event Tunes . . . 13
13 Jet Shapes from ALPGEN Samples . . . 13
14 Quark and Gluon Jet Shapes . . . 16
15 Systematic Uncertainties . . . 16
15.1 Jet Energy Scale . . . 20
15.2 Jet Fragmentation . . . 20
15.3 Non-linearity of Calorimeter Response and Transverse Shower Profile . . . 21
16 Monte Carlo Estimate of Systematics Due to Calorimeter Response . . . 25
16.1 Transverse Showering Spread . . . 26
16.2 Linearity of the Calorimeter Response . . . 27
17 Conclusions . . . 27
A Appendix: Figures for All Jet P_T Bins . . . 35

DRAFT

1 Introduction

The transverse momentum profile of a jet, or jet shape [1, 2], is sensitive to multiple parton emissions from the primary outgoing parton and provides a good test of the parton showering description of Quantum Chromodynamics (QCD), the theory of strong interactions. Historically the jet shape has been used to test perturbative QCD (pQCD) α_s^3 calculations [3, 4]. These leading order calculations, with only one additional parton in a jet, showed good agreement with the observed jet shapes.

While confirming the validity of pQCD calculations, jet shape studies also indicated that jet clustering, underlying event contribution and hadronization effects must be considered. These effects can be modeled accurately within the framework of full-event generators. Current Monte Carlo (MC) event generators use pQCD inspired parton shower models, in conjunction with hadronization and underlying event models, to generate final state particles. MC generators are used extensively to model signal and background events in most analyses at hadron colliders. Jet shapes can be used to tune phenomenological parameters in these MC generators.

QCD predicts broader gluon jets than quark jets. The structure of quark and gluon jets can be investigated by comparing measurements of the jet shapes in different processes enriched with either quark or gluon initiated jets in the final state. Previously, jet shapes have been measured in $p\bar{p}$ collisions at Tevatron and ep collisions at HERA [3–7].

In this paper, we present a study of jet shapes at particle and calorimeter levels in the central region of the CMS detector and compare the results obtained with various MC generators. The sensitivities of jet shapes to the underlying event (UE) model and to the flavor of the initiating parton are also explored.

2 CMS Detector

The Compact Muon Solenoid (CMS) detector is a multipurpose apparatus at the Large Hadron Collider (LHC) at CERN. The CMS has a cylindrical structure covering almost 4π of angular phase-space in order to detect a large fraction of particles produced in a pp collision. It contains subsystems which are designed to measure energies and momenta of photons, electrons, muons, and hadrons [8–10].

The central hadronic section (HCAL) is made of brass and scintillators while the electromagnetic section (ECAL) comprises lead tungstate crystals ($PbWO_4$). The response of the calorimeter to photons is linear versus incident energy, while the response to hadrons depends strongly on the incident energy. The difference in response of the calorimeter to photons and hadrons leads to a nonlinear energy response of the calorimeter to jets.

The coordinate system used at CMS is defined as follows: the x-axis points horizontally outside the LHC ring, the y-axis points upwards, and the z-axis is aligned with the nominal beam direction. The azimuthal angle is ϕ and the polar angle is θ. The transverse momentum P_T is defined as a projection of a particle momentum P on the xy-plane, $P_T = P \cdot \sin\theta$, and the "transverse energy" as $E_T = E \cdot \sin\theta$. The rapidity is defined as $y = \frac{1}{2}\log\frac{E+P_Z}{E-P_Z}$, where E denotes the energy and P_Z is the component of the momentum along the z direction. The pseudo-rapidity is defined as $\eta = -\ln[\tan\frac{\theta}{2}]$.

DRAFT

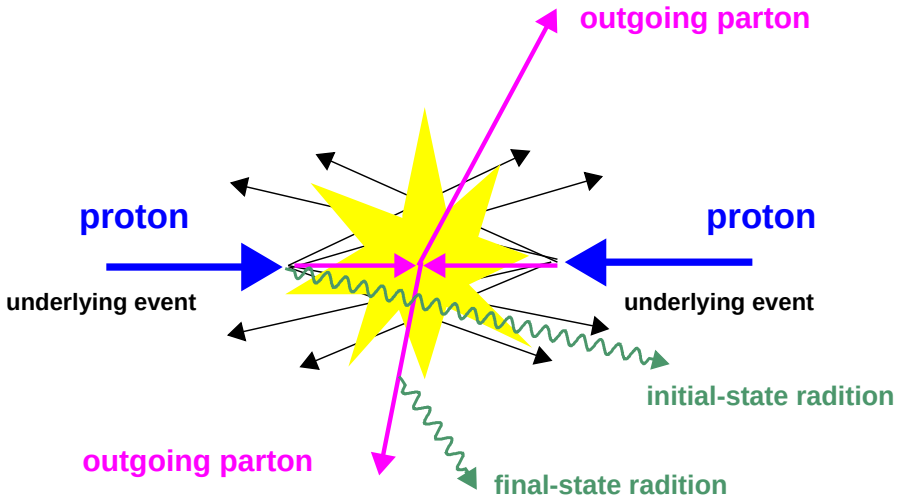

Figure 1: Illustration of a typical proton-proton two parton hard scattering event including initial and final state radiation and beam-beam remnants.

3 Jet Clustering Algorithms

In high energy interactions partons are produced in the final state with large transverse momenta as a result of the hard scattering process illustrated in Figure 1. Partons outgoing from the interaction point produce parton showers and subsequently partons from these showers combine to form hadrons which are color singlets which interact in the detector (see Figure 2). Since the transverse energies involved in the hadronization process are much smaller than the hard scattering energies, the final state particles are collimated around the direction of the original parton. These streams of particles are called jets. Jet clustering algorithms are used to associate particles to a particular jet. Direction and energy of a jet are related to the direction and energy of the original parton. E-scheme [11] is used to calculate the 4-momentum of the jet from the 4-momenta of the individual particles. In the E-scheme, constituents are simply added as four-vectors, producing massive jets.

Two main jet reconstruction algorithms being used in CMS are the inclusive k_T jet algorithm [12] and a recent algorithm SISCone (Seedless Infrared Safe Cone) [13]. The cone jet algorithm, SISCone, groups the input objects together based on their distance in (y, ϕ) space, and the determination of the jet quantities is done at the end of the jet finding. The inclusive k_T algorithm iteratively merges input objects into final jets and so the jet kinematic quantities, the jet direction and energy, are calculated directly during the clustering.

In this analysis, the SISCone algorithm has been used to reconstruct jets at particle and calorimeter levels with $R = 0.7$, where $R = \sqrt{(\Delta y)^2 + (\Delta\phi)^2}$ and Δy and $\Delta\phi$ specify the cone dimensions in rapidity and azimuth respectively.

DRAFT

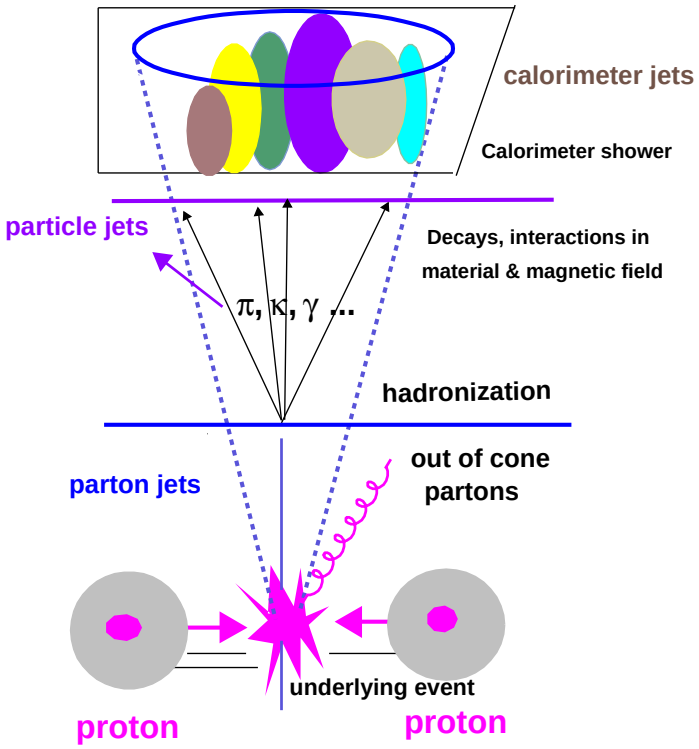

Figure 2: Schematic of jet evolution and detection. Parton jets hadronize into particle jets which interact in the calorimeter forming calorimeter jets.

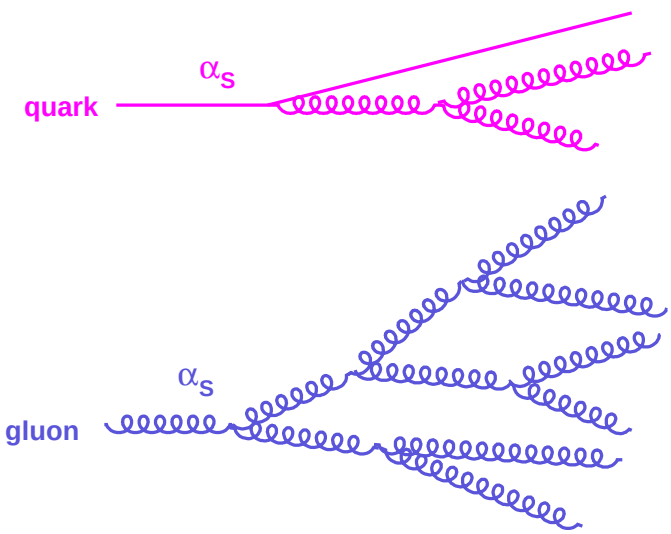

Figure 3: Examples of the structure of quark and gluon initiated jets

4 Data Samples

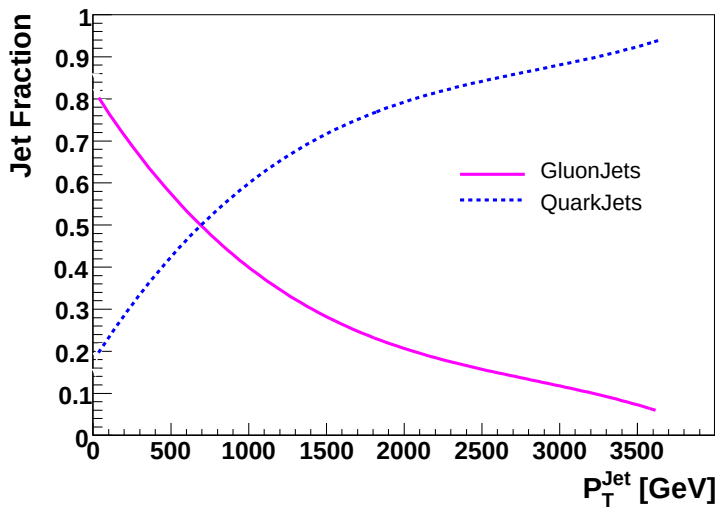

Figure 4: Fraction of the quark or gluon initiated jets as a function of jet P_T for $|\eta| < 1$ (from PYTHIA DWT).

QCD dijet events were generated with PYTHIA in $15 < \hat{p}_T < 5000$ GeV range, ALPGEN in $20 < \hat{p}_T < 5600$ GeV and HERWIG++ in $50 < \hat{p}_T < 7000$ GeV, where $\hat{p}_T$ refers to the transverse momentum in the hard-scatter of partons. Results of this study extend up to jet P_T= 1.4 TeV which is the approximate sensitivity limit for a 10 pb^{-1} integrated luminosity sample of LHC collisions at 14 TeV. Expected number of events for 10 pb^{-1} of integrated luminosity is summarized in Table 1 for different High Level Trigger (HLT) thresholds.

We used calorimeter energy deposits to explore the largest P_T range possible. Tracks can be used to measure jet shapes at low and medium P_T, and to help estimate systematic uncertainties. The calorimeter-jet P_T was corrected using CMS standard jet energy corrections [14]. Calorimeter towers and reconstructed tracks were required to satisfy the E_T=0.5 GeV threshold while no such threshold was applied to particles when reconstructing generator-level jets.

Generated jets were simulated and digitized with CMSSW_1_6_12 for PYTHIA and ALPGEN and CMSSW_1_8_4 for HERWIG++ samples. ALPGEN generated events also were used to verify the PYTHIA correction factors using a different data set.

Figure 4 shows the quark-gluon jet fraction as a function of jet P_T in the PYTHIA samples. It was determined by matching the two leading-P_T jets in the event with the two outgoing partons from the hard scatter within a distance $\Delta R < 0.5$ in (y, ϕ) space.

5 Data Selection

For data, we will use events with one and only one vertex to minimize contribution from pile-up, and to remove some non-physics events.

Clean-up selections will be used to reject cosmic ray events and non-physics events such as beam halo and catastrophic noise. In particular, we plan to use cuts on missing E_T relative to total E_T in the event, and fractions of total jet P_T detected in the electromagnetic calorimeter and carried by the associated charged tracks. These cuts are expected to be fully efficient for

DRAFT

QCD dijet events and are discussed below. The values of the cuts will be determined by looking at the data.

5.1 Missing E_T Significance

This cut will be used to remove cosmic rays and detector related beam background events. Figure 5 shows the distribution for $\not{E}_T/\sqrt{\sum E_T}$ in QCD events. It indicates that one can safely require $\not{E}_T/\sqrt{\sum E_T}$ <5.

5.2 Event Electromagnetic Fraction

In the preselection of data, to distinguish real jet events from fake events, the Event Electromagnetic Fraction (F_{EM}) cut can be applied. F_{EM} distribution, shown in Figure 6, is defined as

$$F_{EM} = \frac{\sum_{j=1}^{N_{jet}} P_T^j \cdot f_{EM}^j}{\sum_{j=1}^{N_{jet}} P_T^j} \tag{1}$$

for jets within the acceptance of the electromagnetic calorimeter, $|\eta| < 3$. f_{EM}^j is the jet electromagnetic fraction of the jet j. Normally, events are expected to have the electromagnetic fraction between 0 and 1, but not close to the edges. Non-physics energy, for example energy from a halo muon, may be deposited either in the hadronic or in the electromagnetic calorimeter only, and thus have F_{EM} either close to 0 or 1.

5.3 Event Charge Fraction

The Event Charge Fraction is defined as the sum of the P_T of the tracks associated to the jet for jets within $|y| < 1.7$. The event charge fraction is formulated as

$$F_{ch} = \frac{1}{N_{jet}} \sum_j \frac{(\sum_i^{tracks} P_{Ti})^j}{P_T^j} \tag{2}$$

where for every jet the sum runs over the tracks that can be matched in (y, ϕ) space to that jet; the average over the charge fraction is taken for all jets within $|y| < 1.7$. Event charge fraction distribution for good events is also shown in Figure 6. Background events from beam halo or cosmic rays are expected to have $F_{ch} = 0$, and can be removed by requiring $F_{ch} > 0$, with minimal loss in efficiency.

6 Multiplicity of Jet Constituents

Figure 7 summarizes the mean multiplicities of particles, tracks and calorimeter towers in a jet as a function of jet P_T. As expected, they increase logarithmically with increasing jet P_T. Figures 8, 9 and 10 present the multiplicity distributions for particles, calorimeter towers and tracks in a jet, respectively, in selected P_T bins.

7 p_T Distributions of Particles, Tracks and Towers In a Jet

P_T distributions of particles, tracks and towers in a jet are shown in Figures 11, 12 and 13, respectively. These distributions become harder with increasing jet P_T.

DRAFT

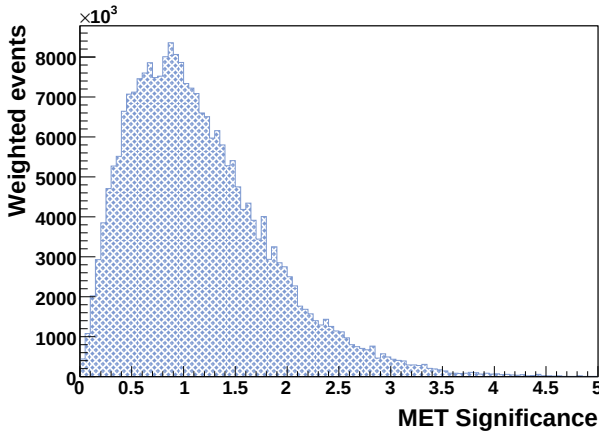

Figure 5: Distribution of MET significance $\not{E}_T$ / $\sqrt{\sum E_T}$ in QCD events.

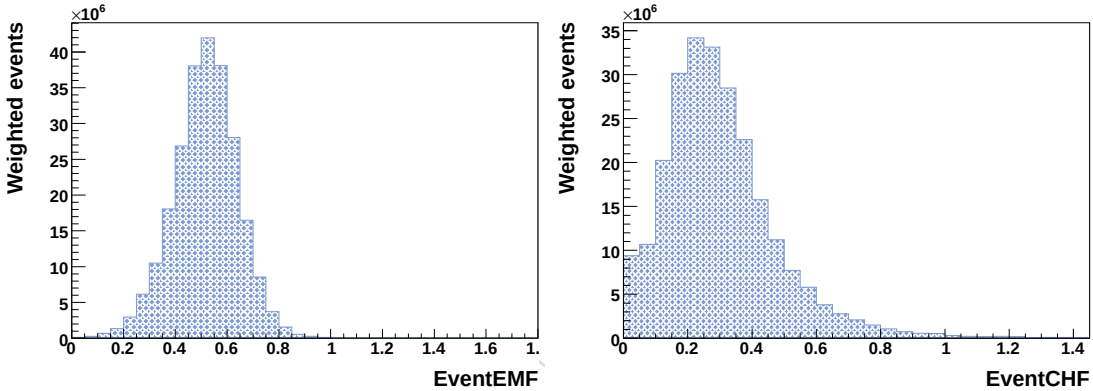

Figure 6: Event Electromagnetic Fraction and Event Charge Fraction distributions in QCD events.

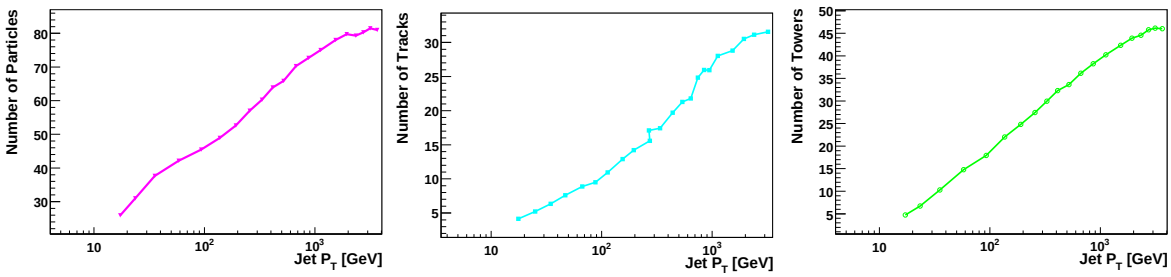

Figure 7: Mean multiplicities of particles, tracks and towers in a jet as a function of jet P_T. Statistical errors are too small to be visible.

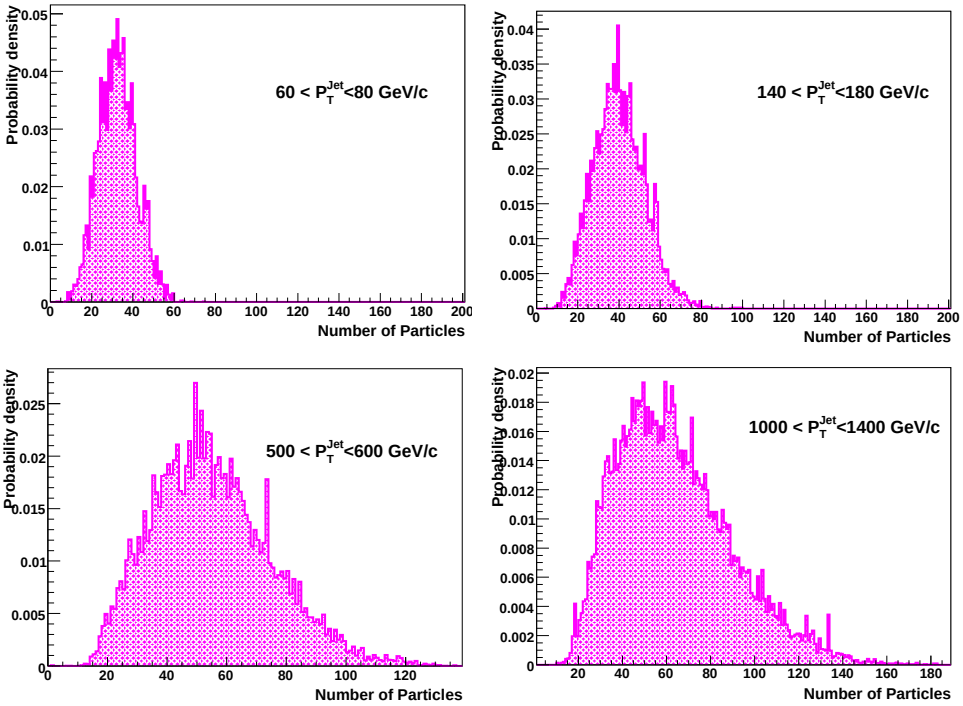

Figure 8: Multiplicity distributions of particles in a jet for selected P_T bins.

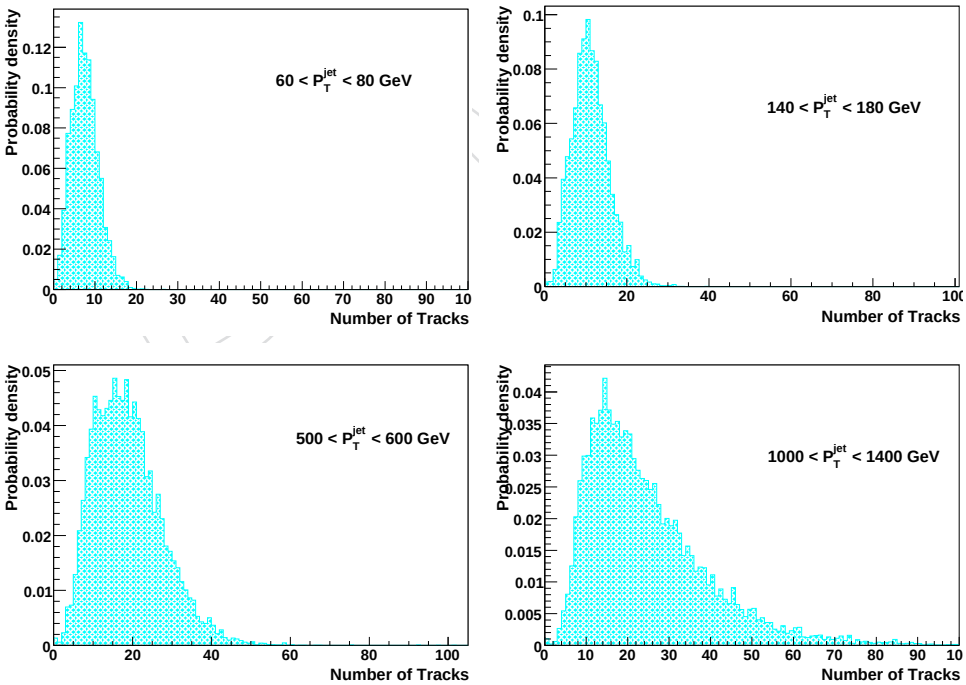

Figure 9: Multiplicity distributions of tracks in a jet for selected jet P_T bins.

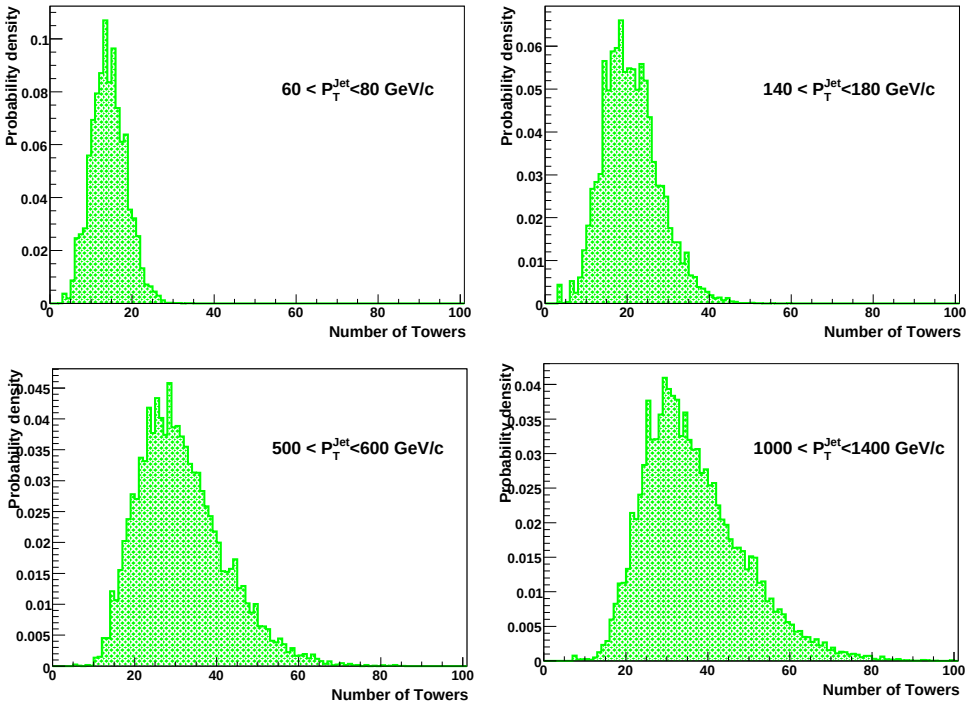

Figure 10: Multiplicity distributions of calorimeter towers in a jet for selected jet P_T bins.

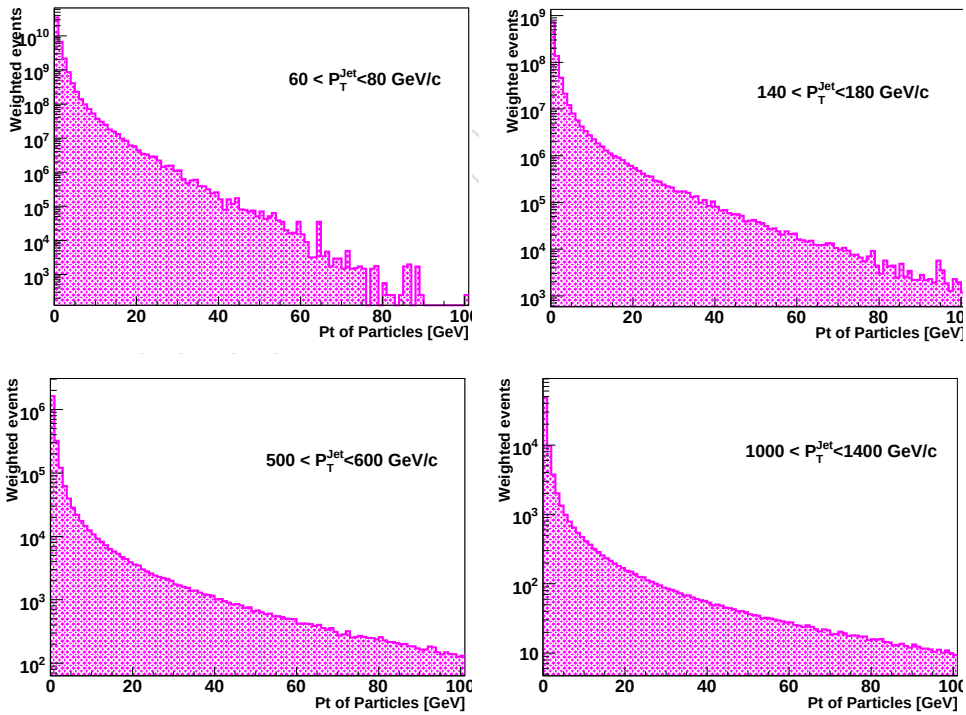

Figure 11: p_T distributions of particles in a jet for selected jet P_T bins.

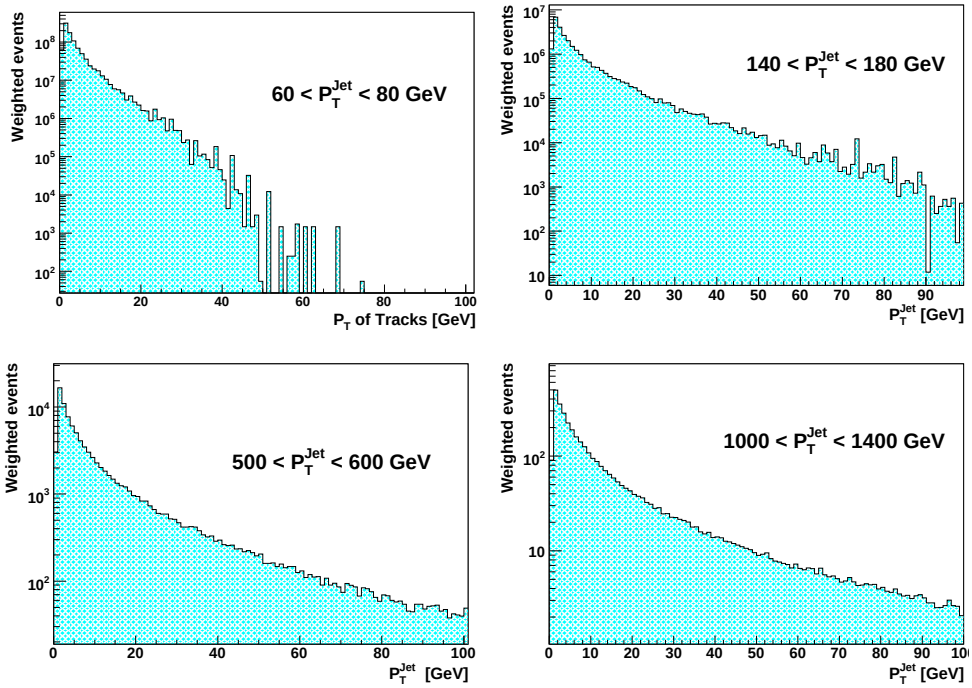

Figure 12: p_T distributions of tracks in a jet for selected jet P_T bins.

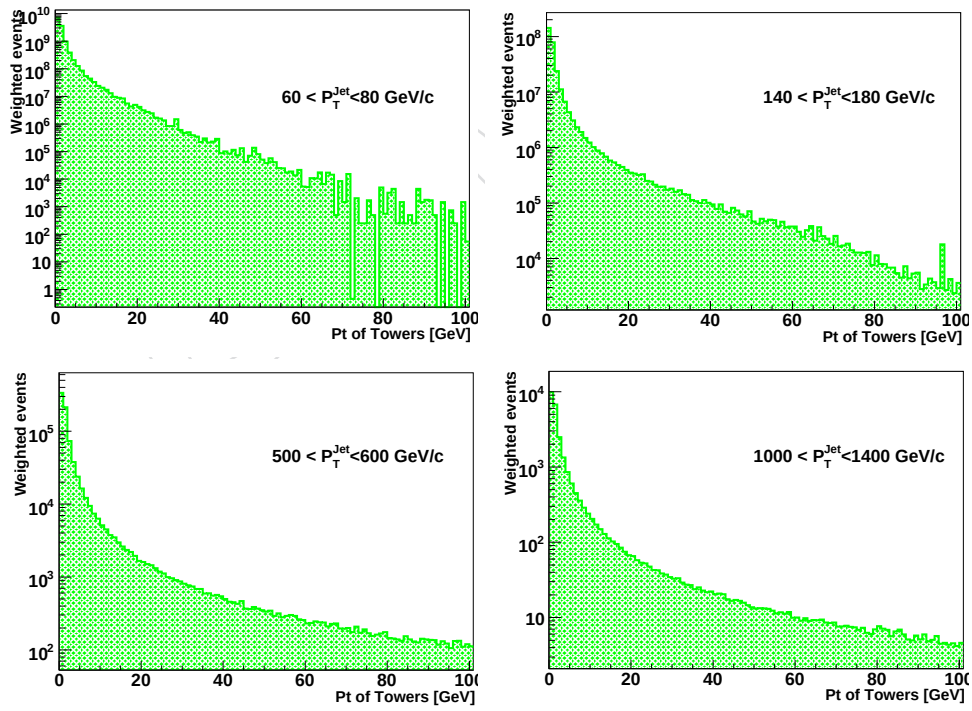

Figure 13: p_T distributions of calorimeter towers in a jet for selected jet P_T bins.

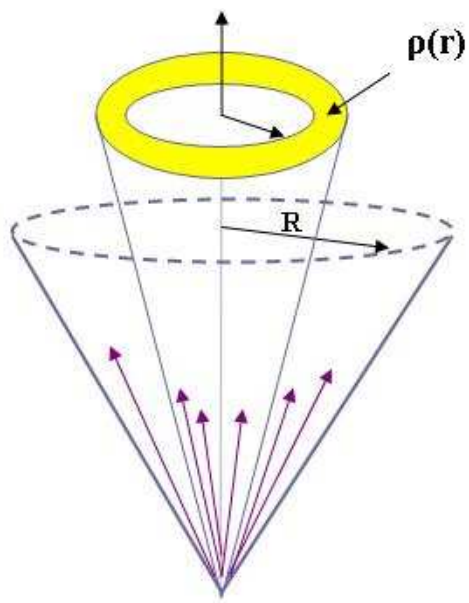

Figure 14: Definition of the differential jet shape, $\rho(r)$.

8 Definition of Jet Shapes

The jet shape is defined as the average fraction of the jet transverse momentum within a cone of a given size r around the jet axis, $r = \sqrt{(y_i - y_j)^2 + (\phi_i - \phi_j)^2}$, where i refers to the particle, calorimeter tower or track, and j to the jet. Jet shapes can be studied by using an integrated or a differential distribution. In the present study only two leading jets within $|y| < 1$ are considered per event. All particles and calorimeter towers within distance $R = \sqrt{(\Delta y)^2 + (\Delta\phi)^2} = 0.7$ from the jet axis are used . This large cone size ensures that most of the parent parton energy is included in the jet.

The differential distribution, $\rho(r)$, is illustrated in Fig. 14. It is defined as the fraction of the jet transverse momentum contained inside an annulus of inner radius $r - \delta r/2$ and outer radius $r + \delta r/2$ around the jet axis, such that $0 \leq r \leq R$:

$$\rho(r) = \frac{1}{\delta r} \frac{1}{N_{jet}} \sum_{jets} \frac{P_T(r - \delta r/2, r + \delta r/2)}{P_T(0, R)}. \tag{3}$$

Above, N_{jet} denotes the total number of selected jets. In the numerator P_T is the sum of all particles, tracks or towers in the distance range $(r - \delta r/2, r + \delta r/2)$ from the jet axis. In the denominator, $P_T(0, R)$ is the scalar sum of transverse momenta of all the particles, tracks or towers within the cone of radius R.

Similarly, the integrated jet shape (see Figure 15), $\psi(r)$, is defined as:

$$\psi(r) = \frac{1}{N_{jets}} \sum_{jets} \frac{P_T(0, r)}{P_T(0, R)} \tag{4}$$

where $P_T(0, r)$ is the scalar sum of transverse momenta of all particles within the distance r from the jet axis with $\psi(r = R) \equiv 1$.

DRAFT

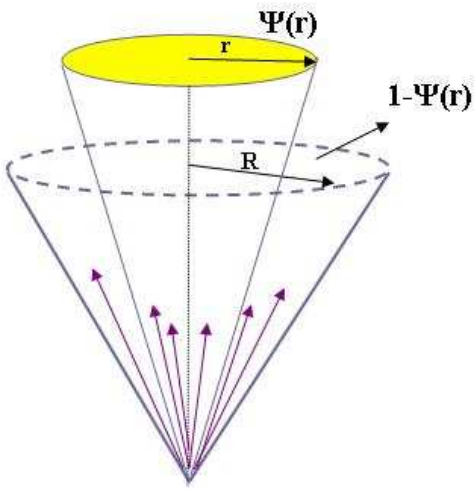

Figure 15: Definition of the integrated jet shape, $\psi(r)$.

To calculate the jet shapes, we made histograms of transverse momentum in the appropriate bin of r divided by the transverse momentum in the cone $R = 0.7$. The mean value of these histograms was then plotted as function of r. The statistical uncertainty on each point was calculated as $rms/\sqrt{N}$, using the rms of the corresponding histogram and the number N of expected jets in the bin for luminosity of 10 pb^{-1}. For the integrated shape the uncertainties at different r points are partially correlated. We used 2000 events in each $\hat{p}_T$ bin. The samples have been combined according to the cross section weights.

9 Raw Jet Shapes

Figure 16 shows the differential jet shapes for PYTHIA events at generated and calorimeter levels (see Figures 43, 44 and 45 for all P_T bins). Most of the momentum is concentrated at the small radius region. Jet shapes become narrower with the increasing P_T of the jet. Underlying event contribution as the fraction of jet P_T is larger at low P_T and at large radius. Integrated jet shapes in Figure 17 become narrower with increasing P_T for both particle and calorimeter levels (see also Figures 46 and 47).

10 Jet Shape Corrections

Due to various detector effects, the measured (calorimeter) jet shapes are different than the true (particle) jet shapes. Due to the magnetic field of CMS, charged particles with $P_T < 0.9$ GeV do not reach the calorimeter. In addition showers from particles interacting with the detector material spread their energy over many calorimeter towers. The measured jet shapes must be corrected for these detector effects. Correction factors were determined as a function of distance from the jet axis using MC events before and after the CMS detector simulation. For this approach to be valid, the MC simulation must describe the calorimeter response accurately. As discussed in Section 15 we plan to cross-check this assumption using tracking information. The corrections have been determined using unmatched jets and are applied as a function of distance from the jet axis.

DRAFT

The correction factors $D(r)$ and $I(r)$ for differential and integrated jet shapes are defined in Equations 5 and 6, respectively:

$$D(r) = \rho_{MC}^{PARTICLE}(r)/\rho_{MC}^{CAL}(r) \tag{5}$$

$$I(r) = \psi_{MC}^{PARTICLE}(r)/\psi_{MC}^{CAL}(r) \tag{6}$$

where calorimeter towers and generated particles have been used to reconstruct differential $\rho_{MC}^{CAL}(r)$, $\rho_{MC}^{PARTICLE}(r)$ and integrated jet shapes $\psi_{MC}^{CAL}(r)$, $\psi_{MC}^{PARTICLE}(r)$ in different bins of jet P_T.

Measured calorimeter jet shapes are then used to determine the corrected differential jet shapes $\rho^{corrected}(r) = D(r) \cdot \rho^{CAL}(r)$ and integrated jet shapes $\psi^{corrected}(r) = I(r) \cdot \psi^{CAL}(r)$.

The correction factors $D(r)$ in Figure 18 (see also Figures 48 and 49) do not show a significant dependence on jet P_T in the region $r < 0.5$. They vary between 0.6 and 1.3 as a function of r, and between 1.3-2 for the region $r > 0.5$. The correction factors for integrated jet shapes in Figure 19 (see also Figures 50 and 51) vary from 0.9 to 1.06 for all radius and P_T bins. For the integrated distributions, the correction factors do not have a strong dependence on jet P_T.

11 Corrected Jet Shapes

The corrected differential and integrated jet shapes are shown in Figures 16 and 17 (see also Figures 43, 44, 45 and Figures 46, 47). Close to the jet axis, the jet shape is dominated by collinear gluon emission, whereas at large distance from the jet axis, the jet shape reflects large angle gluon emissions, which can be calculated perturbatively. The jet shape $\psi(r)$ increases faster with r for jets at larger P_T indicating that these jets are more collimated.

12 Sensitivity of Jet Shapes to Underlying Event Tunes

The energy from the underlying event (UE) contributes to jets and impacts the jet shapes. To determine the sensitivity of jet shapes to the UE contribution, event samples were generated using PYTHIA DW which has a smaller UE contribution than PYTHIA with tune DWT, which is the CMS default setting [15]. These tunes are different extrapolations to $\sqrt{s}$=14 TeV of the same tune at the Tevatron energy $\sqrt{s}$=1.8 TeV. The jet shapes for PYTHIA DWT and PYTHIA DW are shown in Fig. 20 (see also Figure 52) for the differential jet shapes and in Figure 21 (see also Figure 53) for the integrated jet shapes. At low jet P_T, one can observe the difference in jet shapes due to the UE contribution.

13 Jet Shapes from ALPGEN Samples

We tested the corrections derived from PYTHIA on an independent sample generated using ALPGEN [16]. For this sample the parton showering and hadronization models are the same as used by PYTHIA. Figure 22 shows the differential jet shapes at particle and corrected calorimeter levels for ALPGEN multi-jet samples (see also Figures 54 and 55). Figure 23 shows the corrected integrated jet shapes (see also Figures 56 and 57). Correction factors determined from PYTHIA DWT events work reasonably well for ALPGEN, as expected since the parton showering and hadronization is done by PYTHIA.

DRAFT

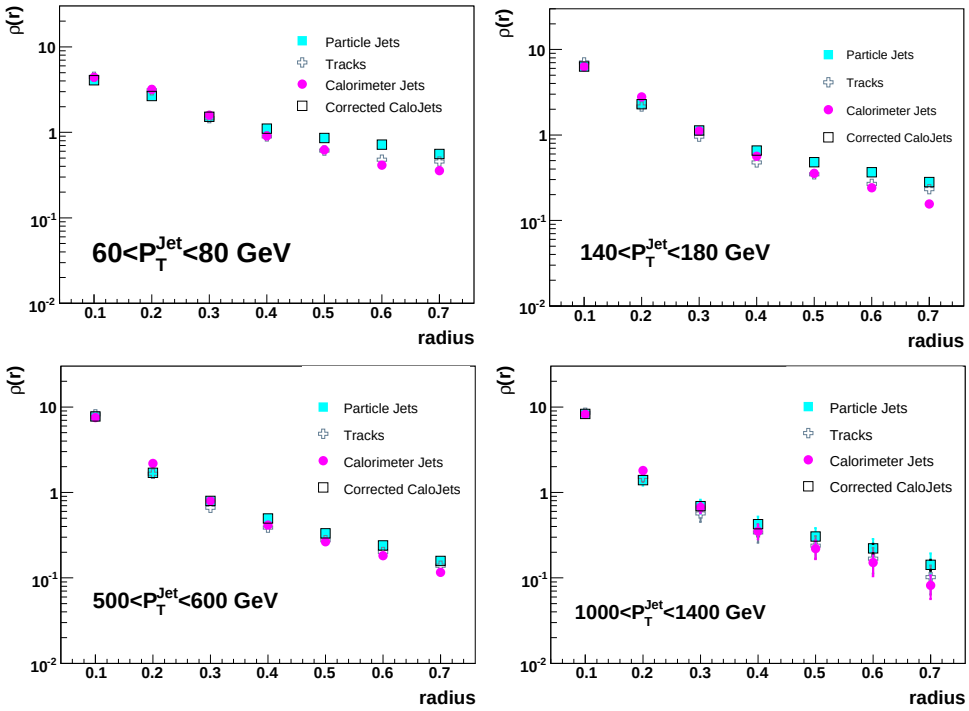

Figure 16: Differential jet shapes for selected P_T bins. Statistical errors are included.

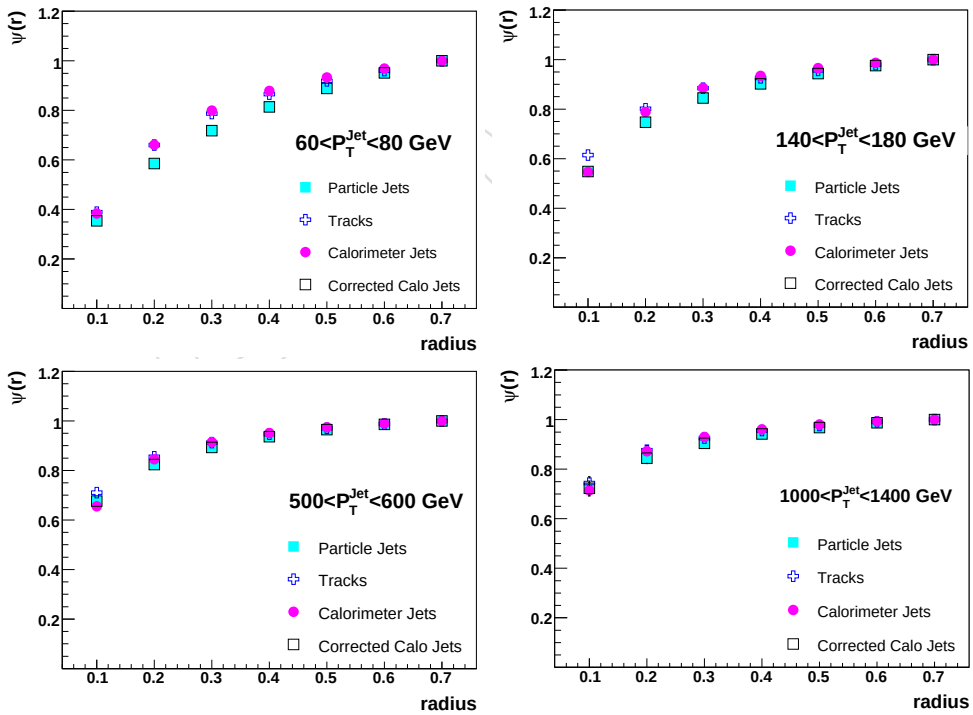

Figure 17: Integrated jet shapes for selected P_T bins. Statistical errors are included.

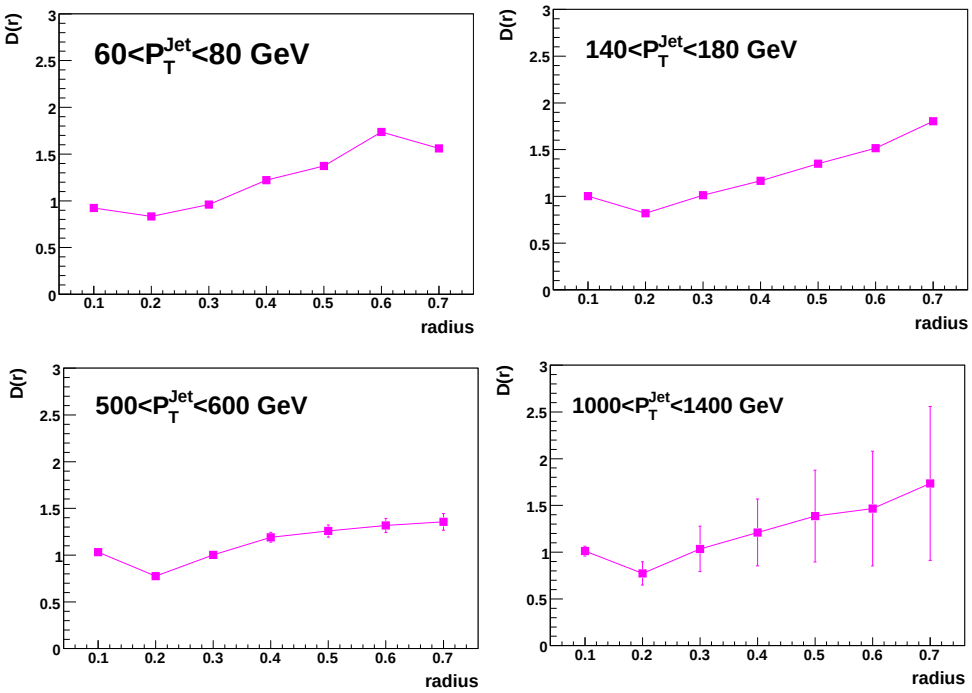

Figure 18: Correction factors for differential jet shapes for selected P_T bins. Statistical errors are included.

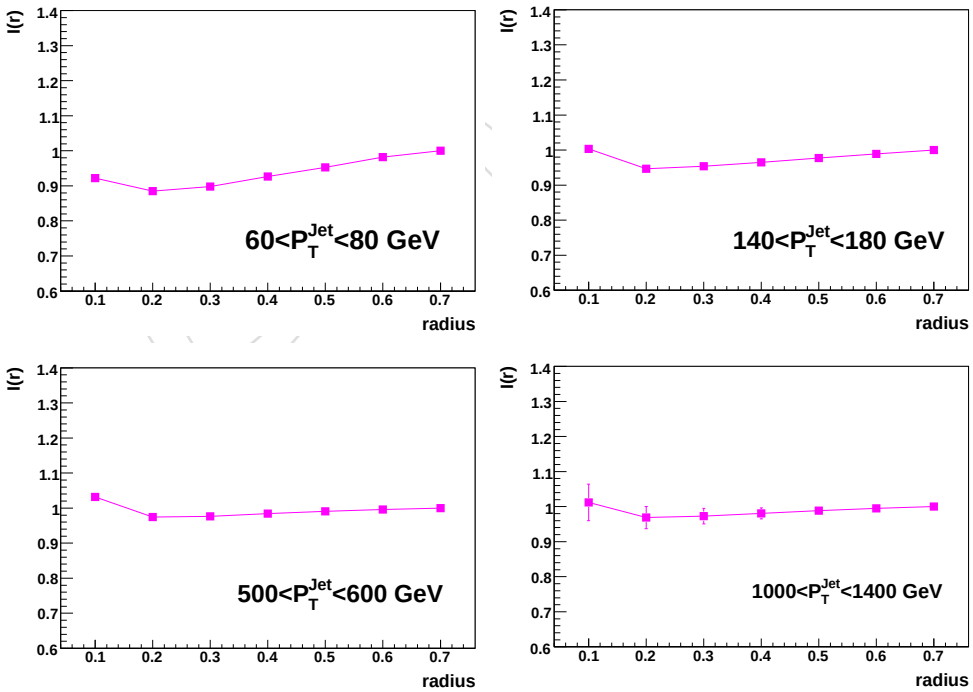

Figure 19: Correction factors for the integrated jet shapes for selected P_T bins. Statistical errors are included.

14 Quark and Gluon Jet Shapes

Jet shapes are sensitive to quark and gluon jet contributions. Using parton information from PYTHIA we classified hadron level jets based on matching within $\Delta R < 0.5$ in (y, ϕ) space. The MC predicts that the measured jet shapes are dominated by contributions from gluon initiated jets at low jet P_T while contributions from quark initiated jets become important at high jet P_T. Figures 24 and 25 compare differential and integrated jet shapes for quarks and gluons with simulated data (see also Figures 58, 59, 60 and 61). As expected, quark jets are narrower than the gluon jets due to the coupling strengths for gluon emission which depend on the color factors C_F=4/3 for radiating quarks and C_A=3 for gluons. Fraction of gluon jets in the sample is higher at lower jet P_T.

Figure 26 presents the P_T fraction contained in the jet cone $R = 0.7$ lying outside a cone of r=0.2 as function of the jet P_T. Reconstructed calorimeter jets from the full CMS Monte Carlo simulation are compared with parton shower MC predictions for quark and gluon jets. Tables 2, 3 and 4 provide details of the calculation of statistical and systematic uncertainties for $1 - \psi(r = 0.2)$ in all P_T bins.

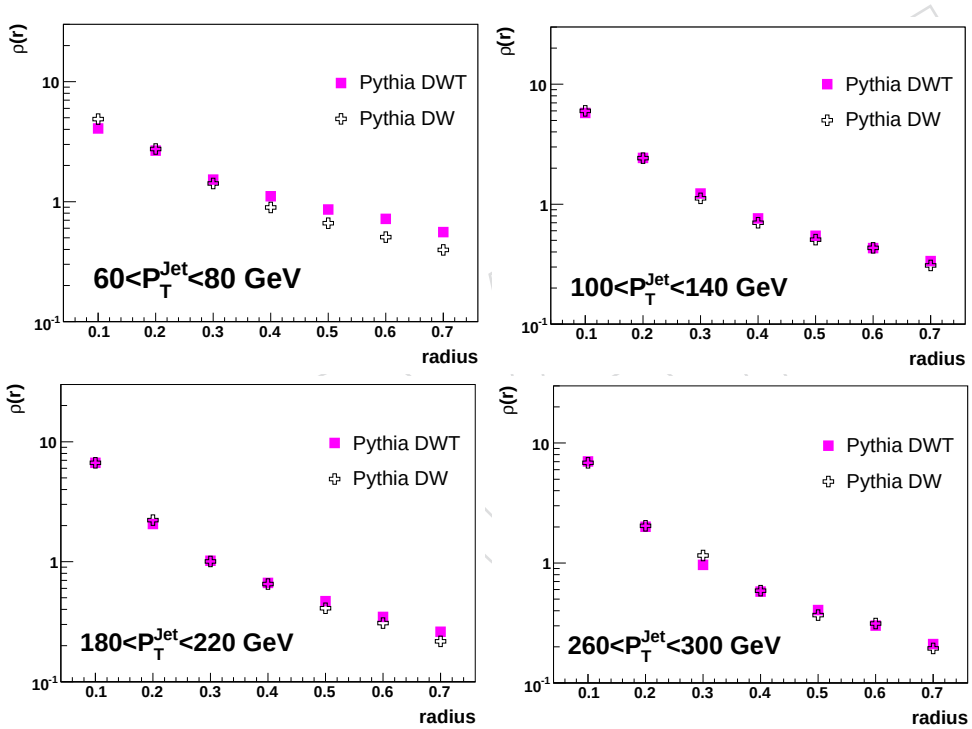

Figure 20: Comparison of differential jet shapes for PYTHIA tunes DW and DWT at particle level in selected P_T bins. Statistical errors are included.

15 Systematic Uncertainties

The main sources of systematic uncertainties include:

- Jet energy scale
- Transverse shape of calorimeter showers
- Non-linearity of calorimeter response
- Jet fragmentation

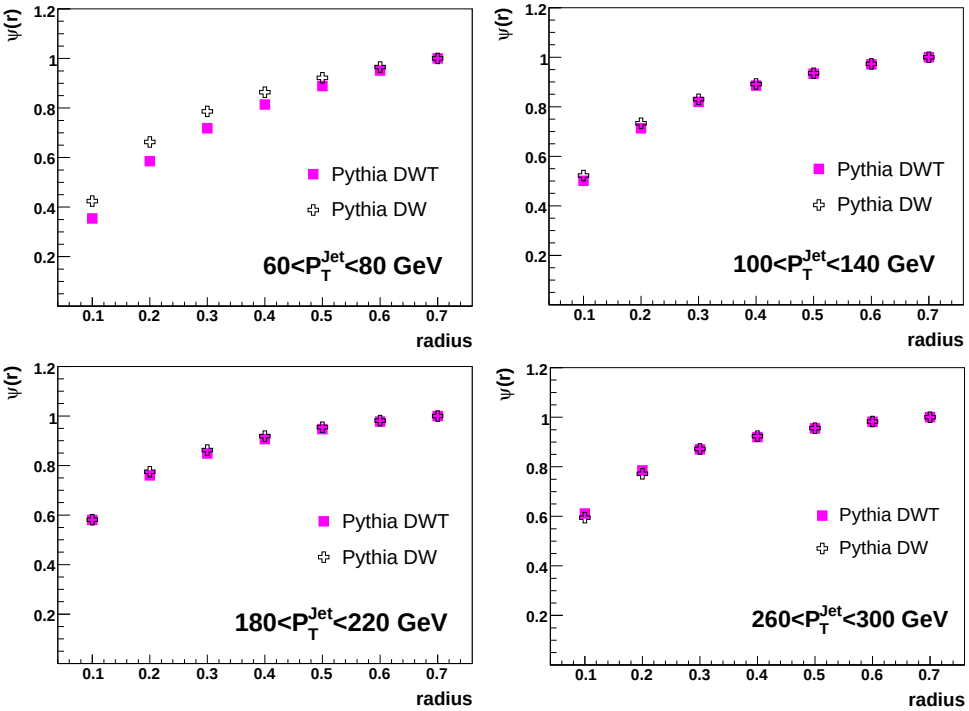

Figure 21: Comparison of integrated jet shapes for PYTHIA tunes DW and DWT at particle level in selected P_T bins. Statistical errors are included.

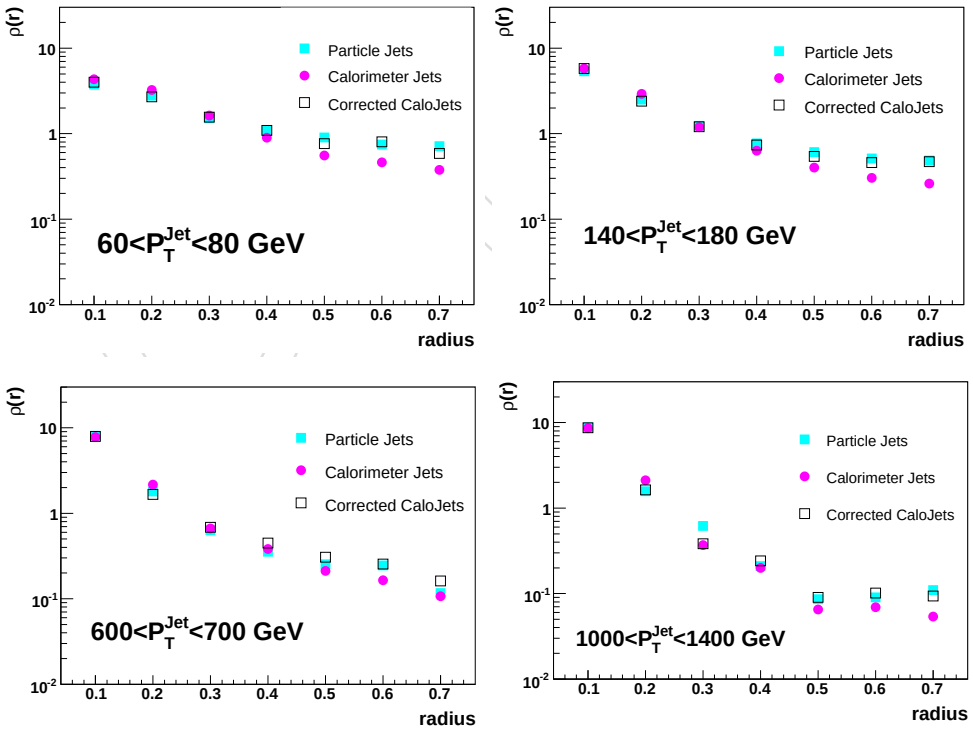

Figure 22: Differential jet shapes for selected P_T bins in multi-jet samples generated with ALPGEN. Calorimeter jets are corrected using corrections derived from PYTHIA samples. Statistical errors are included.

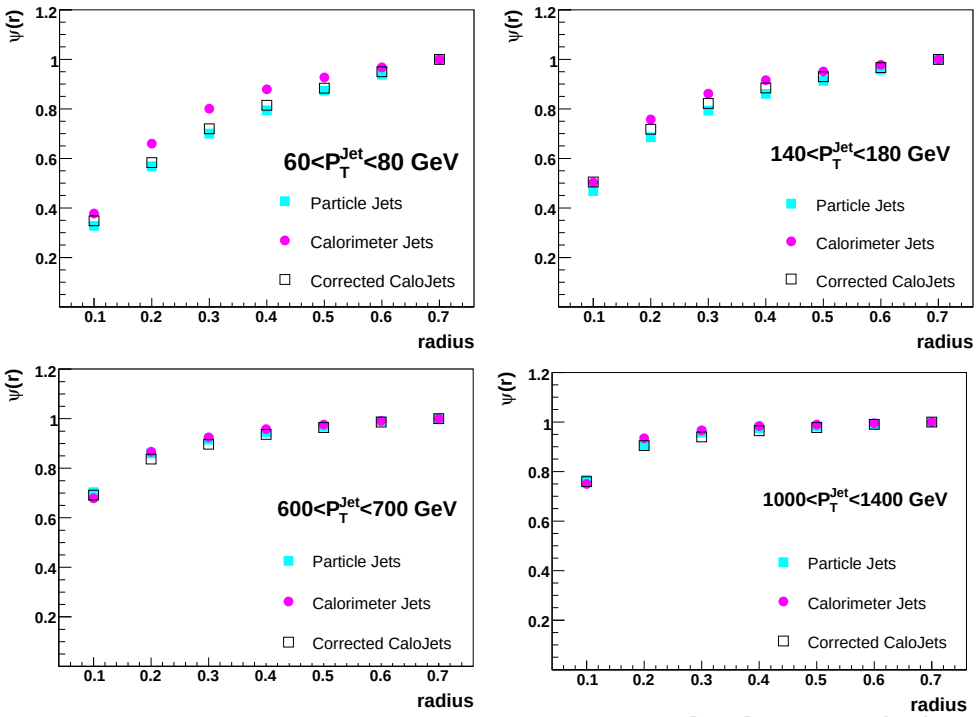

Figure 23: Integrated jet shapes for selected P_T bins in multijet samples generated with ALPGEN. Calorimeter jets are corrected using corrections derived from PYTHIA samples. Statistical errors are included.

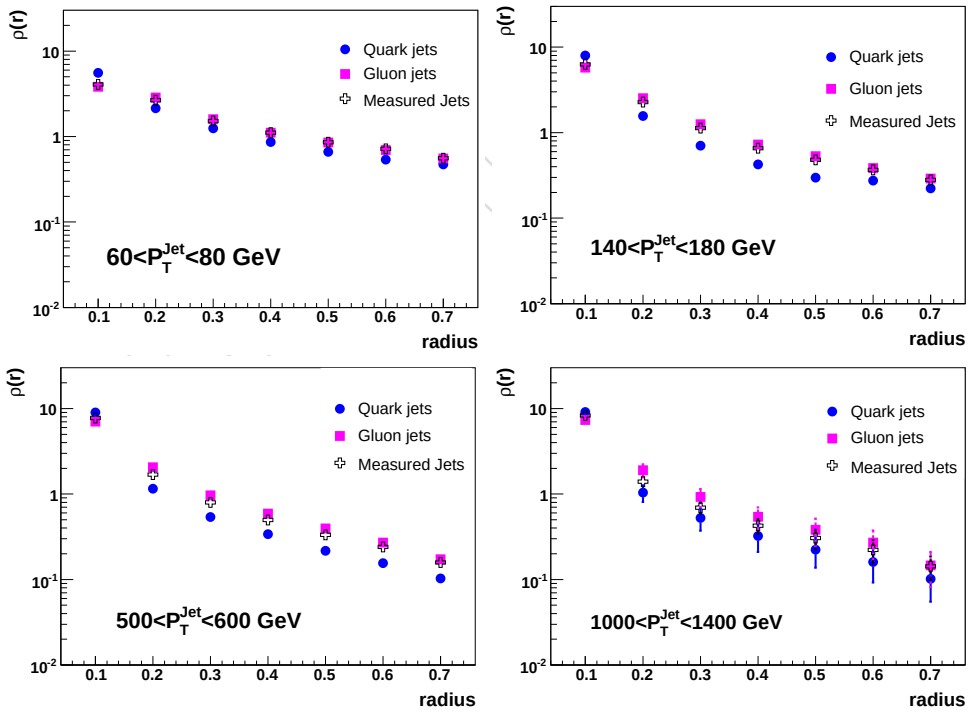

Figure 24: Comparison of quark and gluon differential jet shapes to simulated data in selected P_T bins. Statistical errors are included.

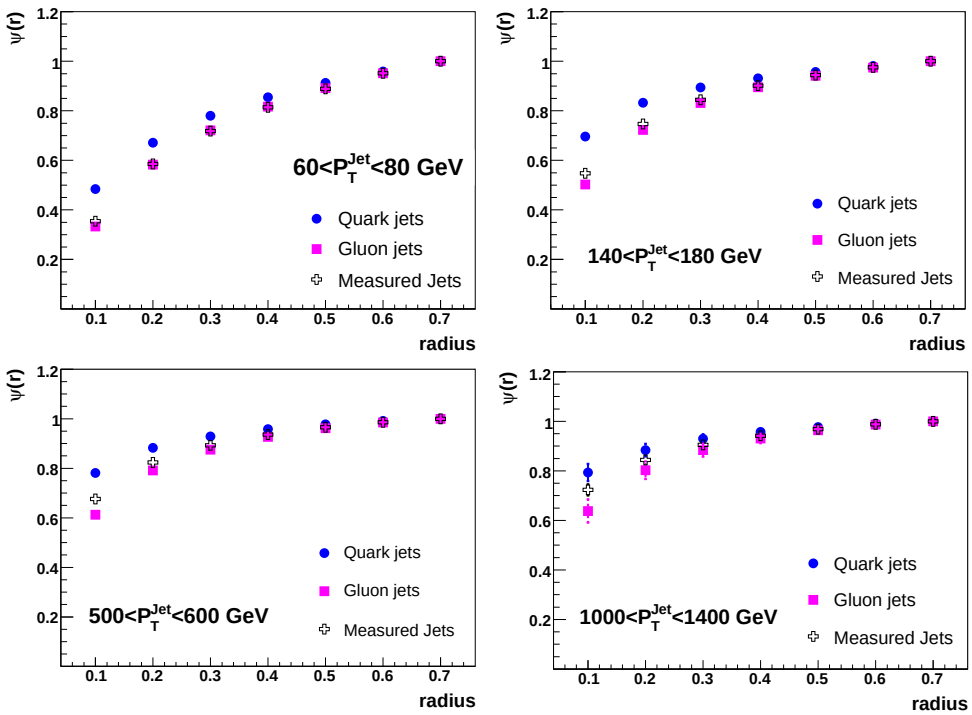

Figure 25: Comparison of quark and gluon integrated jet shapes to simulated data in selected P_T bins. Statistical errors are included.

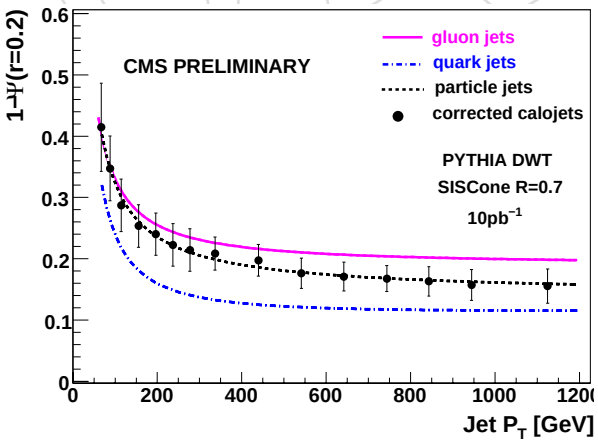

Figure 26: The fractional transverse momentum of a jet outside r=0.2, $1-\psi(0.2)$, as a function of the jet P_T for jets in the rapidity region $|y| < 1$. The reconstructed calorimeter jets, from PYTHIA Tune DWT (black points) are shown along with PYTHIA predictions for quark (dashed-dotted line) and gluon (solid line) initiated jets, and for all particle jets (dashed line). Systematic and statistical errors for the reconstructed calorimeter jets are added in quadrature. For the integrated shape the uncertainties at different r points are partially correlated.

The uncertainties arising from jet energy and position resolution, and from event selection cuts are expected to be negligible compared to the sources listed above and are not considered.

15.1 Jet Energy Scale

The uncertainty on the jet energy scale (JES) will be determined from data. Current expectation of the JES uncertainty at start up is $\pm 10\%$ [14]. Changing the JES correction within its uncertainty changes the jet shapes as jets migrate between P_T bins. Jet shapes vary slowly with jet P_T and thus this effect is expected to be small. To determine the impact on the jet shapes, we changed the P_T of the jet by $\pm 10\%$ and repeated the whole analysis. The comparison between the default JES corrections and the modified corrections is shown in Figure 27 (see also Figures 66, 67, 68 and 69). The corresponding systematic uncertainties on the differential jet shape are 10% at r=0.1 and $< 5\%$ at r =0.2 for all jet P_T. At larger $r \geq 0.5$ they are $< 20\%$.

The uncertainties on the integrated jet shape are 10% at r=0.1, 5% at r=0.2 for P_T <100 GeV, and decrease as a function of r. They are $< 2\%$ at r=0.1 for $P_T > 100$ GeV and negligible at r >0.1, as shown in Figure 28 (see also Figures 70, 71 and Figures 72, 73). (The systematic uncertainty at r=0.7 is 0 by definition of the integrated jet shape.)

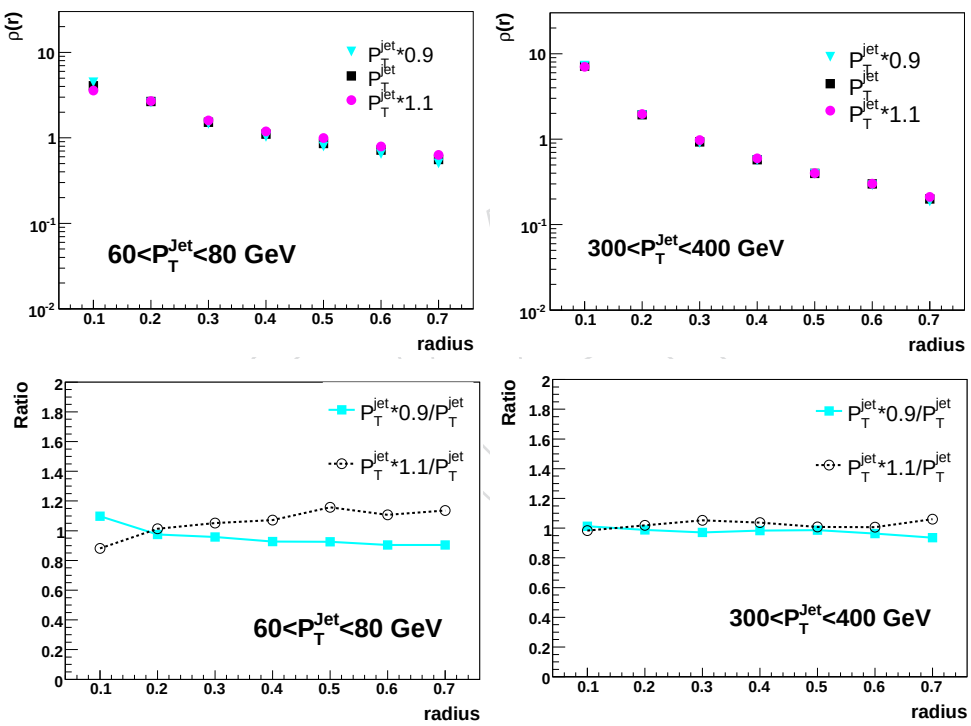

Figure 27: Differential jet shapes for $\pm 10\%$ change in energy scale (top) and fractional effect of changing jet energy scale (bottom), for selected P_T bins. Only statistical errors are included.

15.2 Jet Fragmentation

Because the calorimeter response depends on the energies of the particles in the jets, modeling of jet fragmentation contributes to the uncertainty on the corrected jet shapes. Uncertainties due to the fragmentation model can be estimated by comparing results obtained using PYTHIA and HERWIG++. The model of the underlying event used in HERWIG++ is described in [17].

Particle level differential and integrated jet shapes in PYTHIA DWT and HERWIG++ 2.2 [18]

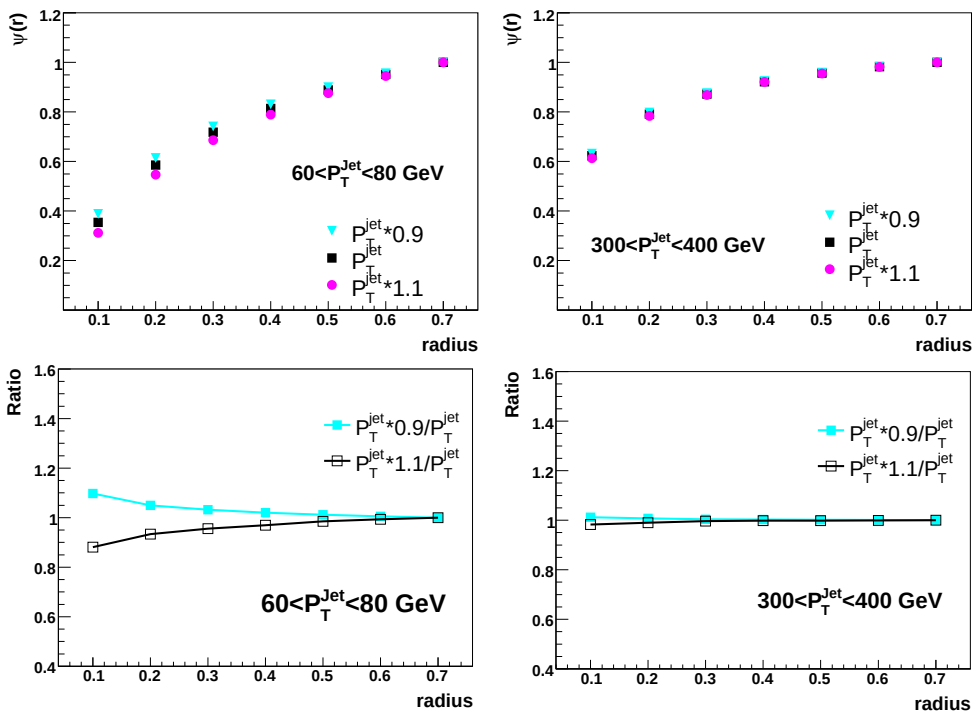

Figure 28: Integrated jet shapes for ±10% changes in energy scale (top) and fractional effect of changing the jet energy scale (bottom), for selected P_T bins. Only statistical errors are included.

are shown in Figure 29 (see also Figures 74 and 75) and Figure 30 (see also Figures 76 and 77), respectively. Their observed difference is less than 5% at r <0.3.

To determine the systematic uncertainty due to modeling of jet fragmentation we compared PYTHIA DWT and HERWIG++ differential jet shape correction factors, shown in Figure 31 (see also Figures 78 and 79). They agree to $< 10\%$ for $r \leq 0.2$, however, the differences can be as large as $30 - 40\%$ at $r \geq 0.5$. Note that the jet energy fraction at large r is small, which makes uncertainties on the differential jet shape measurement large in this region.

Comparisons of the integrated jet shape correction factors for PYTHIA DWT and HERWIG++ are shown in Figure 32 (see also Figures 80 and 81). They agree within 5% (2%) at r=0.1 (0.2) for $60 < P_T < 80$ GeV. For $P_T > 80$ GeV the differences range between $5 - 10\%$ at r=0.1 and are less than 5% at r=0.2. These differences decrease with increasing radius r for all jet P_T.

The correction factors have been also compared for PYTHIA DWT and PYTHIA DW simulations. The differences are less than 20% at r=0.1 and $< 10\%$ at $r = 0.2$. For differential jet shapes at large r, they can be as large as $20 - 30\%$. For integrated jet shapes, they become smaller for the high P_T jets and decrease with increasing r. The comparisons of correction factors for PYTHIA DWT and PYTHIA DW are shown in Figure 33 for differential jet shapes and in Figure 34 for integrated jet shapes (see also Figures 82 and 83, respectively).

15.3 Non-linearity of Calorimeter Response and Transverse Shower Profile

The uncertainties due to CMS calorimeter simulation can be estimated by comparing track jet shapes with calorimeter jet shapes in simulated and collider data. Here we assume that track reconstruction inefficiency and fake rate are small in both data and MC and have negligible effect on track jet shapes. These assumptions will be verified by comparing the track multiplicity

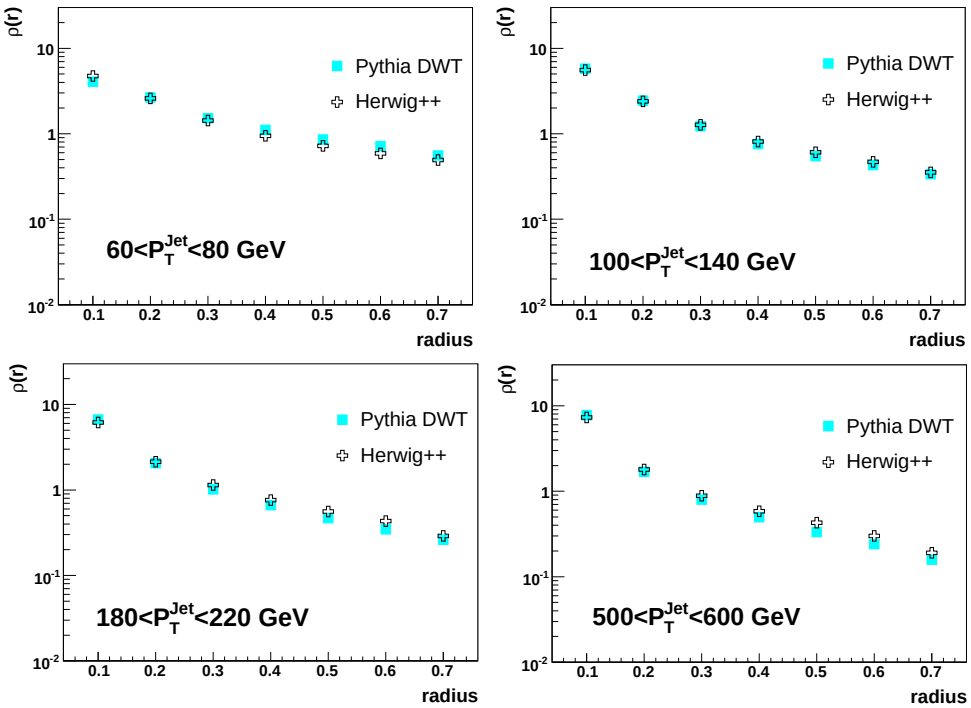

Figure 29: Comparison of differential jet shapes from HERWIG++ and PYTHIA for selected P_T bins. Only statistical errors are included.

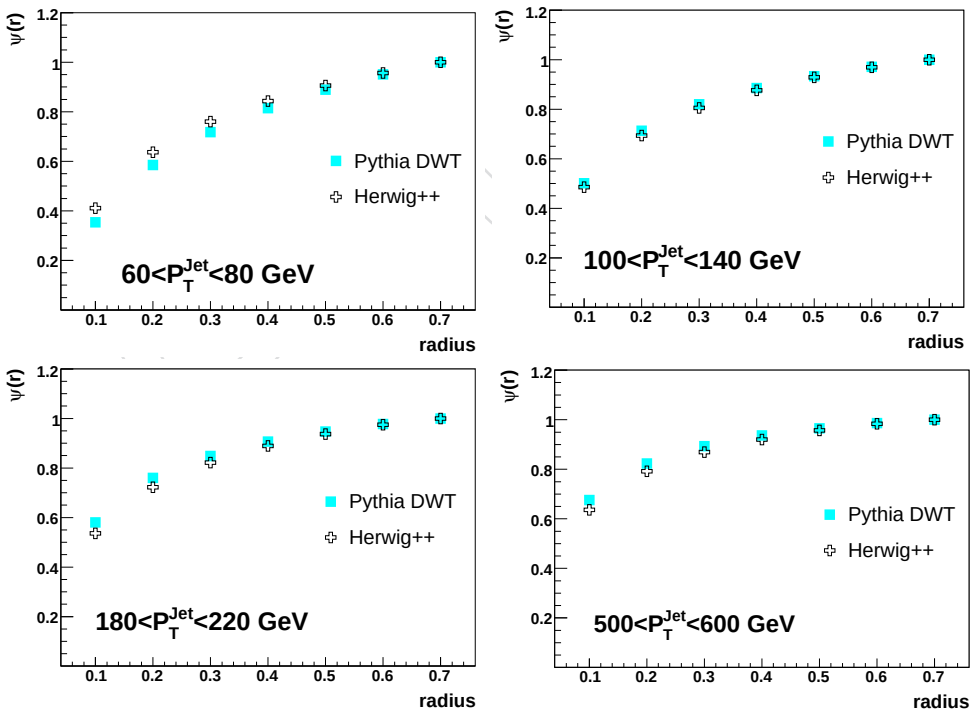

Figure 30: Comparison of integrated jet shapes from HERWIG++ and PYTHIA DWT for selected P_T bins. Only statistical errors are included.

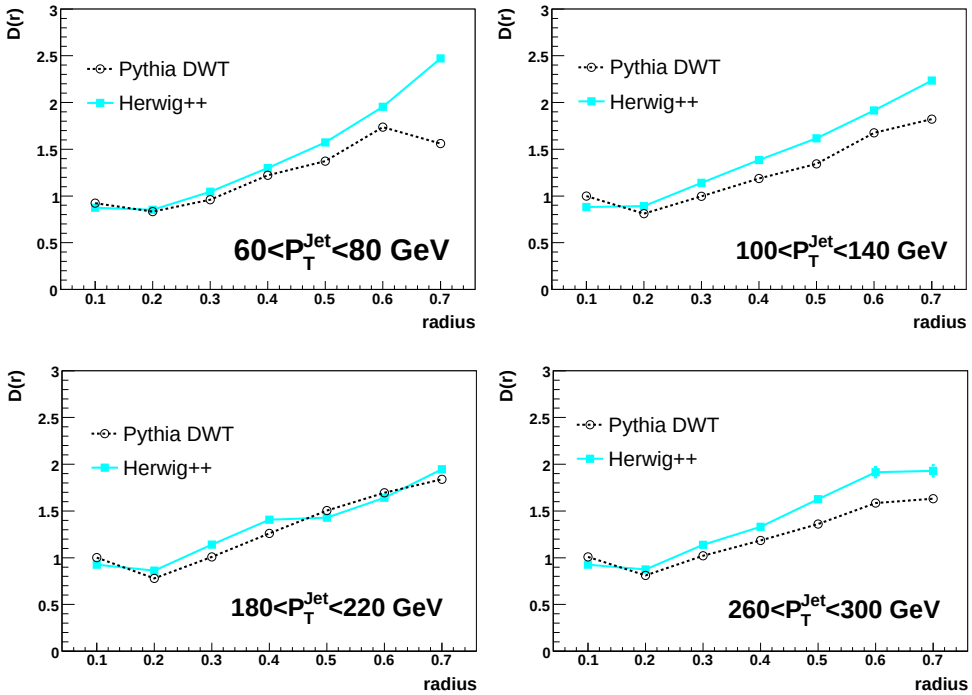

Figure 31: Comparison of the correction factors for PYTHIA DWT and HERWIG++ differential jet shapes. Only statistical errors are included.

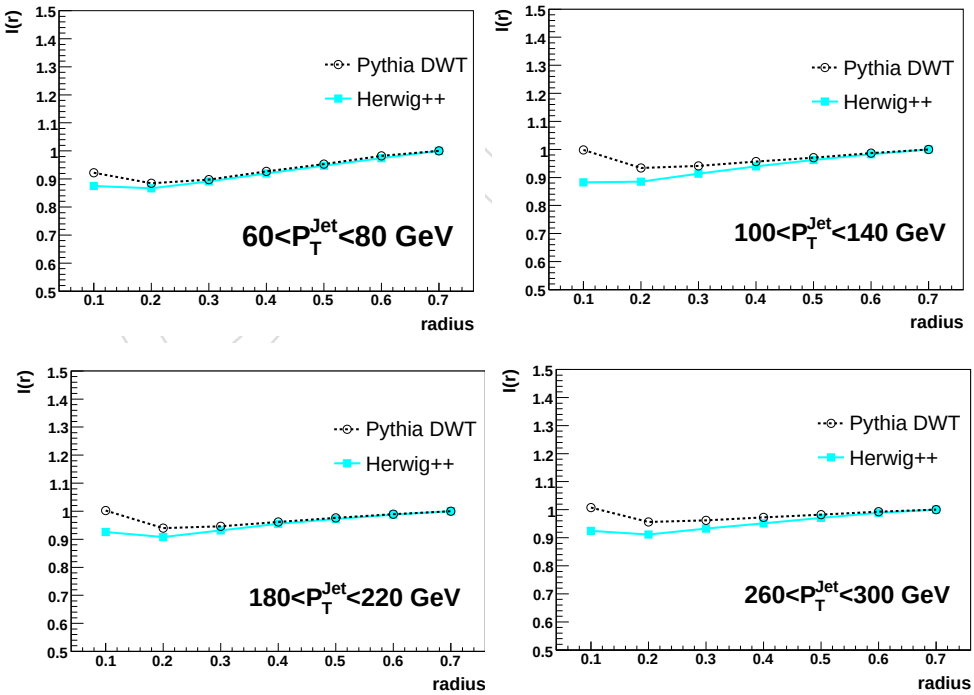

Figure 32: Comparison of the correction factors for PYTHIA DWT and HERWIG++ integrated jet shapes. Only statistical errors are included.

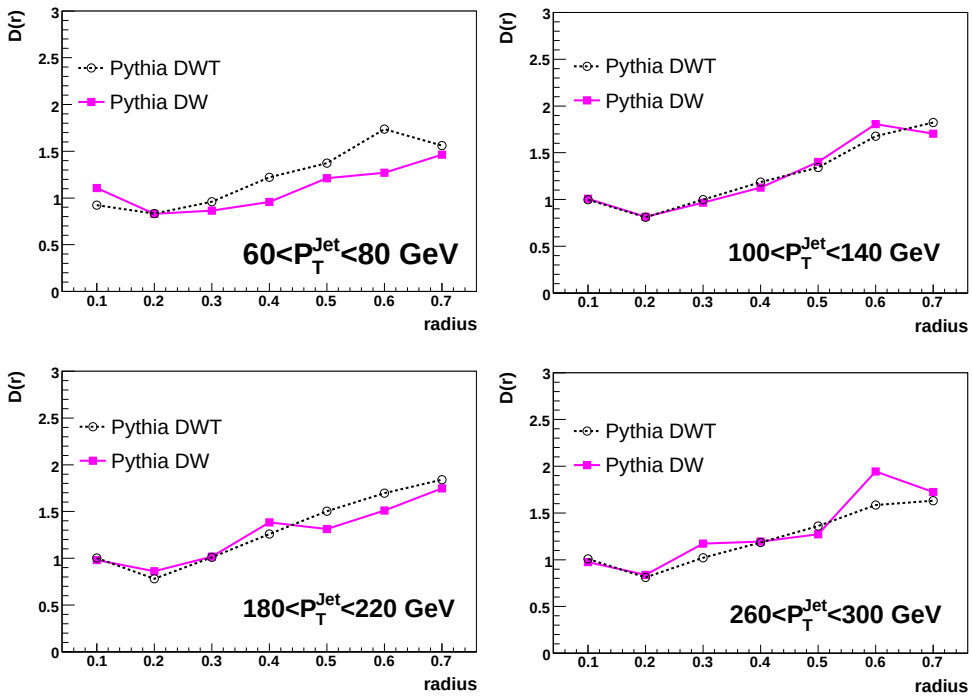

Figure 33: Comparison of the correction factors for PYTHIA DWT and DW differential jet shapes. Only statistical errors are included.

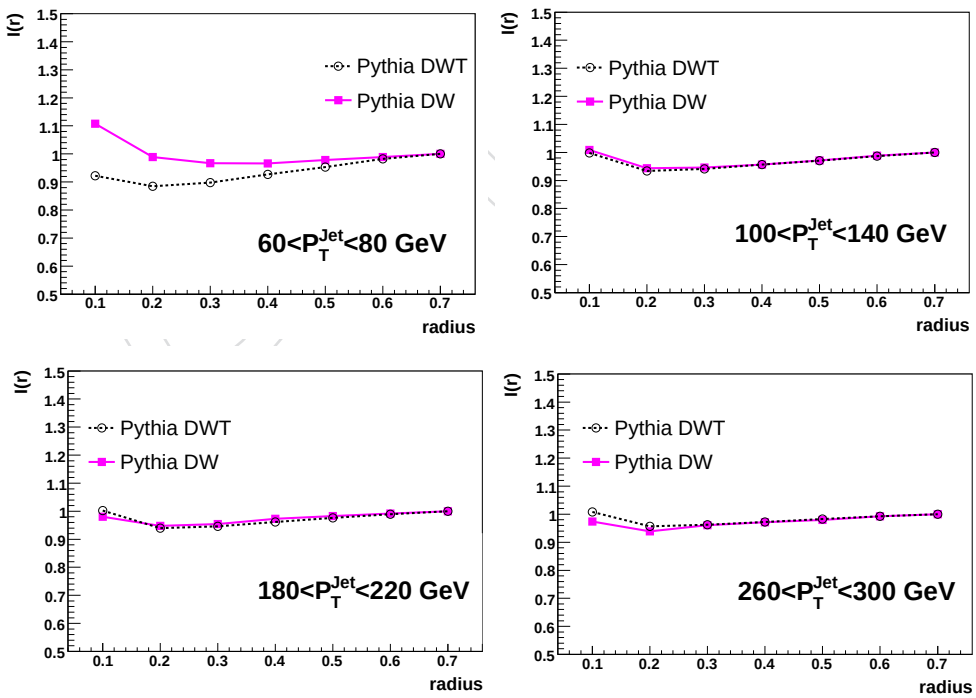

Figure 34: Comparison of the correction factors for PYTHIA DWT and DW integrated jet shapes. Only statistical errors are included.

and track P_T distributions in data and MC after applying the track reconstruction inefficiency and fake rate as measured from data. In addition, it is assumed that any difference in calorimeter response to photons in data and MC is much smaller than possible difference in calorimeter response to hadrons.

The differential track jetshapes are compared to calorimeter jetshapes in Figure 35 (see also Figures 62 and 63). Their ratios can be seen in Figures 64 and 65. We will measure the same ratio in data and determine the scale factor SF as defined below. This scale factor quantifies the difference between the data and the simulation and if it is ~ 1, we plan to scale the corrections derived from MC by SF and add the deviation from unity as systematic uncertainty. Analogous procedure can be done for the integrated jet shapes.

$$SF = \frac{R^{DATA}}{R^{MC}} \tag{7}$$

where

$$R^{MC} = \frac{TrackJetShape}{CaloJetShape}_{MC}, \; R^{DATA} = \frac{TrackJetShape}{CaloJetShape}_{DATA} \tag{8}$$

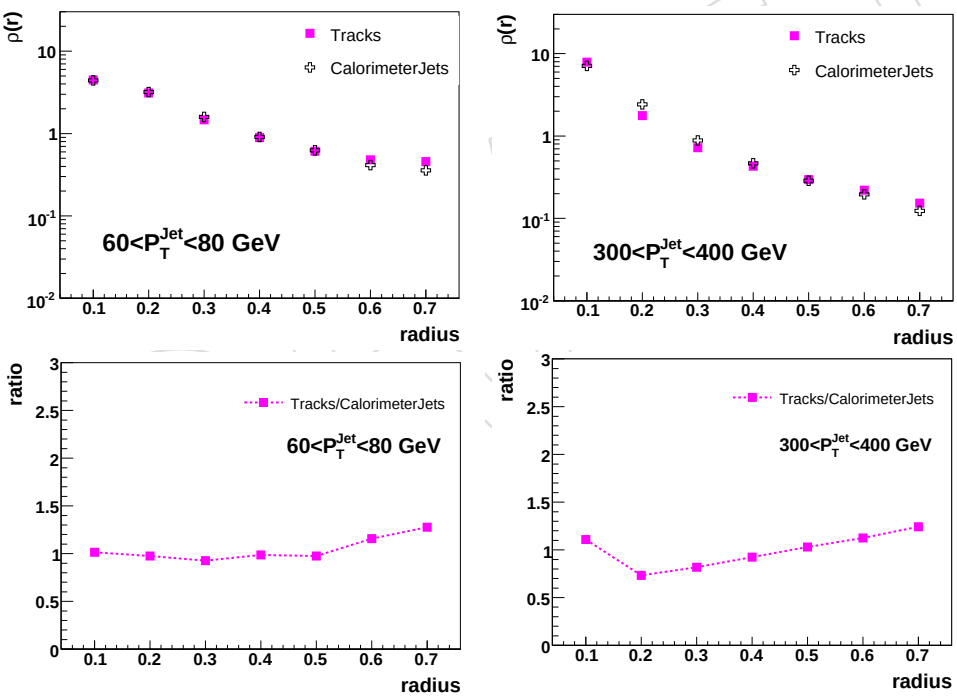

Figure 35: Comparison of the track jet shapes with the calorimeter jet shapes in simulated data (top) and their ratios (bottom) for selected P_T bins.

16 Monte Carlo Estimate of Systematics Due to Calorimeter Response

As mentioned above, the systematic uncertainties can not be derived before real data is available. In the absence of data, we estimated the size of the uncertainty due to a possible difference

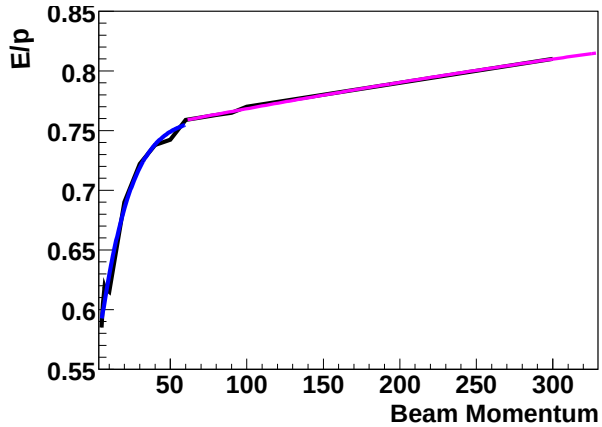

Figure 36: Single pion response from simulation

in calorimeter simulation and the expected real calorimeter response using a simple model. We determined the calorimeter jet shape obtained using a parameterized calorimeter response to single pions and compared it to the full simulation. The difference in the two calorimeter jet shapes accounts for a) transverse spreading of the showers, b) material interactions and energy threshold effects in the calorimeter. It is a simplified model and thus only a fraction of this difference should be considered as systematic uncertainty. However, for the purpose of this paper we used the full difference as an estimate of the related systematics. In Section 16.1 we discuss the effect of ignoring the transverse shower spreading in the calorimeter. In Section 16.2 we discuss p_T dependent systematics for calorimeter response to single particles. Figure 36 shows the single pion response from the simulation. The E/p curve was fitted in two p_T sub-ranges ($p_T < 70$ GeV and $p_T > 70$ GeV) with the function given in the equation below:

$$f(x) = \frac{A}{1 + Be^{-CX}} \tag{9}$$

We used variations of the E/p fit for estimating this part of the systematics.

16.1 Transverse Showering Spread

Calorimeter level shower shape is different than the particle level shape due to bending of charged particles in the magnetic field and to showering of particles in the calorimeter. To estimate the latter effect we used the parametrized E/p for single particle response to scale p_T of the particles. The scaled p_T was used to calculate new jet shapes, which take into account the E/p response but not the transverse shower spread. Response for the π^0, γ and e was taken as 1. Then we compared the calorimeter jet shapes obtained from a parameterized calorimeter response with calorimeter jet shapes obtained from full simulation. We consider the numbers below as upper limits on the expected uncertainties.

Figures 37 and 39 show the estimated impact of the transverse showering effect on differential and integrated jet shapes, respectively (see also Figures 84, 85 and Figures 88, 89). Figure 38 (Fig. 40) shows the deviations from unity of the ratio of differential (integrated) jet shapes obtained using the parameterized response to those from full simulation (see also Figures 86, 87 and Figures 90, 91). Based on this comparison, we estimated the uncertainty for differential jet shapes as $< 40\%$ at r=0.1 and $< 20\%$ for r=0.2 at $60 < P_T < 80$ GeV, and $< 20\%$ for $r \leq 0.2$ at $80 < P_T < 100$ GeV. The deviation from unity at r=0.2 does not change much for jet P_T >100 GeV while at r=0.1 it decreases slowly as a function of jet P_T.

The transverse showering uncertainty for the integrated jet shapes is negligible for r >0.3 for all jet P_T. For 60 < P_T < 80 GeV, the difference is 30% (10%) at r=0.1 (0.2) and decreases to 20% (10%) for r=0.1 (0.2) for 80 P_T <100 GeV jets. For jets with P_T >100 GeV, the difference is 10% at r=0.1 and negligible for r >0.1. In Figure 26, these differences are added in quadrature with the other sources of systematic uncertainty.

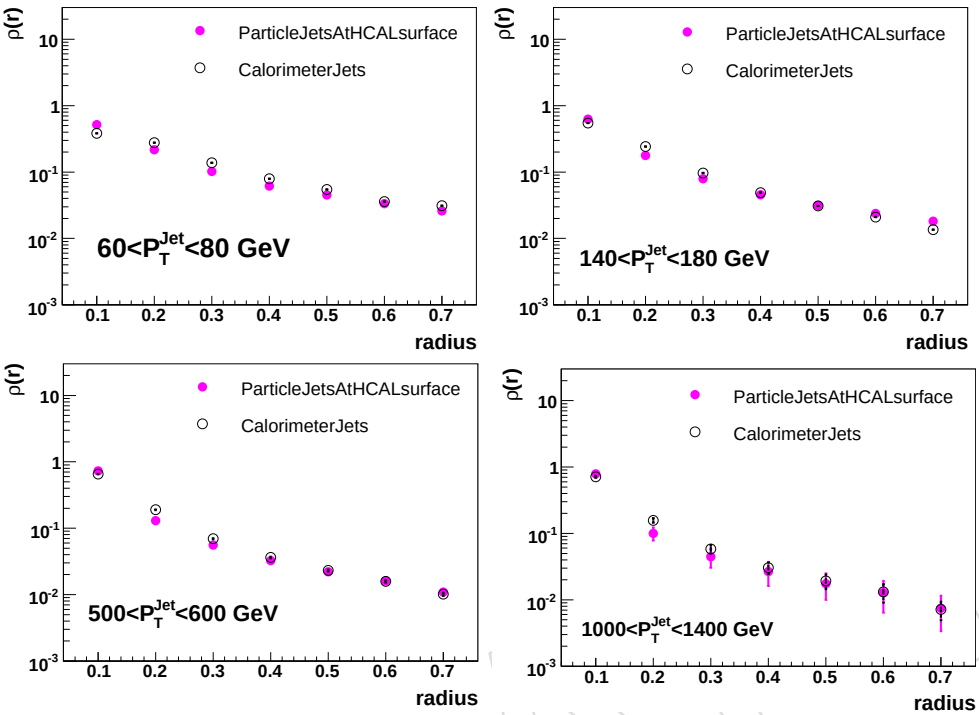

Figure 37: Effect of transverse showering spread for the differential jet shapes. Only statistical errors are included.

16.2 Linearity of the Calorimeter Response

The observed jet shape depends on the E/p response function for single particles. The uncertainty due to E/p simulation in the MC can be estimated by varying the single particle response function within its expected error.

As before, p_T of each track was scaled with the fitted E/p curve. Since no official estimate of uncertainty on E/p curve was available, we used an educated guess. We changed the E/p parameterization by ±10% for p_T <50 GeV and by ±5% for p_T >50 GeV and then we determined the new calorimeter jet shape. Figures 41 and 42 show the "scaling difference" for differential and integrated jet shapes due to such "$\pm 1\sigma$" variations of E/p (see also Figures 92, 93, 94, and 95). For jets with 60< P_T <80 GeV, the differential jet shape changes by < 2% at the low radius (r=0.1) and < 4% at r >0.1 while the differences are negligible at r=0.1 for jet P_T >80 GeV. The integrated jet shapes are less affected by this scaling: < 2% at r=0.1, and negligible at r > 0.1.

17 Conclusions

Using PYTHIA and HERWIG++ MC simulations, we have investigated a technique to measure jet shapes in pp collisions for the two leading jets in the kinematic region 60 GeV< P_T < 1.4 TeV and $|y|$ < 1. Particle level jet shapes were determined from calorimeter jets using corrections derived from PYTHIA MC events.

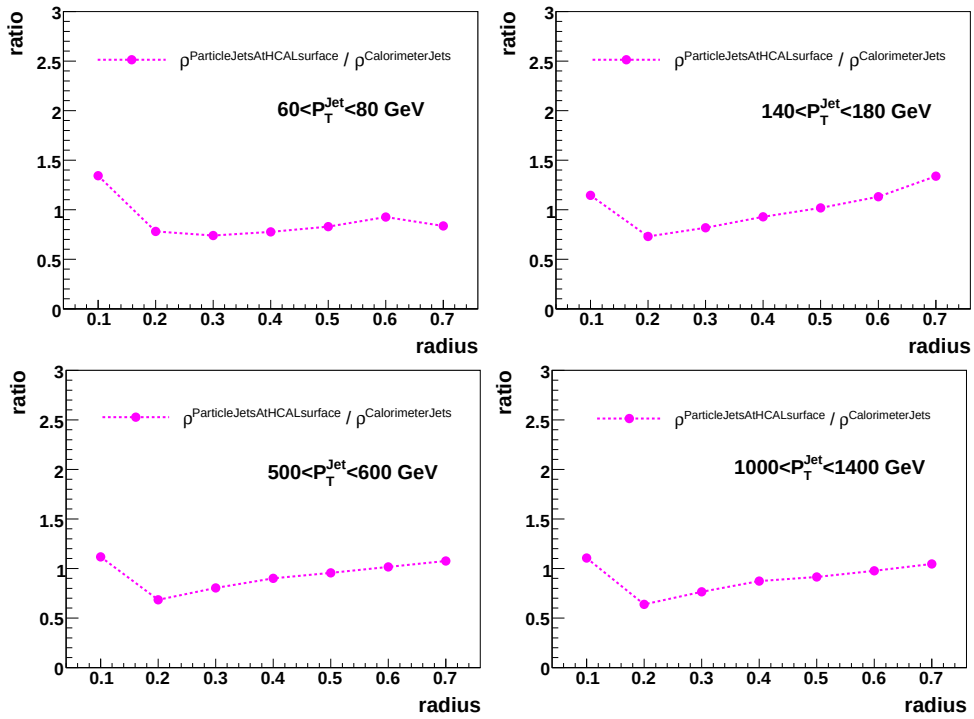

Figure 38: Ratio of the differential jet shapes obtained using the parameterized response (without transverse showering) to those from full simulation.

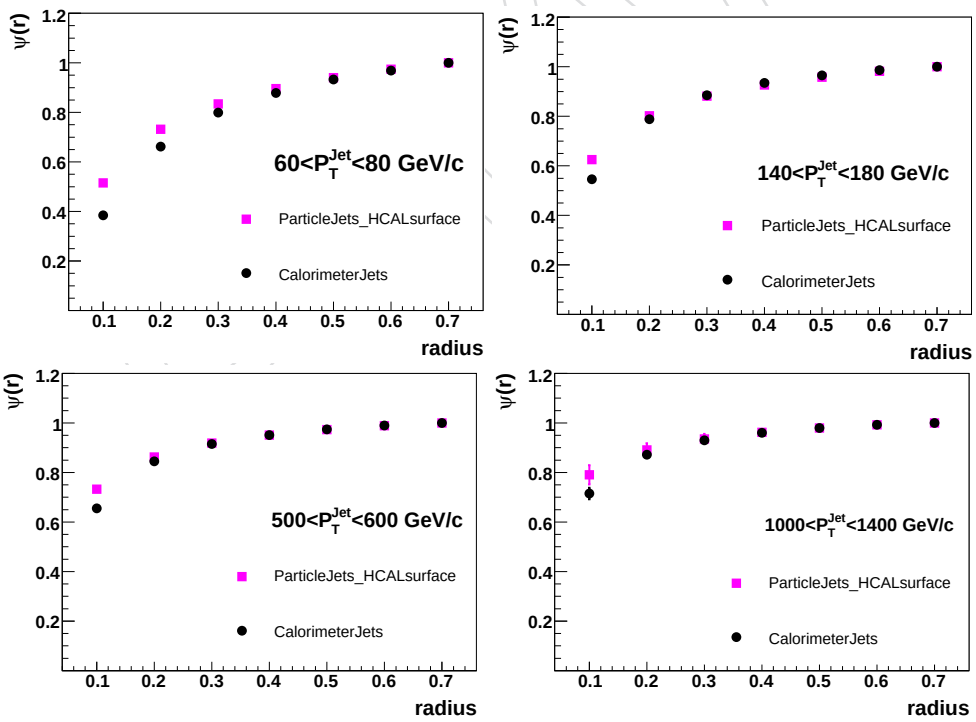

Figure 39: Effect of transverse showering spread for the integrated jet shapes. Only statistical errors are included.

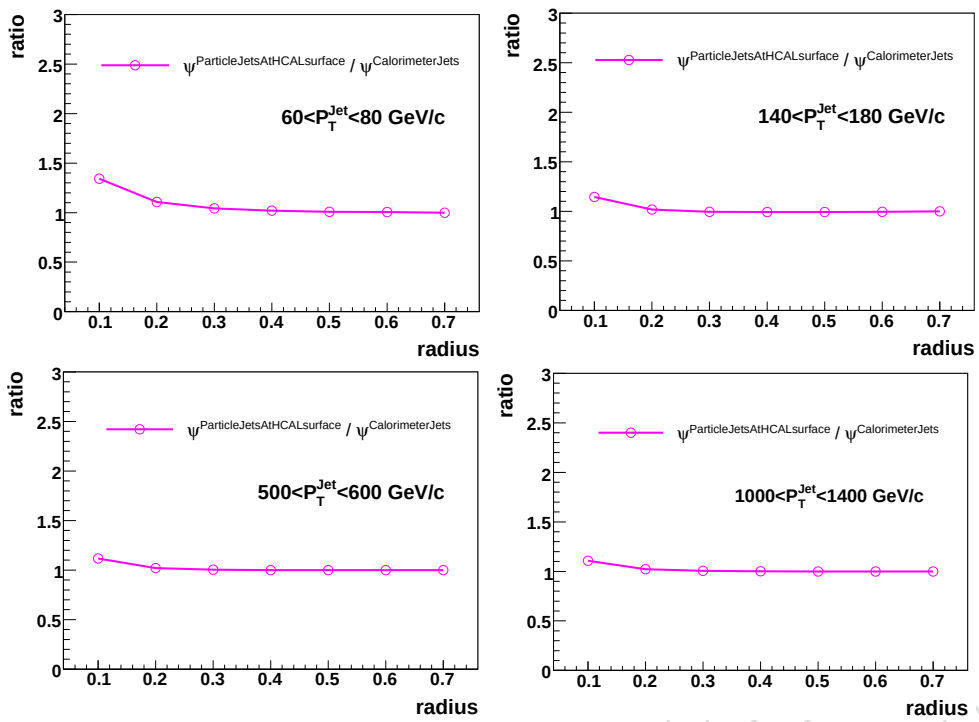

Figure 40: Ratio of the integrated jet shapes obtained using the parameterized response (without transverse showering) to those from full simulation.

DRAFT

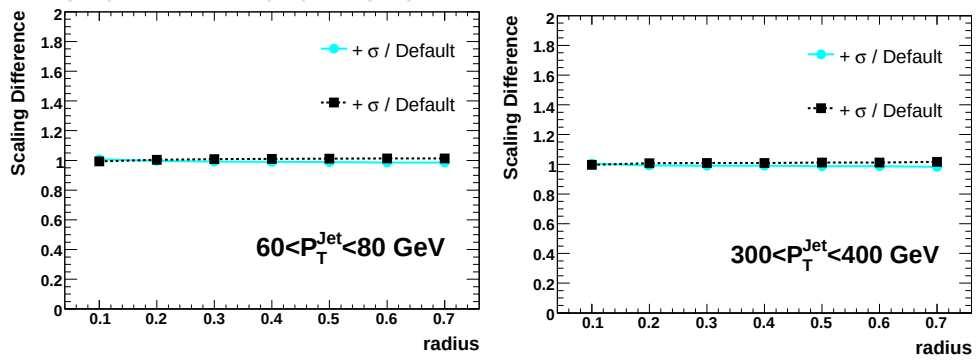

Figure 41: Scaling difference due to the E/p variation(see text) for the differential jet shapes for selected P_T bins.

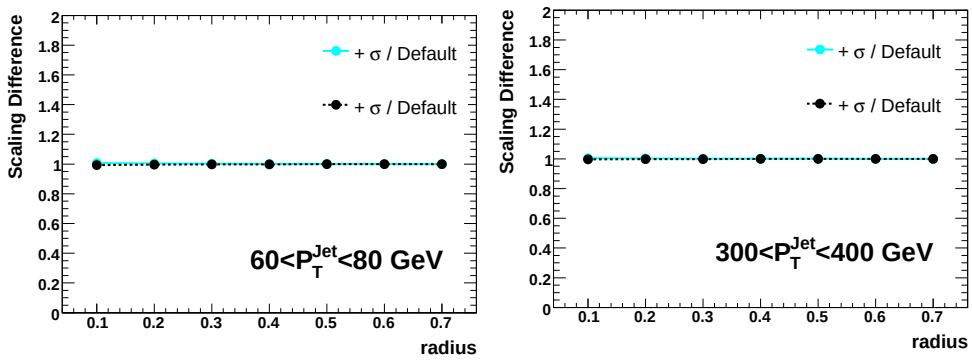

Figure 42: Scaling difference due to the E/p variation (see text) for the integrated jet shapes for selected P_T bins.

Several sources of systematic uncertainties were investigated, arising from jet energy calibration, jet fragmentation, calorimeter response and transverse showering, as function of jet P_T and distance from jet axis r. The systematic uncertainty is dominated by overall jet energy scale, jet fragmentation and calorimeter simulation effects. The total systematic uncertainty at r=0.2 is 12% at P_T=60 GeV, decreasing to 4% at jet P_T=1 TeV.

As expected in QCD, jet shapes are observed to become narrower with increasing jet P_T. Different underlying event tunes (PYTHIA DWT and PYTHIA DW) were studied. PYTHIA DW tends to produce narrower jet shapes in the low P_T region. QCD predicts different shapes of jets originating from quarks and gluons. A measurement of the jet shapes in the context of the PYTHIA Monte Carlo gives an estimate of the fraction of gluon initiated jets in data as a function of jet P_T.

DRAFT

HLT threshold (GeV)	Prescale
30	10^5
60	10^4
110	10^2
150	10
200	1

Table 1: HLT thresholds and prescales

P_T (GeV)	N^{Jets}	$N^{Jets}_{prescaled}$ (N_p)	$Mean\ \psi(r=0.2)$	rms	$\sigma = rms/\sqrt{(N_p)}$	$\sigma/Mean(\%)$
$60-80$	$1.311e+08$	1311.7	0.66	0.24	0.006	0.90
$80-100$	$2.803e+07$	2803.1	0.72	0.21	0.004	0.55
$100-140$	$1.328e+07$	132.8	0.76	0.20	0.017	2.31
$140-180$	$2.484e+06$	248498	0.78	0.20	0.0004	0.05
$180-220$	682348	682348	0.80	0.20	0.0002	0.02
$220-260$	256142	256142	0.81	0.21	0.0004	0.04
$260-300$	102488	102488	0.82	0.20	0.0006	0.07
$300-400$	83581.5	83581.5	0.83	0.21	0.0006	0.07
$400-500$	17589.5	17589.5	0.83	0.21	0.001	0.11
$500-600$	5282.8	5282.8	0.84	0.21	0.002	0.23
$600-700$	1909.3	1909.3	0.85	0.20	0.004	0.46
$700-800$	753.8	753.8	0.85	0.22	0.007	0.81
$800-900$	325.8	325.8	0.86	0.22	0.012	1.3
$900-1000$	159.2	159.2	0.86	0.21	0.016	1.87
$1000-1400$	158.1	158.1	0.87	0.21	0.016	1.83

Table 2: Number of jets before and after prescale, and mean and rms values of the p_T fraction histograms at r=0.2 in 10 pb^{-1} for all P_T jet bins which were analyzed. Statistical errors are listed for the corresponding jet P_T using prescaled event numbers.

DRAFT

P_T (GeV)	$Fragmentation(\%)$	$JES(\%)$	$Showering(\%)$	$E/p(\%)$	$TotalSys.(\%)$
$60-80$	1.82	5.78	10.7	0.39	12.3
$80-100$	2.20	5.5	5.4	0.33	8.06
$100-140$	4.85	1.38	2.4	0.30	5.58
$140-180$	4.18	1.0	1.6	0.26	4.62
$180-220$	3.10	0.81	0.7	0.24	3.29
$220-260$	4.22	0.96	1.1	0.23	4.49
$260-300$	4.48	0.13	1.8	0.23	4.85
$300-400$	3.23	0.83	0.7	0.21	3.42
$400-500$	2.35	0.92	2.0	0.19	3.23
$500-600$	4.71	0.68	2.0	0.18	5.19
$600-700$	1.69	0.44	1.3	0.16	2.19
$700-800$	2.85	0.51	1.7	0.16	3.40
$800-900$	2.17	0.39	1.3	0.15	2.56
$900-1000$	1.99	0.11	1.3	0.14	2.41
$1000-1400$	1.73	0.74	2.2	0.12	2.9

Table 3: Different sources of systematics for $\psi(r = 0.2)$ listed as percentage contributions for all jet P_T bins for 10 pb^{-1} of integrated luminosity. Total systematics is a quadrature sum of fragmentation, jet energy scale, showering and E/p contributions.

DRAFT

P_T (GeV)	Raw $\psi(r = 0.2)$	$I(r = 0.2)$	$1 - \psi(r = 0.2)$	$AbsErr$
$60 - 80$	0.66	0.90	0.41	0.072
$80 - 100$	0.72	0.93	0.34	0.052
$100 - 140$	0.76	0.94	0.28	0.043
$140 - 180$	0.79	0.94	0.25	0.034
$180 - 220$	0.80	0.95	0.24	0.025
$220 - 260$	0.81	0.95	0.22	0.034
$260 - 300$	0.82	0.95	0.21	0.038
$300 - 400$	0.83	0.96	0.20	0.027
$400 - 500$	0.83	0.97	0.19	0.025
$500 - 600$	0.84	0.96	0.17	0.042
$600 - 700$	0.85	0.97	0.17	0.018
$700 - 800$	0.85	0.97	0.16	0.029
$800 - 900$	0.86	0.97	0.16	0.024
$900 - 1000$	0.86	0.96	0.15	0.025
$1000 - 1400$	0.87	0.97	0.15	0.028

Table 4: Absolute error on $1 - \psi(r = 0.2)$ represents quadratic sum of systematic and statistical uncertainties for 10 pb^{-1} of integrated luminosity. $I(r = 0.2)$ refers to the integrated correction factors at r=0.2.

DRAFT

References

[1] S. D. Ellis, Z. Kunszt, and D. E. Soper, "Jets at hadron colliders at order alpha-s**3: A Look inside," *Phys. Rev. Lett.* **69** (1992) 3615–3618, arXiv:hep-ph/9208249. doi:10.1103/PhysRevLett.69.3615.

[2] M. H. Seymour, "Jet shapes in hadron collisions: Higher orders, resummation and hadronization," *Nucl. Phys.* **B513** (1998) 269–300, arXiv:hep-ph/9707338. doi:10.1016/S0550-3213(97)00711-6.

[3] **CDF** Collaboration, F. Abe et al., "A Measurement of jet shapes in $p\bar{p}$ collisions at $\sqrt{s} = 1.8$ TeV," *Phys. Rev. Lett.* **70** (1993) 713–717. doi:10.1103/PhysRevLett.70.713.

[4] **D0** Collaboration, S. Abachi et al., "Transverse energy distributions within jets in $p\bar{p}$ collisions at $\sqrt{s} = 1.8$ TeV," *Phys. Lett.* **B357** (1995) 500–508. doi:10.1016/0370-2693(95)00889-S.

[5] **CDF** Collaboration, D. E. Acosta et al., "Study of jet shapes in inclusive jet production in $p\bar{p}$ collisions at $\sqrt{s} = 1.96$ TeV," *Phys. Rev.* **D71** (2005) 112002, arXiv:hep-ex/0505013. doi:10.1103/PhysRevD.71.112002.

[6] **H1** Collaboration, C. Adloff et al., "Measurements of transverse energy flow in deep inelastic scattering at HERA," *Eur. Phys. J.* **C12** (2000) 595–607, arXiv:hep-ex/9907027. doi:10.1007/s100520000287.

[7] **ZEUS** Collaboration, J. Breitweg et al., "Measurement of jet shapes in high-Q**2 deep inelastic scattering at HERA," *Eur. Phys. J.* **C8** (1999) 367–380, arXiv:hep-ex/9804001. doi:10.1007/s100520050471.

[8] **CMS** Collaboration, " The Compact MUon Solenoid (CMS) Technical Proposal,". CERN/LHCC 94-38.

[9] **CMS** Collaboration, "CMS TDR4,". CERN/LHCC 97-33.

[10] **CMS** Collaboration, "CMS TDR2,". CERN/LHCC 97-31.

[11] G. Blazey et al., "Run II Jet Physics,". hep-ex/0005012.

[12] **CMS** Collaboration, P. Kurt et al., "Performance of the k_t Jet Algorithms in CMS,". CMS AN-2007/062.

[13] G. P. Salam, "A Practical Seedless Infrared Safe Cone Algorithm," arXiv:0705.2696.

[14] **CMS** Collaboration, "Plans for Jet Energy Corrections at CMS,". CMS-PAS-JME-007-002.

[15] **CMS** Collaboration, "The Underlying Event at LHC,". CMS-Note-2006/067.

[16] M. L. Mangano, M. Moretti, F. Piccinini, R. Pittau, and A. D. Polosa, "ALPGEN, a generator for hard multiparton processes in hadronic collisions," *JHEP* **07** (2003) 001, arXiv:hep-ph/0206293.

[17] M. Bahr, S. Gieseke, and M. H. Seymour, "Simulation of multiple partonic interactions in Herwig++," *JHEP* **07** (2008) 076, arXiv:0803.3633. doi:10.1088/1126-6708/2008/07/076.

[18] M. Bahr et al., "Herwig++ 2.2 Release Note," arXiv:0804.3053.

DRAFT

A Appendix: Figures for All Jet P_T Bins

In the following pages we present an expanded set of figures for all jet P_T bins.

DRAFT

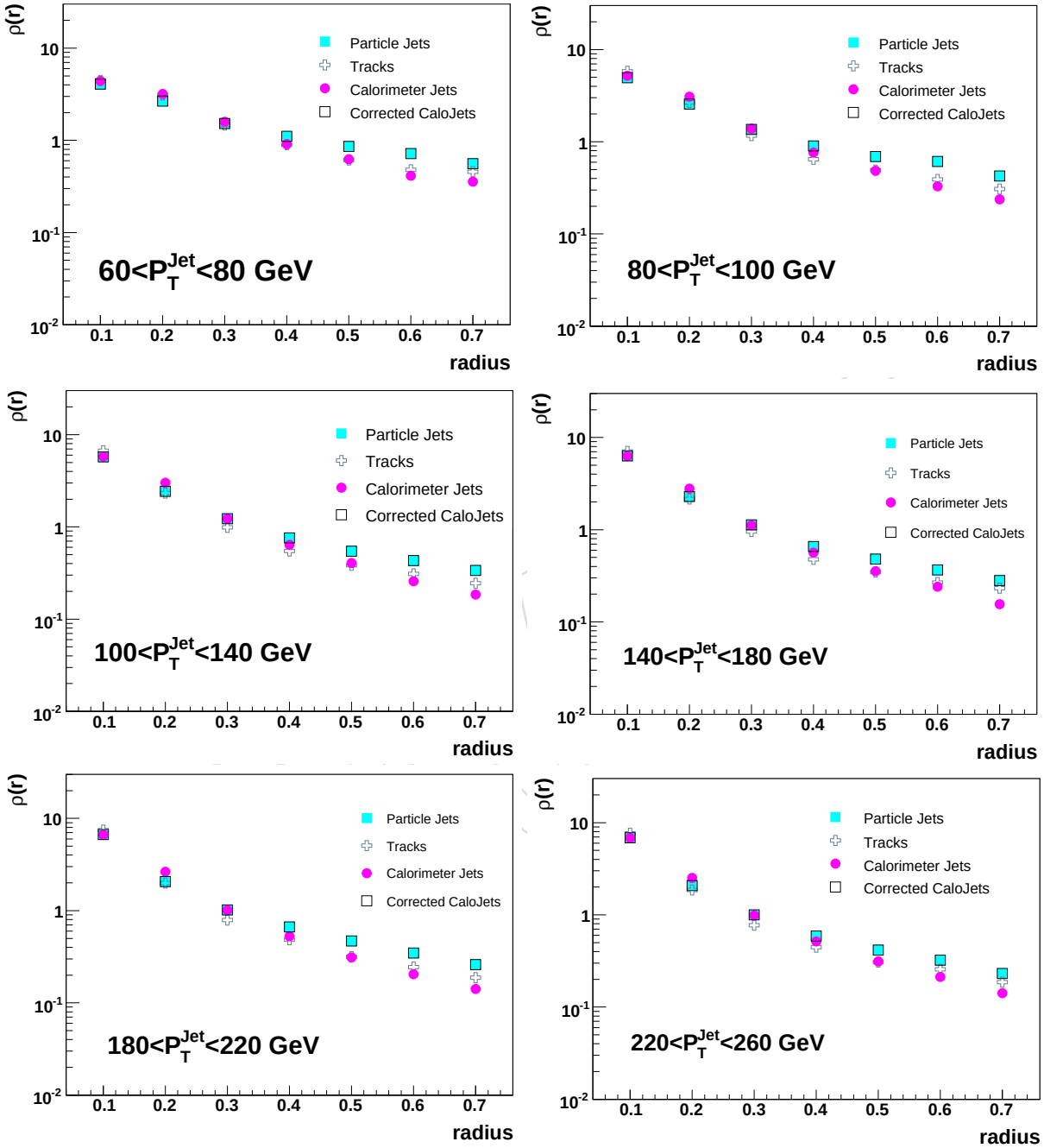

Figure 43: Differential jet shapes for selected P_T bins. Statistical errors are included.

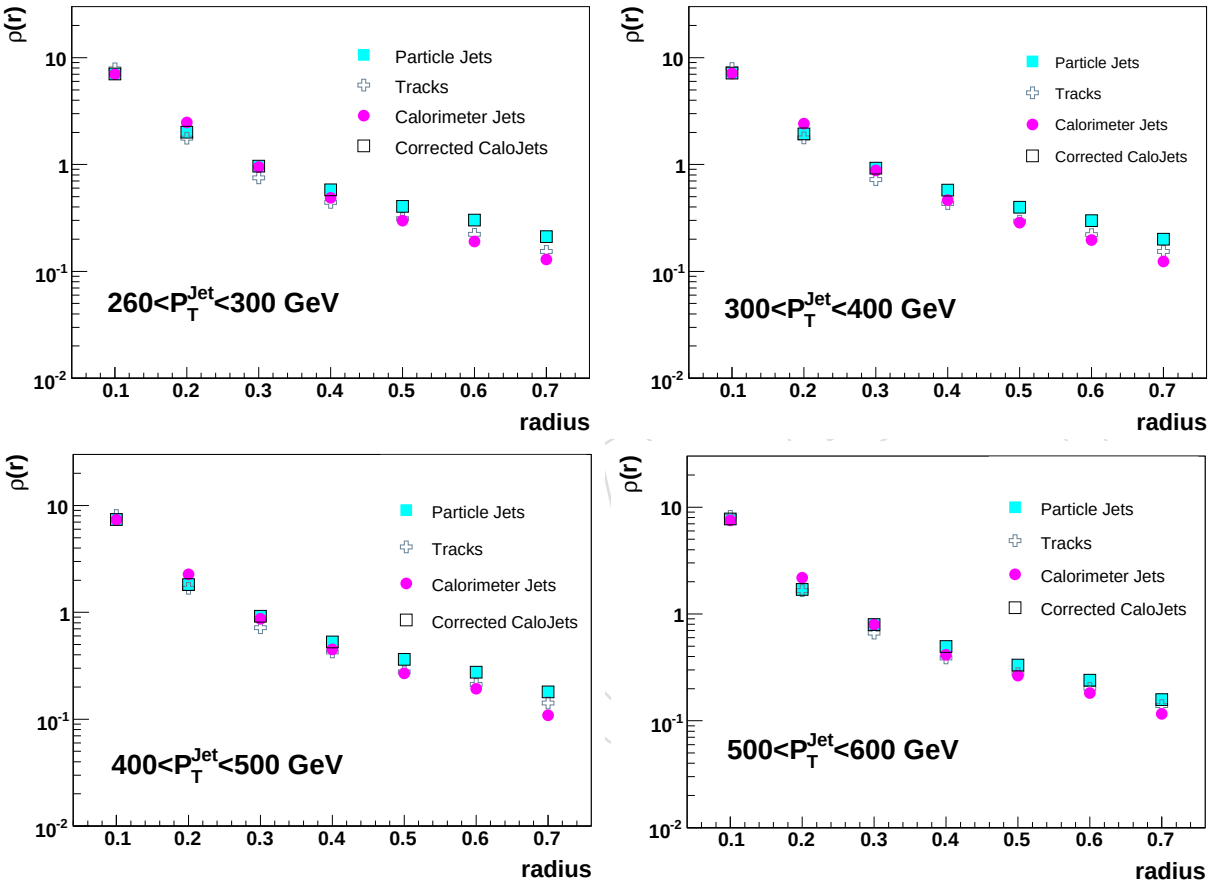

Figure 44: Differential jet shapes for selected P_T bins. Statistical errors are included.

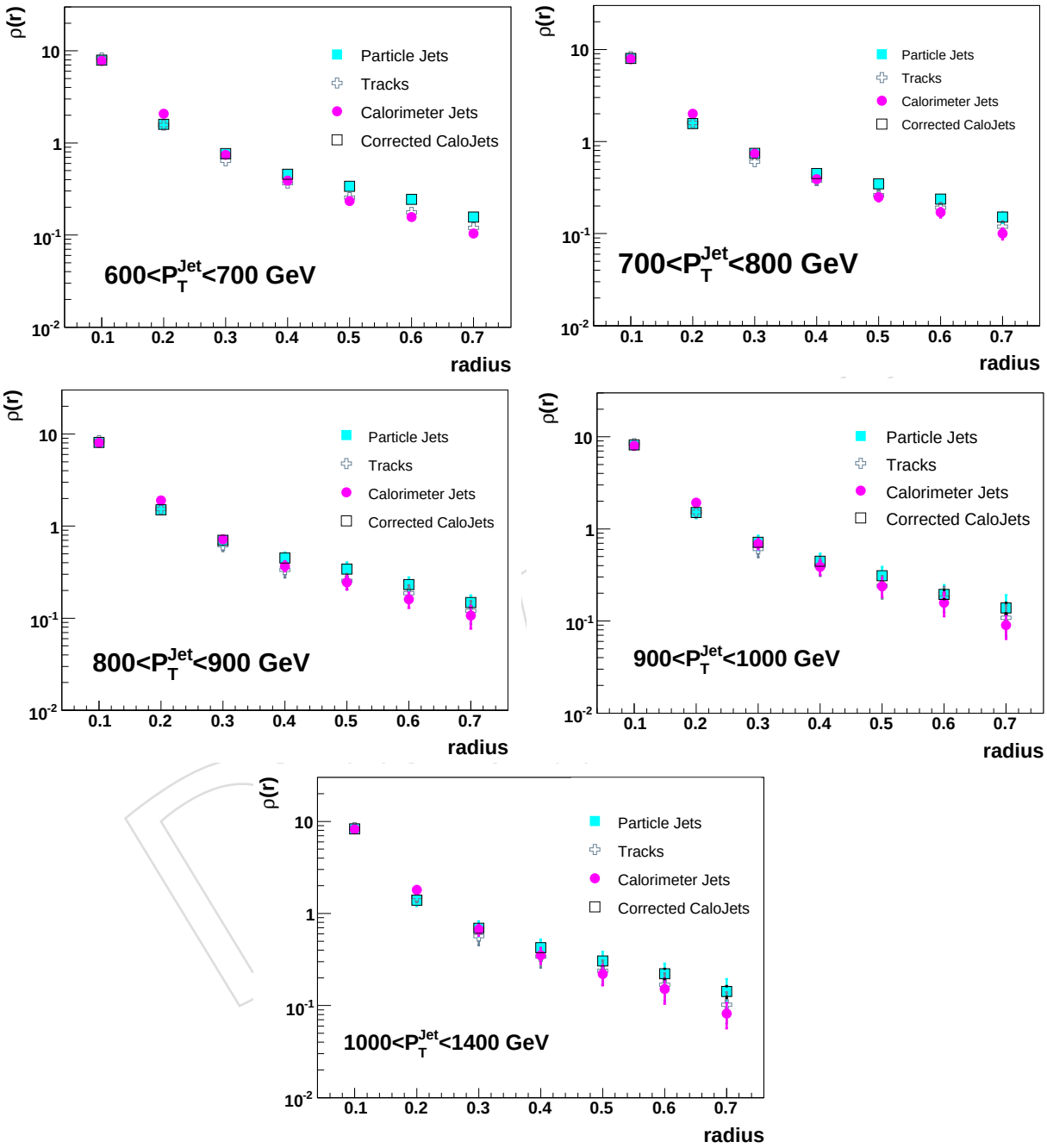

Figure 45: Differential jet shapes for selected P_T bins. Statistical errors are included.

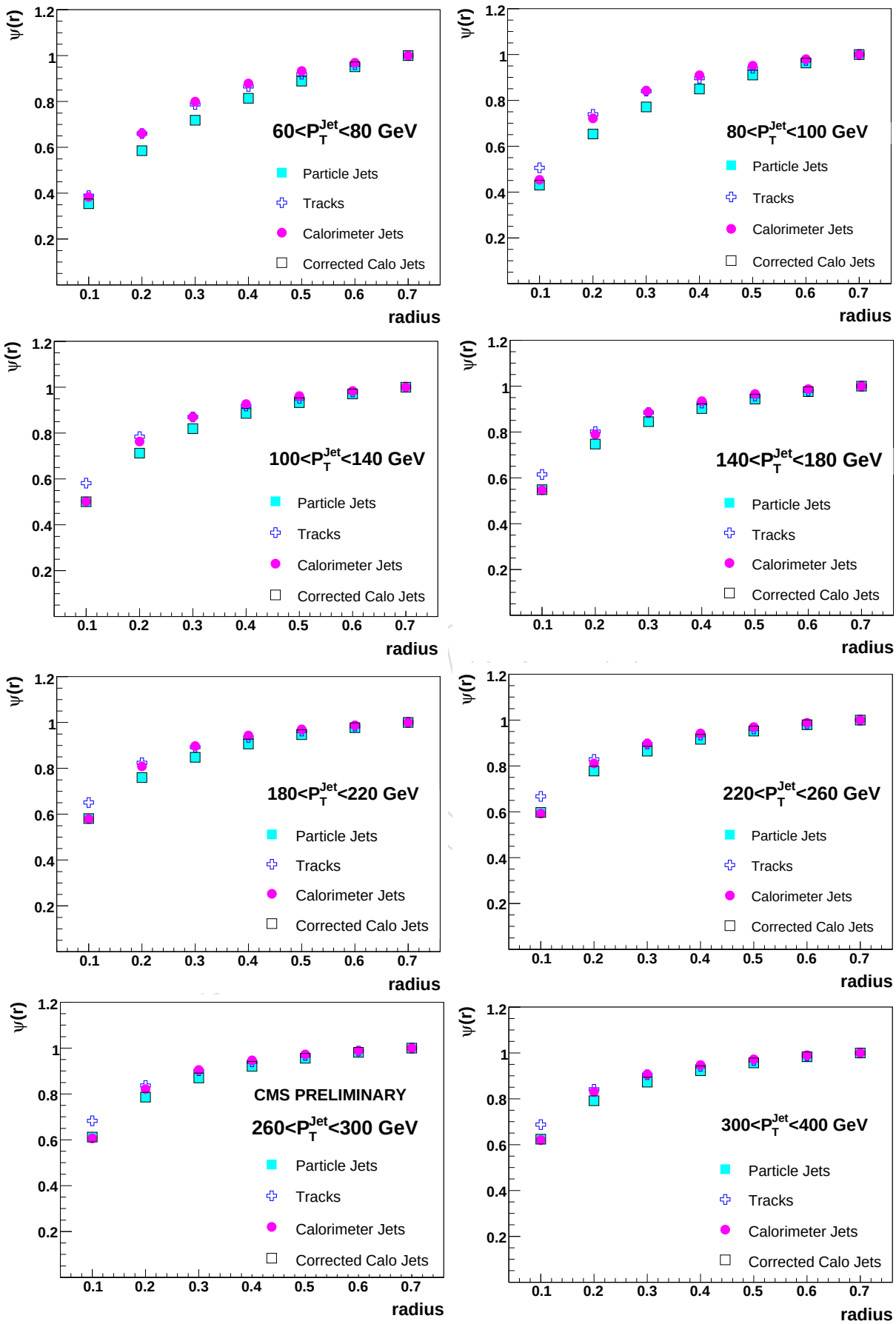

Figure 46: Integrated jet shapes for selected P_T bins. Statistical errors are included.

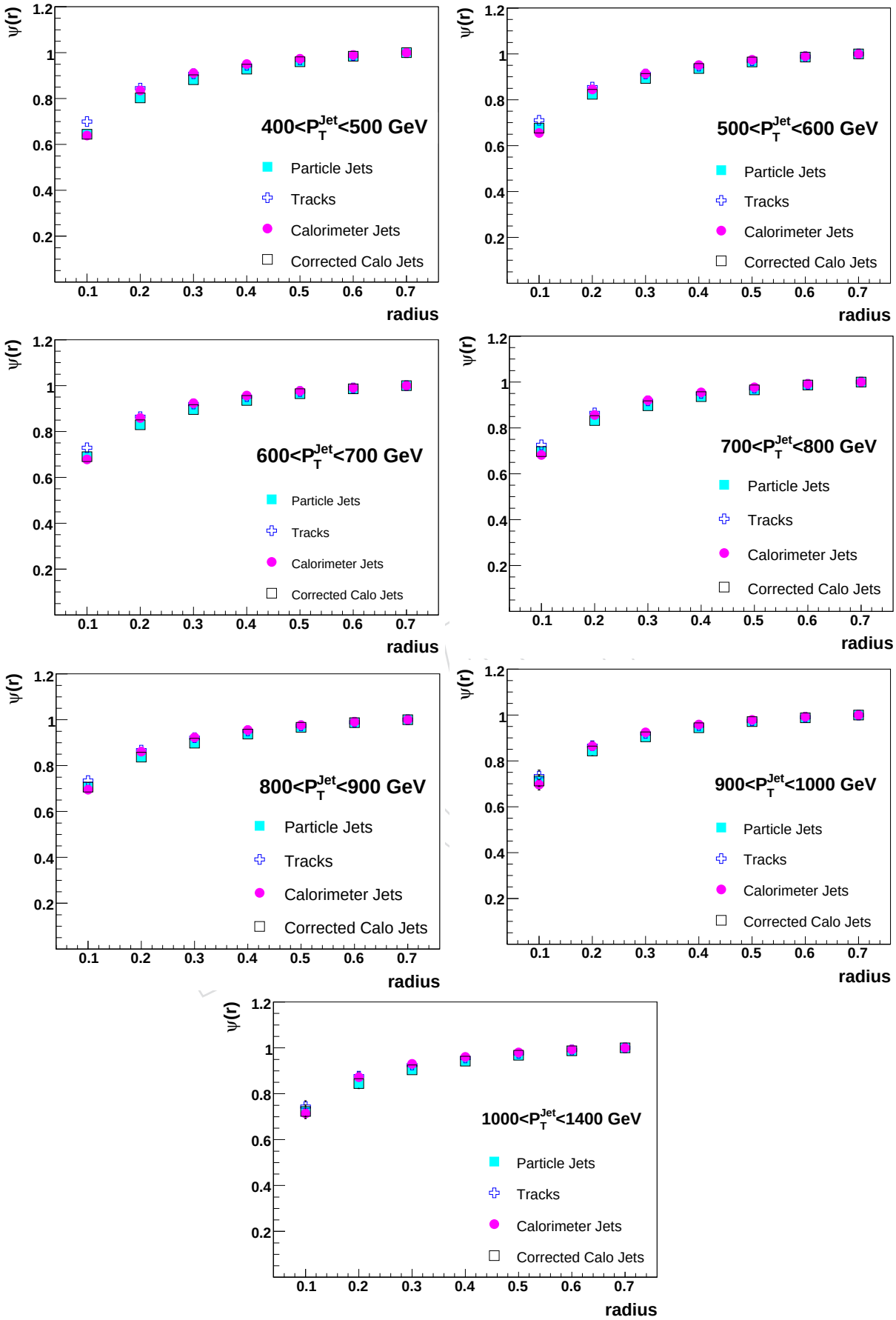

Figure 47: Integrated jet shapes for selected P_T bins. Statistical errors are included.

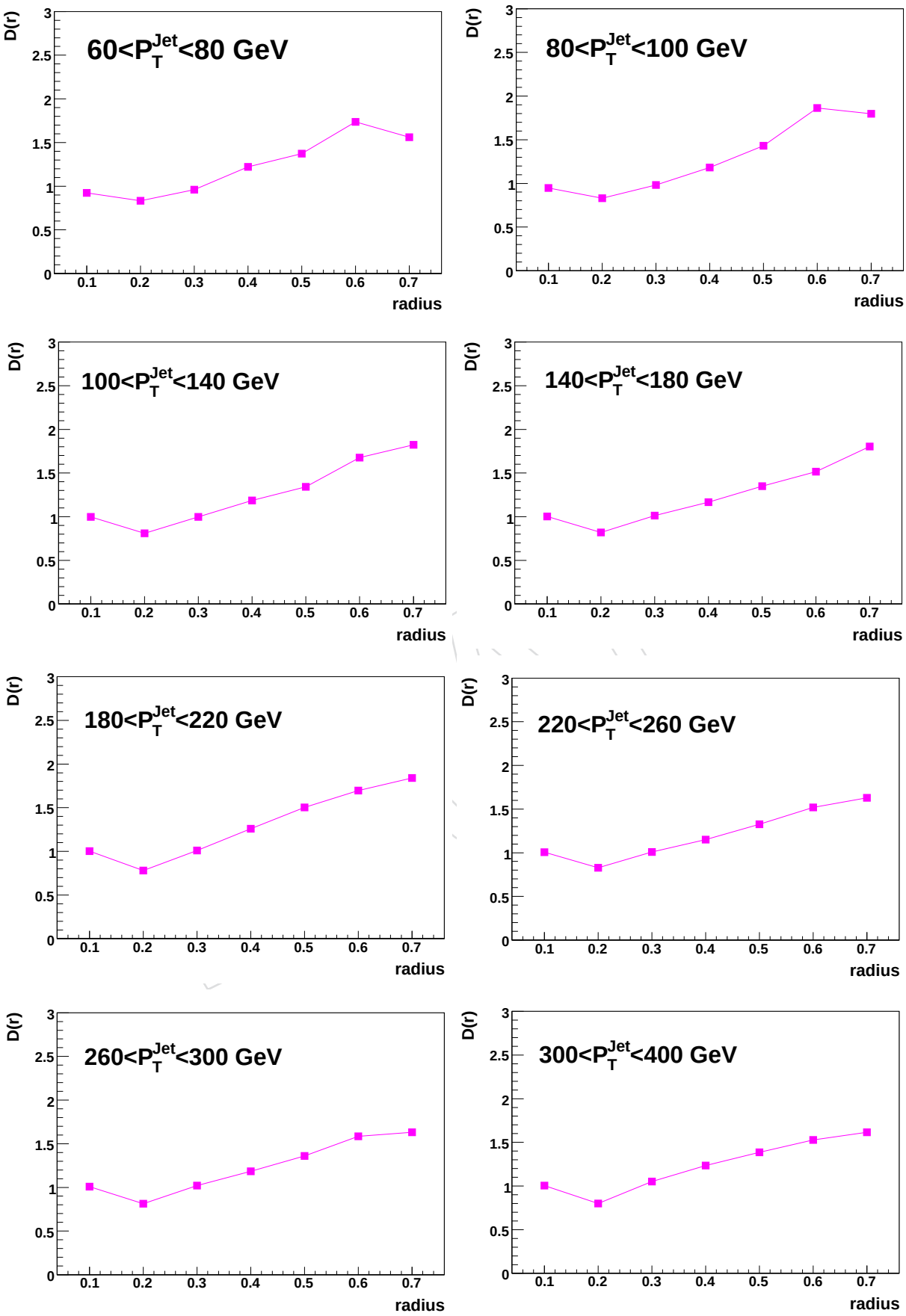

Figure 48: Correction factors for differential jet shapes for selected P_T bins. Statistical errors are included.

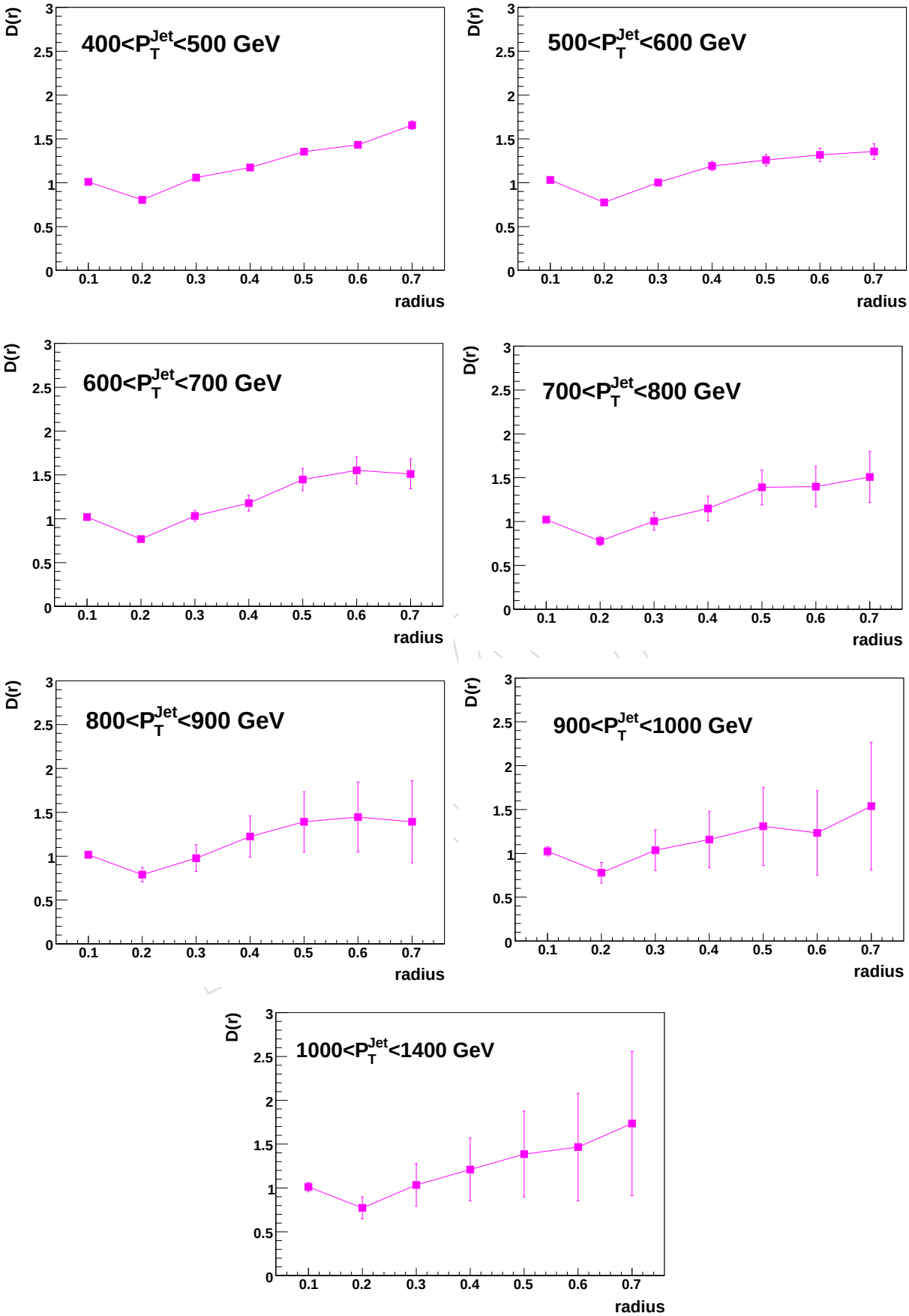

Figure 49: Correction factors for differential jet shapes for selected P_T bins. Statistical errors are included.

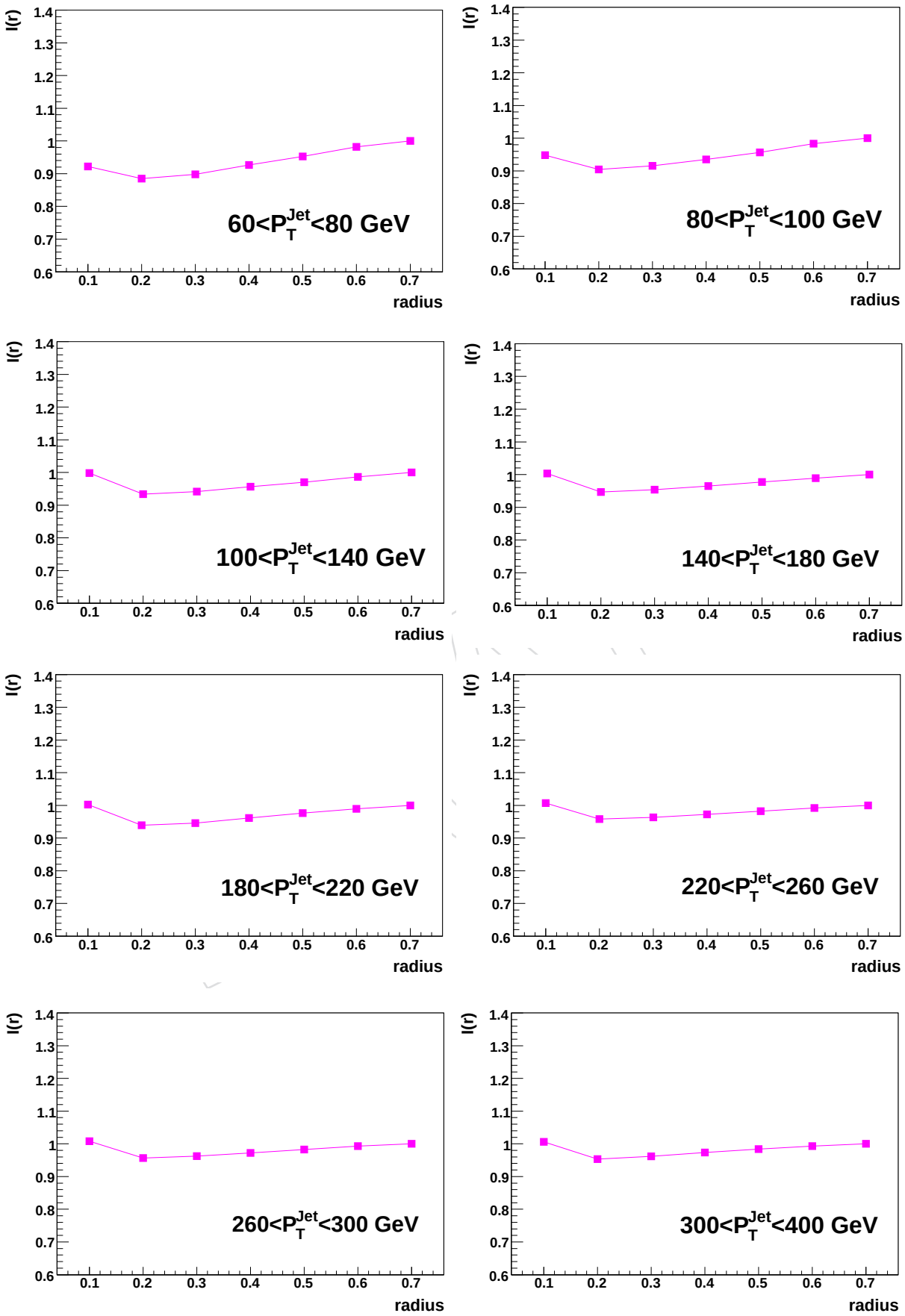

Figure 50: Correction factors for integrated jet shapes for selected P_T bins. Statistical errors are included.

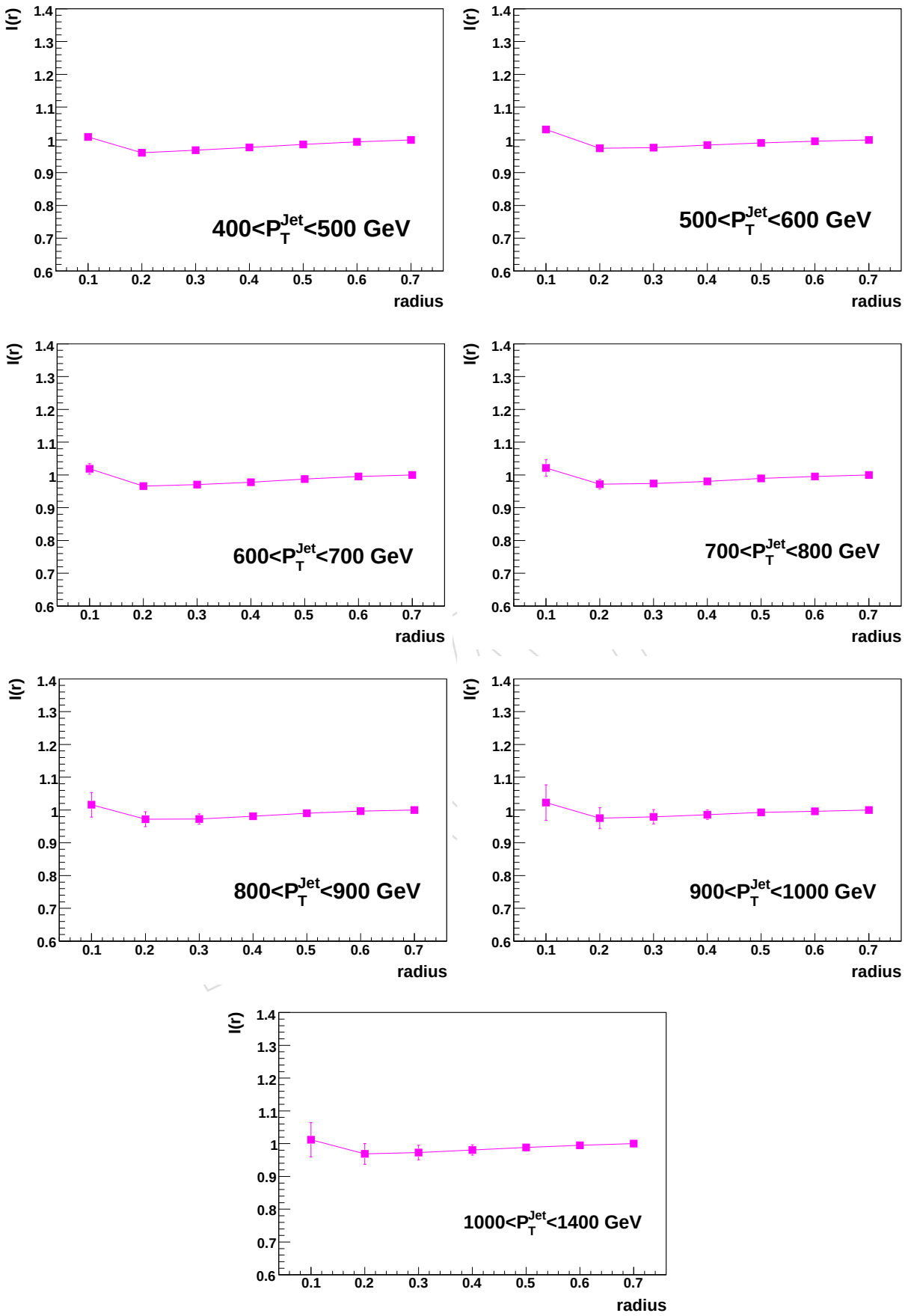

Figure 51: Correction factors for integrated jet shapes for selected P_T bins. Statistical errors are included.

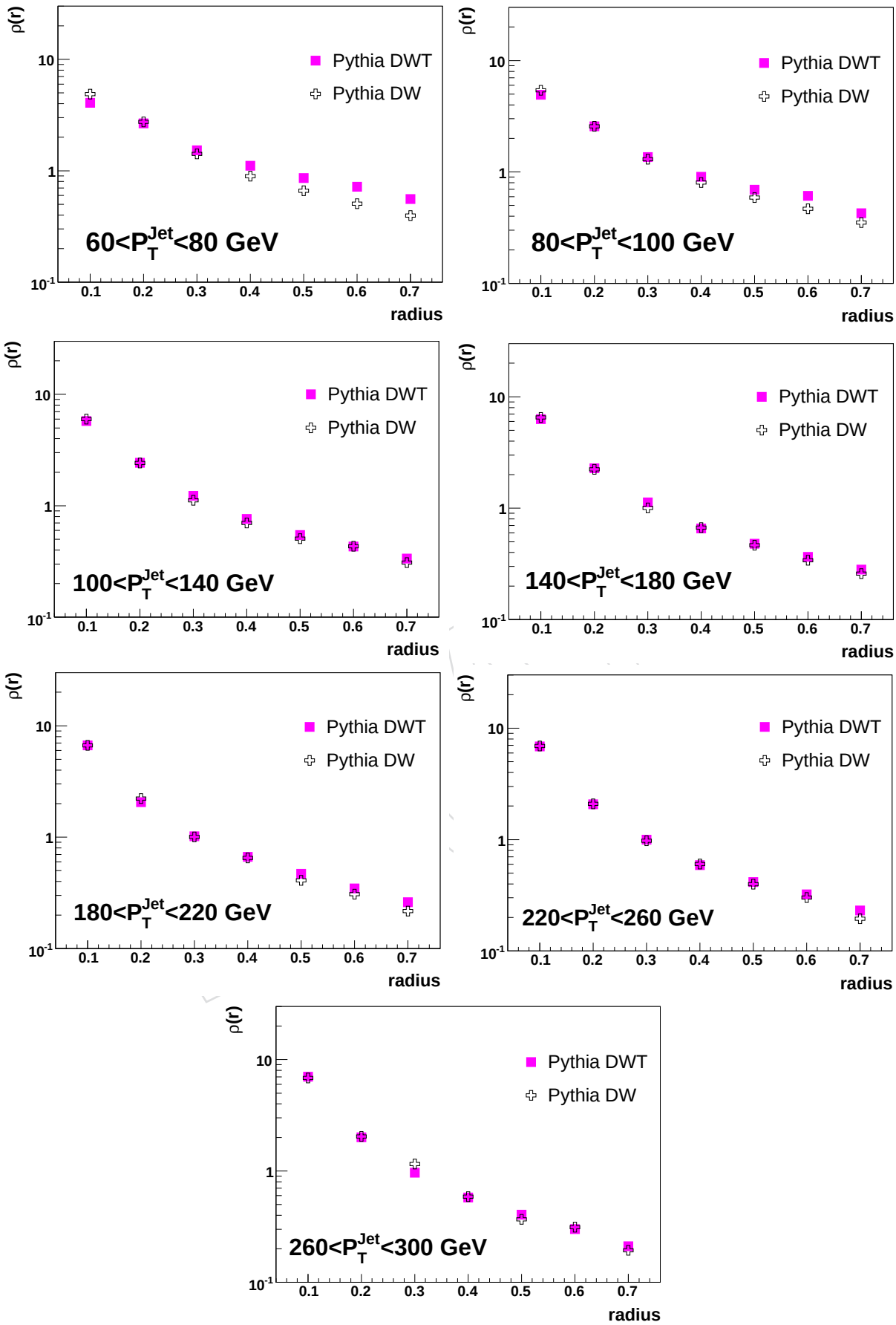

Figure 52: Comparison of differential jet shapes for PYHTIA tunes DWT and DW in selected P_T bins. Statistical errors are included.

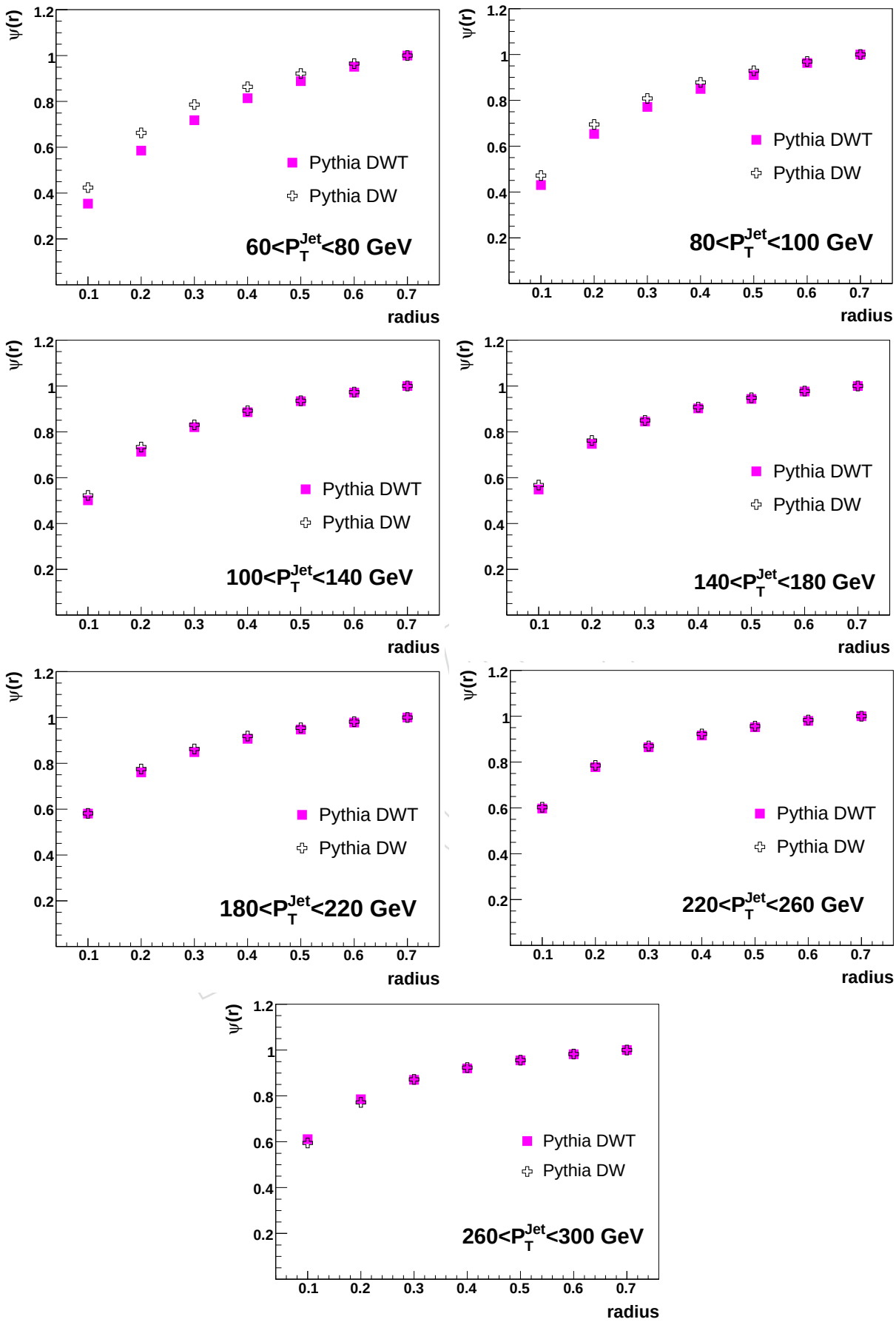

Figure 53: Comparison of integrated jet shapes for PYHTIA tunes DWT and DW in selected P_T bins. Statistical errors are included.

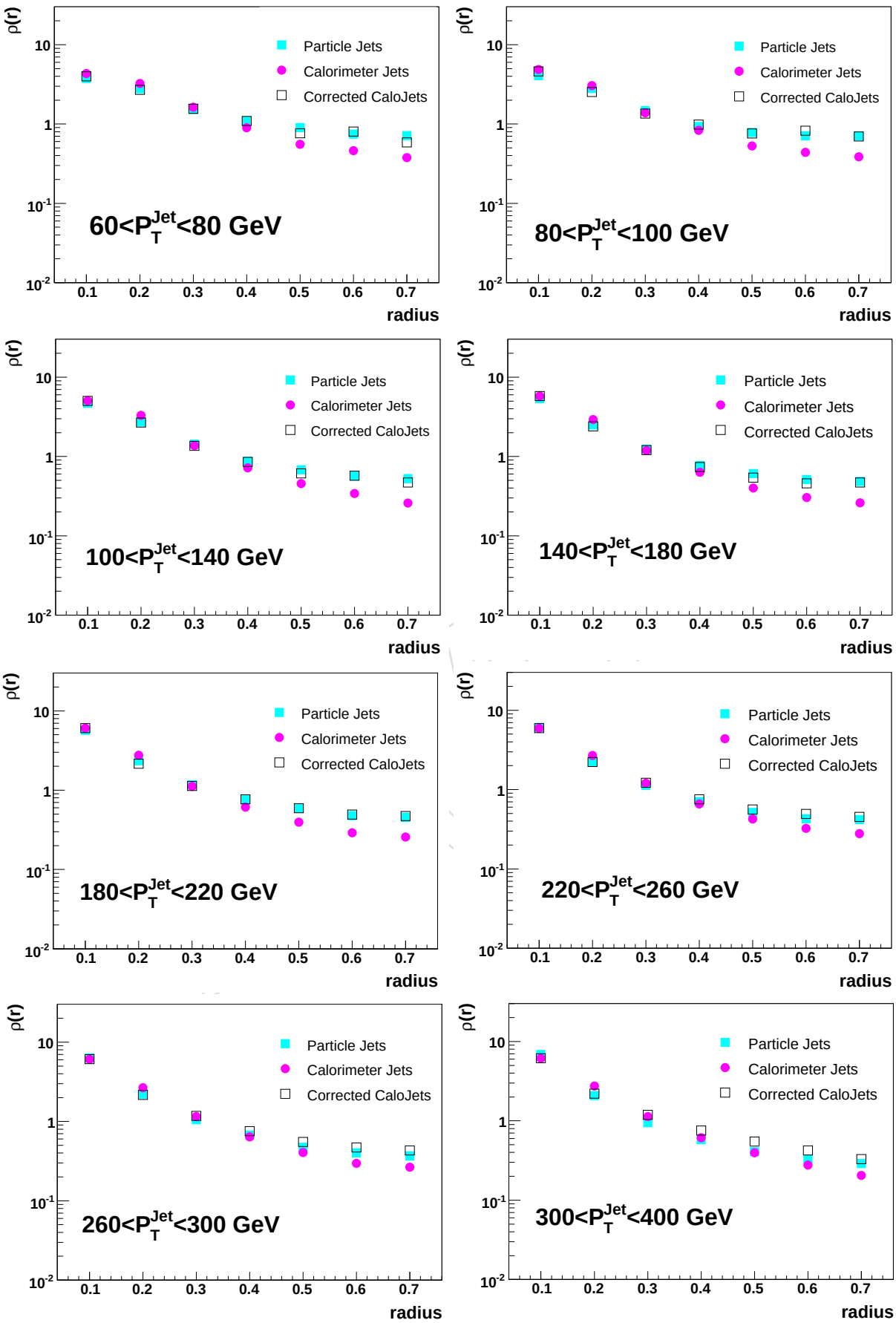

Figure 54: Differential jet shapes for selected P_T bins in multijet samples generated with ALPGEN. Statistical errors are included.

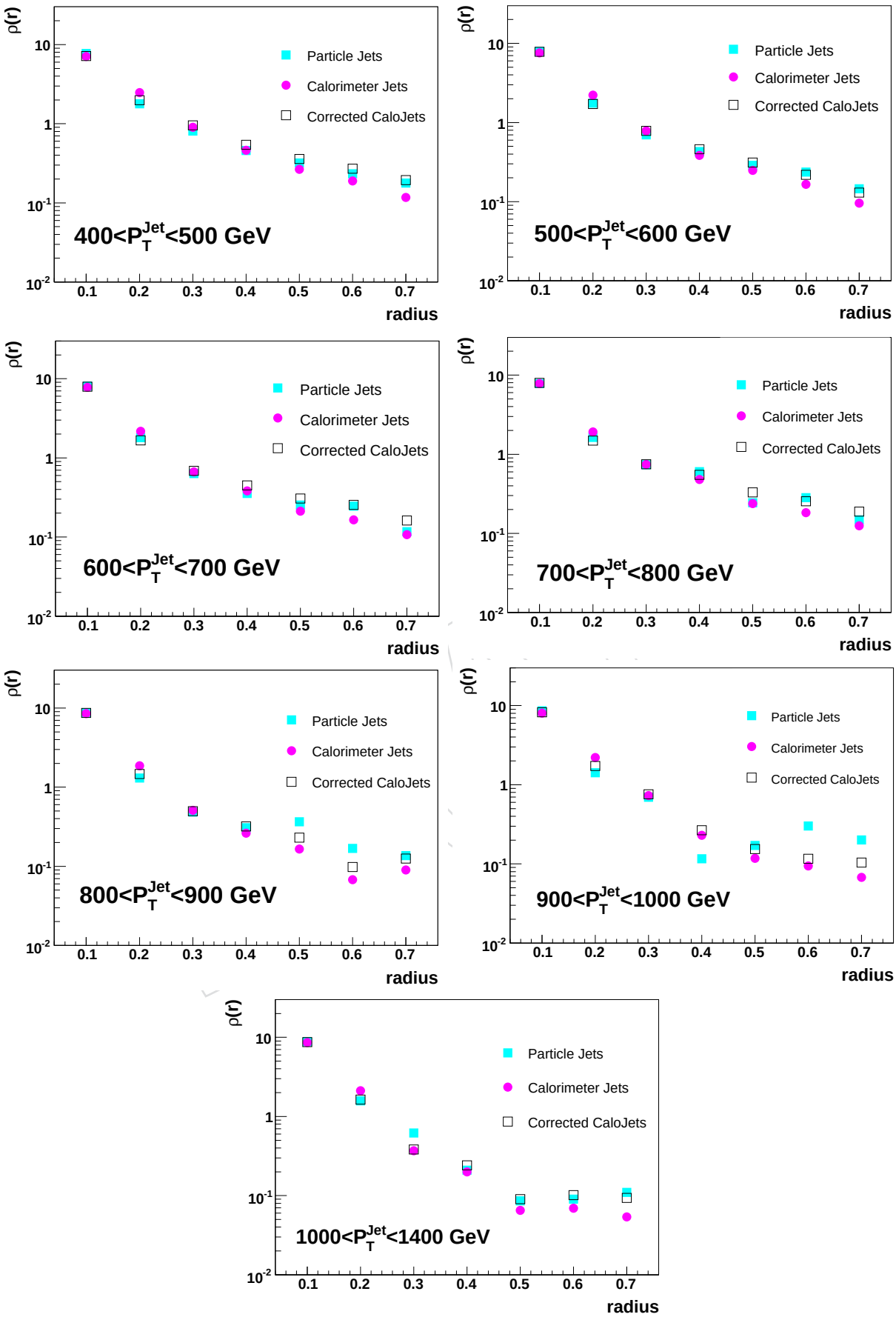

Figure 55: Differential jet shapes for selected P_T bins in multijet samples generated with ALPGEN.

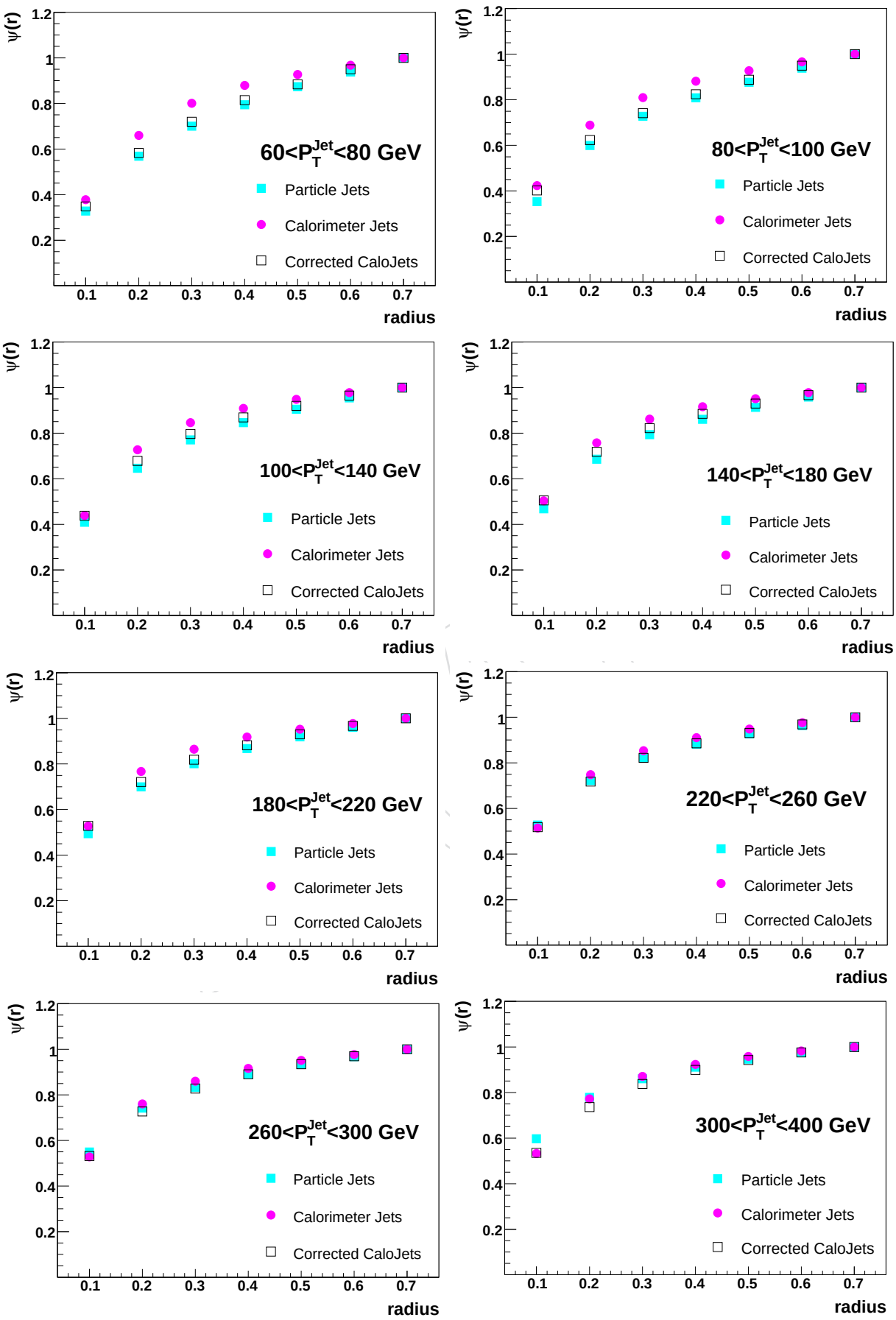

Figure 56: Integrated jet shapes for selected P_T bins in multijet samples generated with ALPGEN.

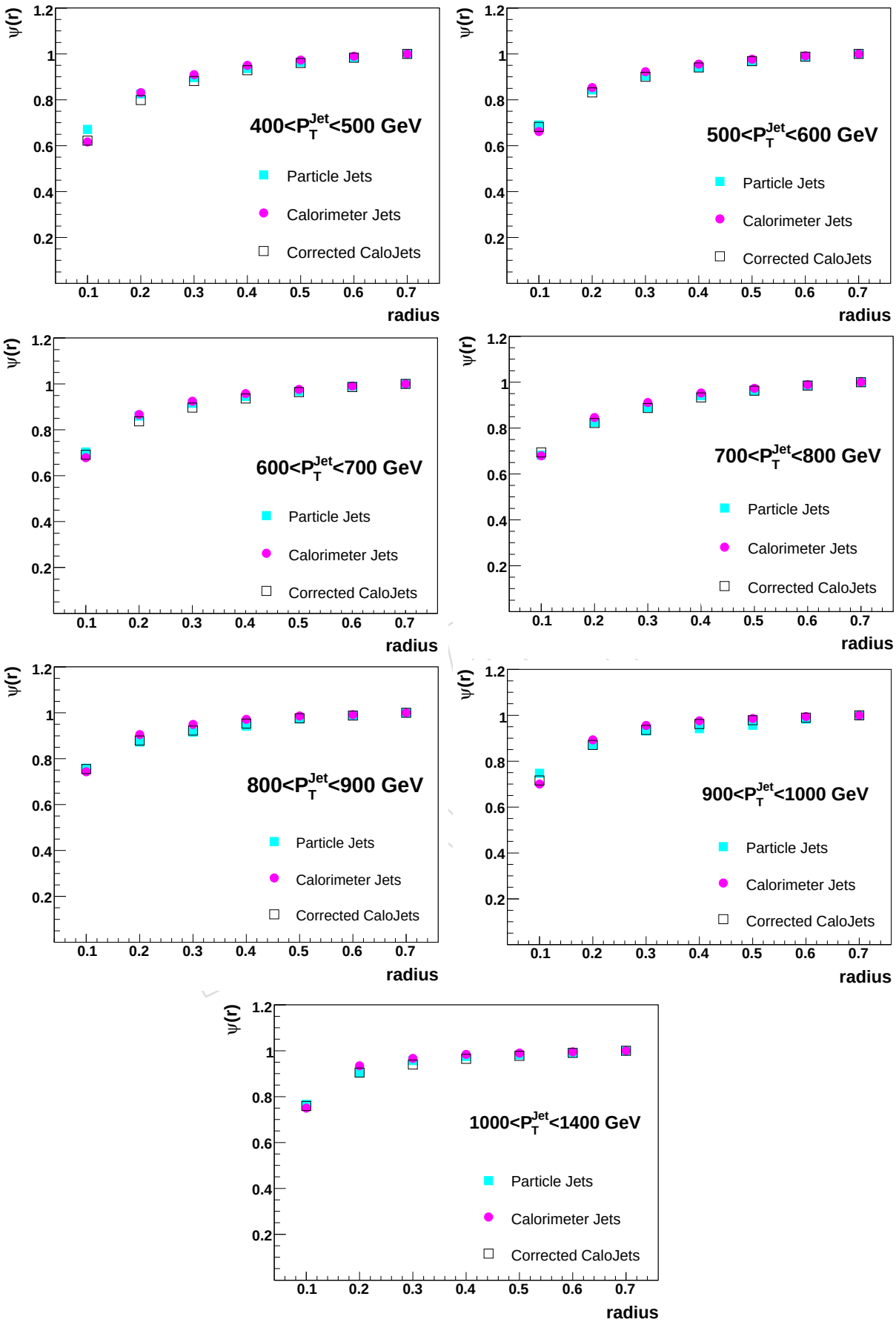

Figure 57: Integrated jet shapes for selected P_T bins in multijet samples generated with ALPGEN.

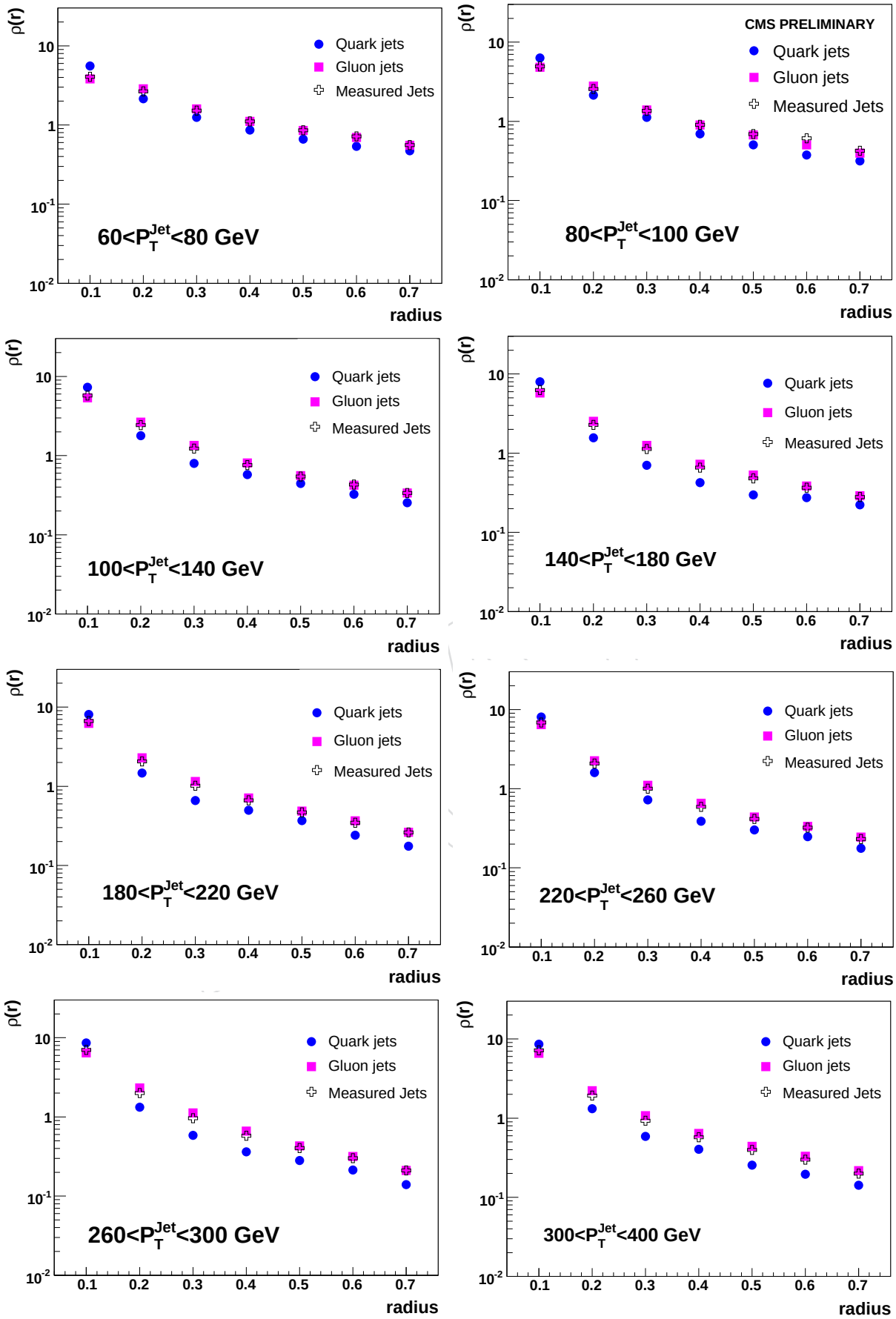

Figure 58: Comparison of quark and gluon differential jet shapes to simulated data in selected P_T bins. Statistical errors are included.

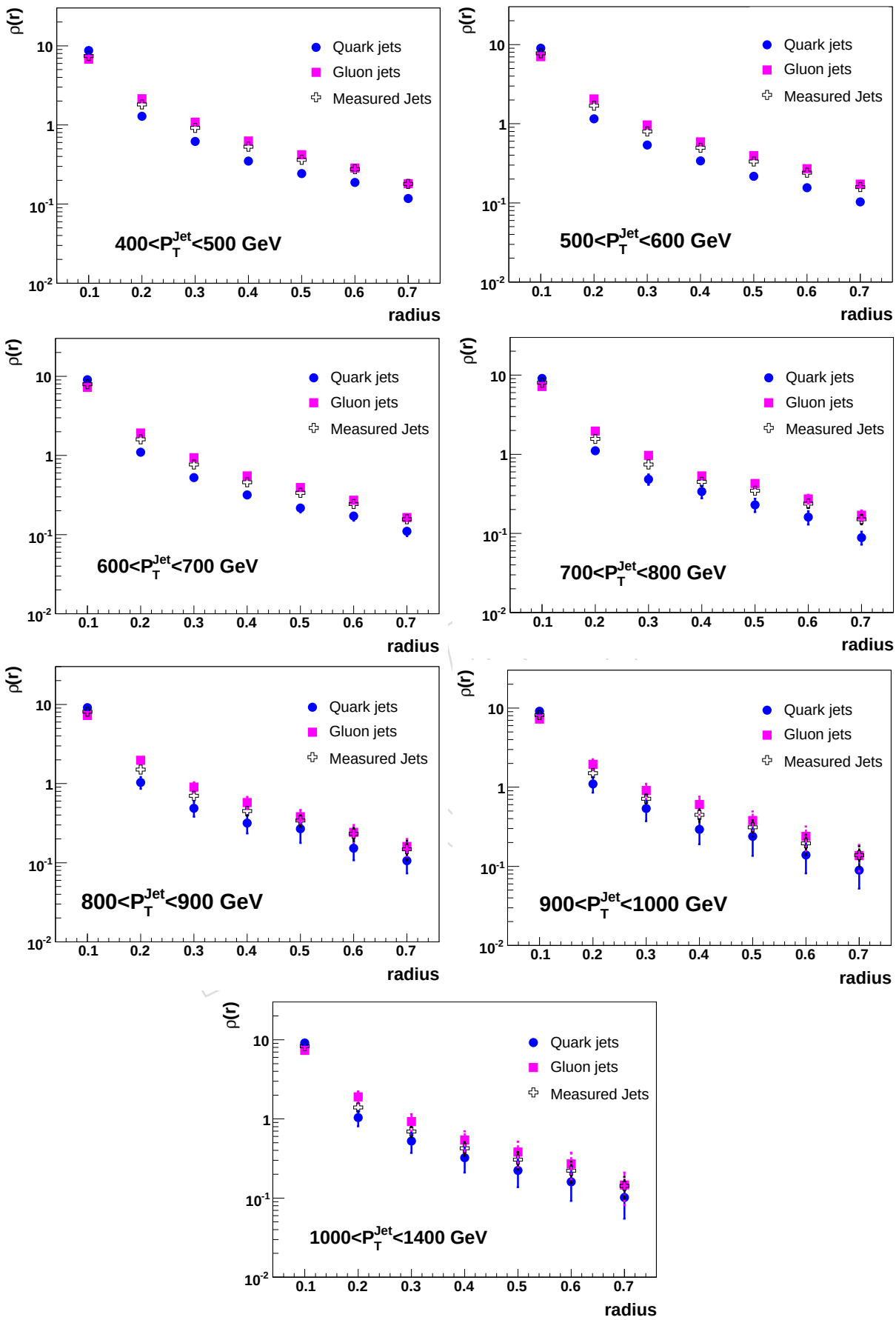

Figure 59: Comparison of quark and gluon differential jet shapes to simulated data in selected P_T bins. Statistical errors are included.

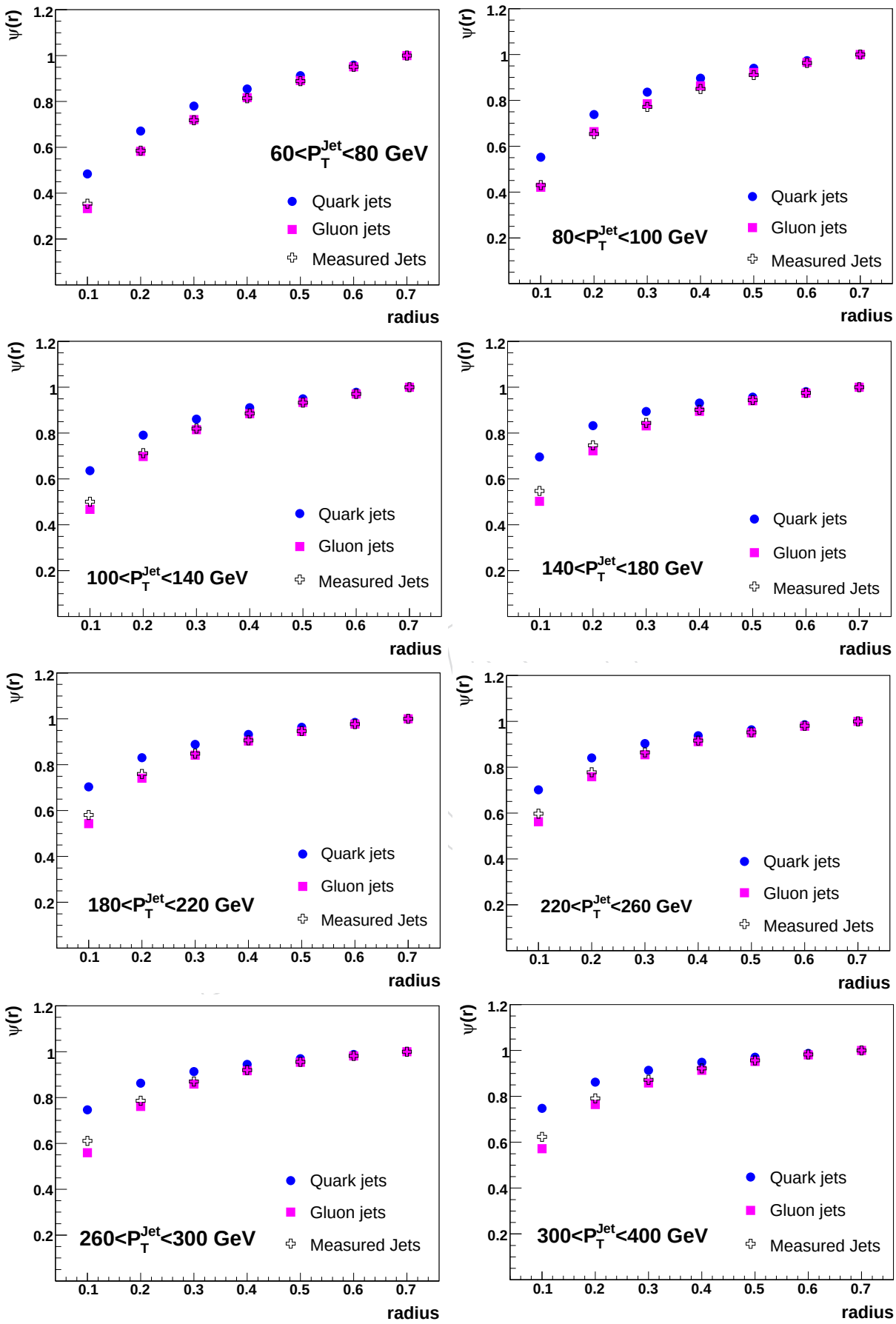

Figure 60: Comparison of quark and gluon integrated jet shapes to simulated data in selected P_T bins. Statistical errors are included.

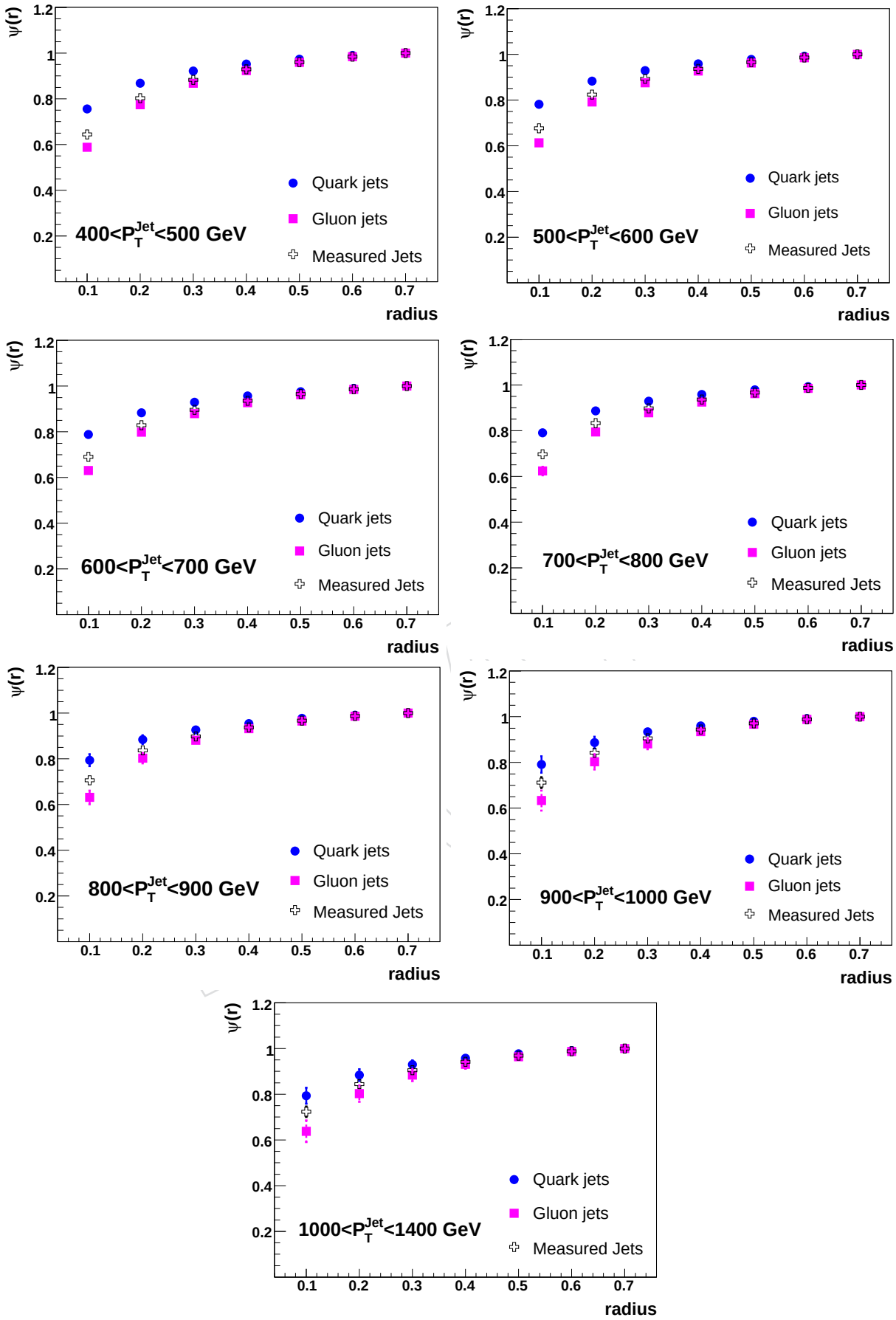

Figure 61: Comparison of quark and gluon integrated jet shapes to simulated data in selected P_T bins. Statistical errors are included.

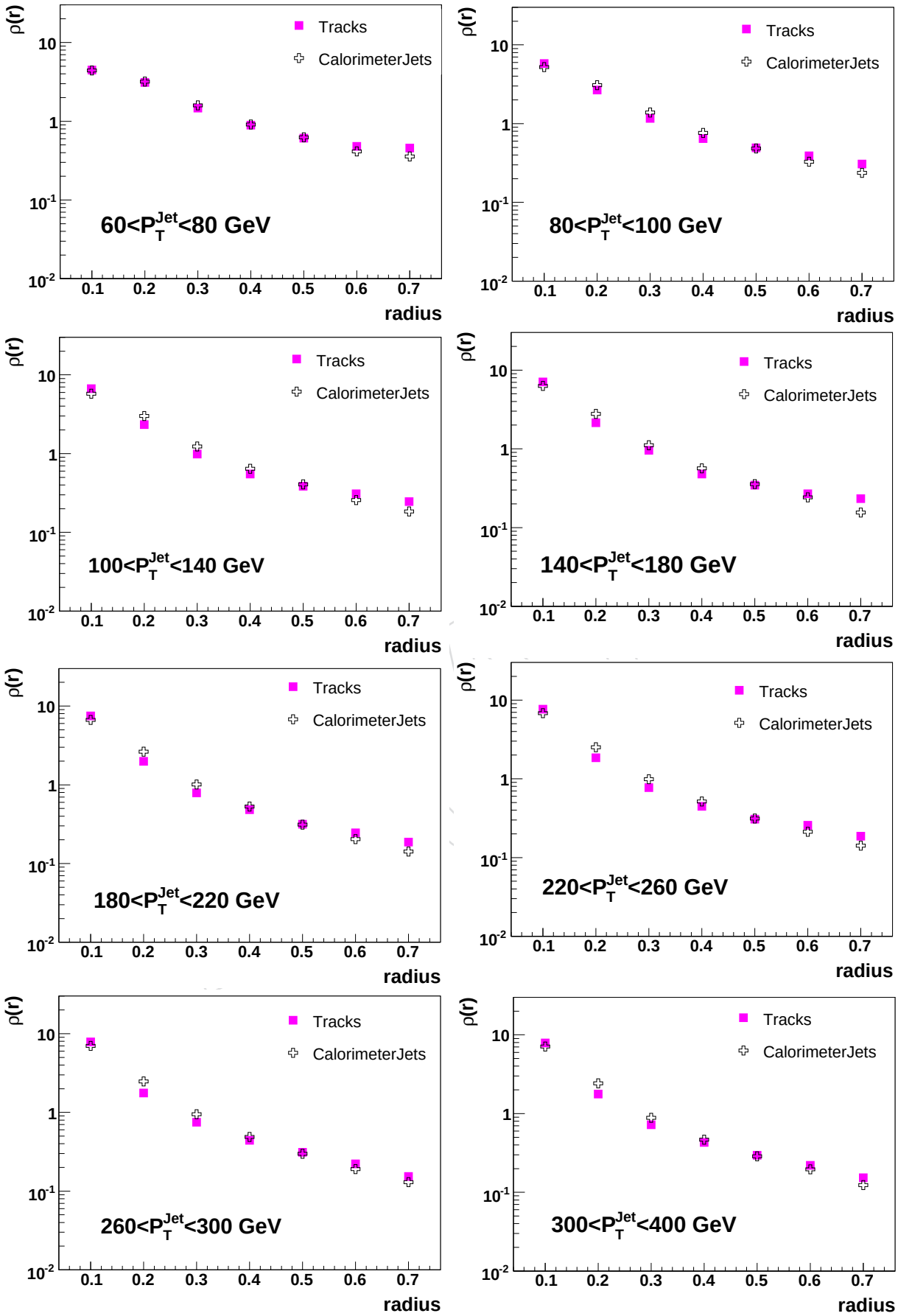

Figure 62: Comparison of the differential track jet shapes to the calorimeter jet shapes in simulated data for selected P_T bins. Statistical errors are included.

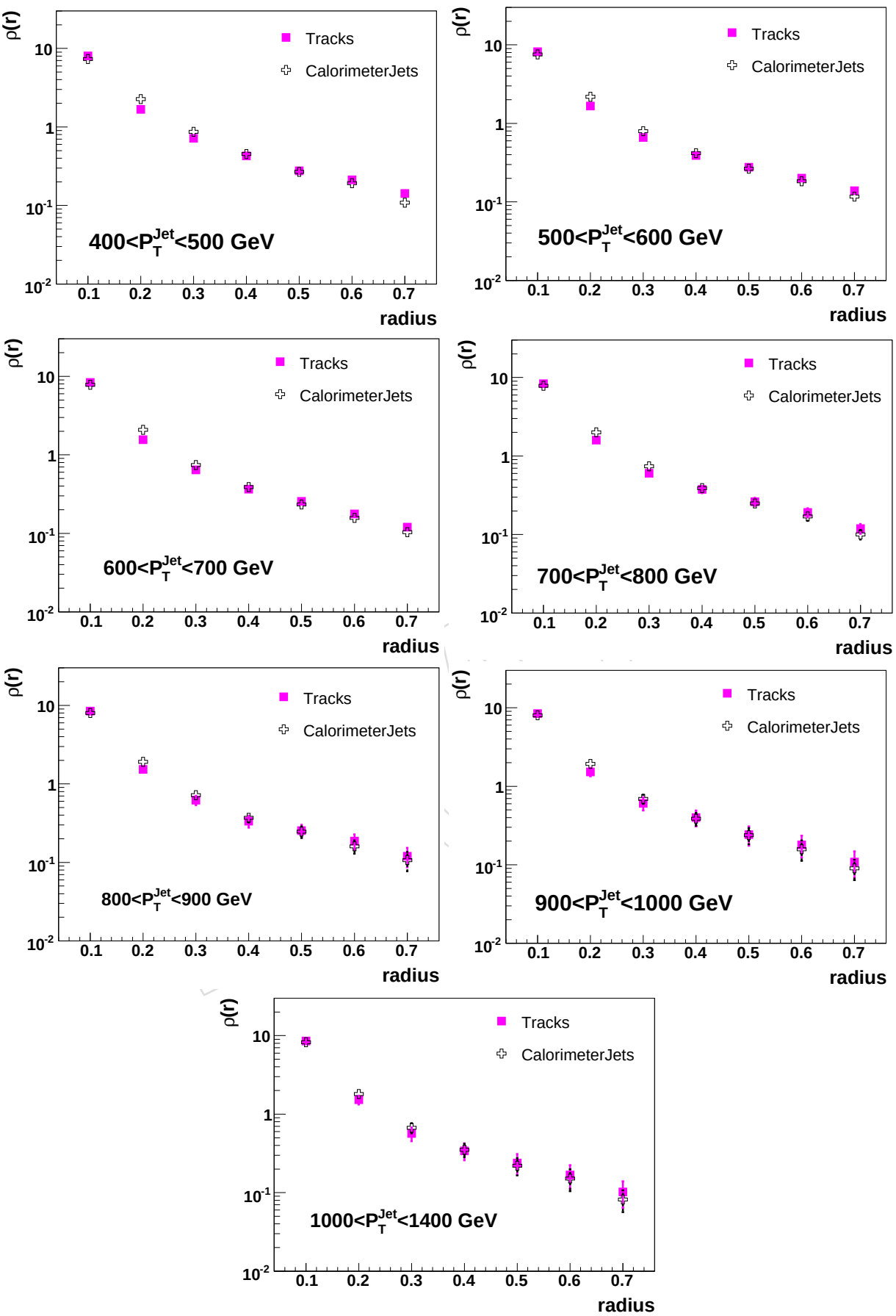

Figure 63: Comparison of the differential track jet shapes to the calorimeter jet shapes in simulated data for selected P_T bins. Statistical errors are included.

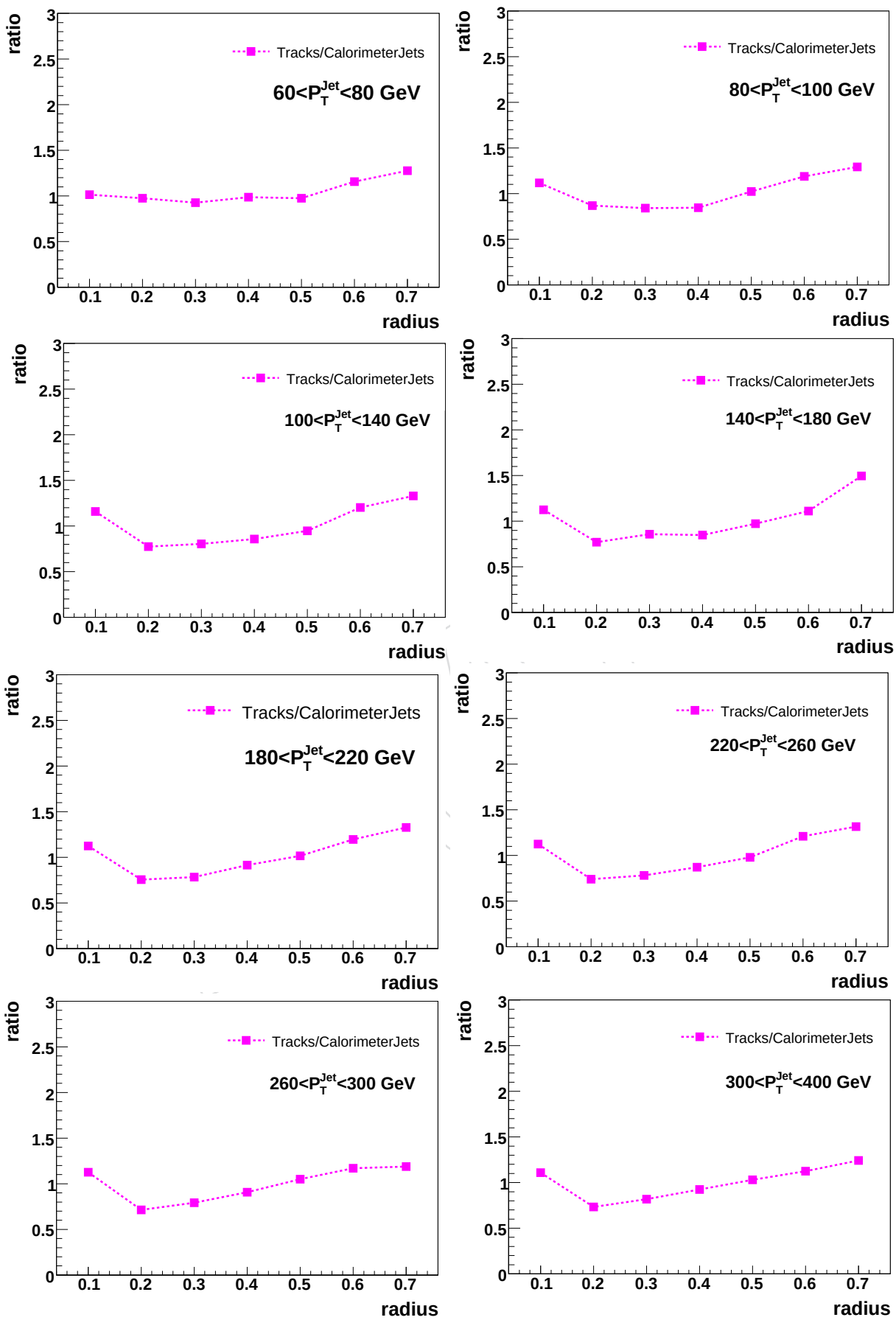

Figure 64: Ratio of the track differential jet shapes to the calorimeter jet shapes in simulated data for selected P_T bins. Statistical errors are included.

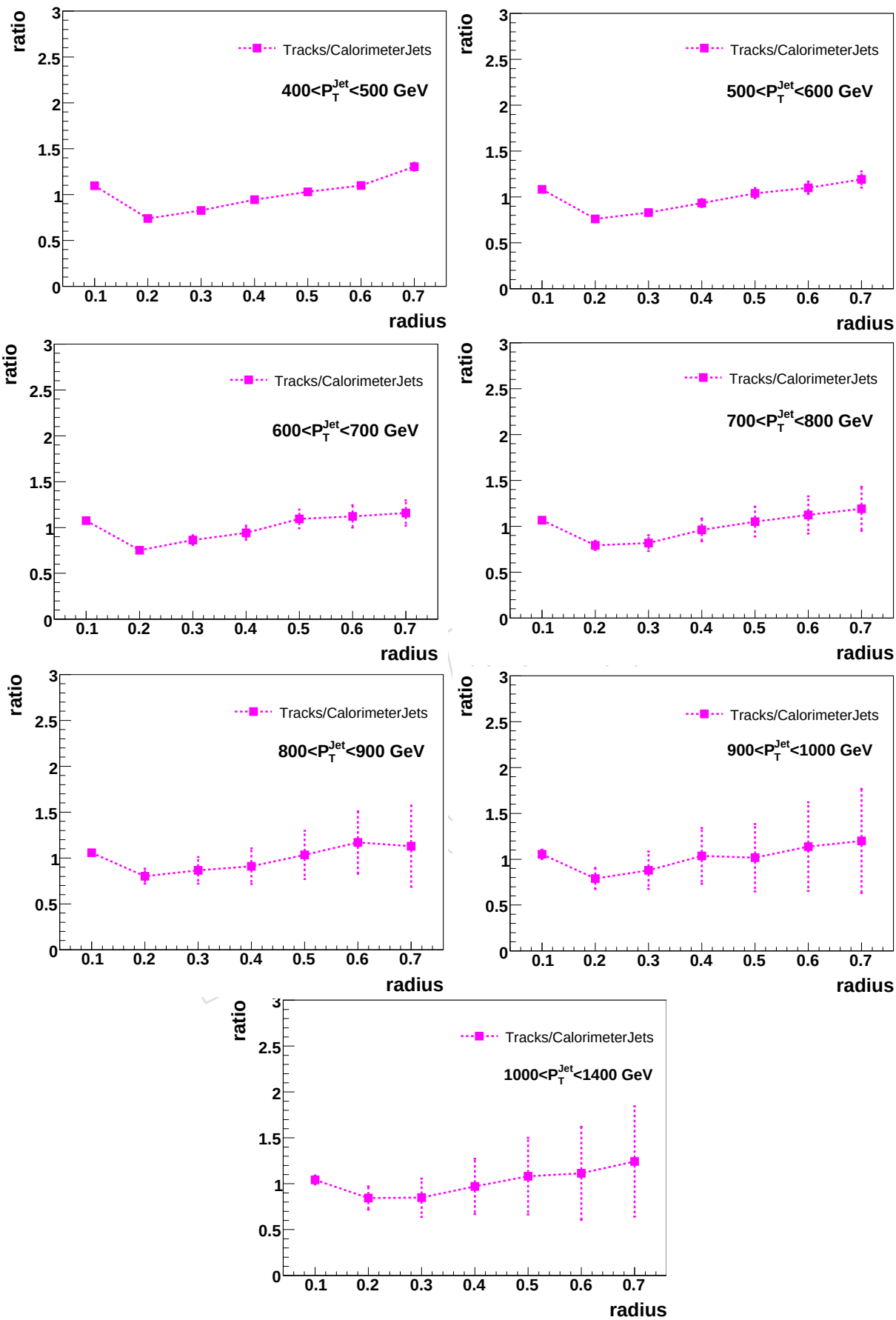

Figure 65: Ratio of the track integrated jet shapes to the calorimeter jet shapes in simulated data for selected P_T bins. Statistical errors are included.

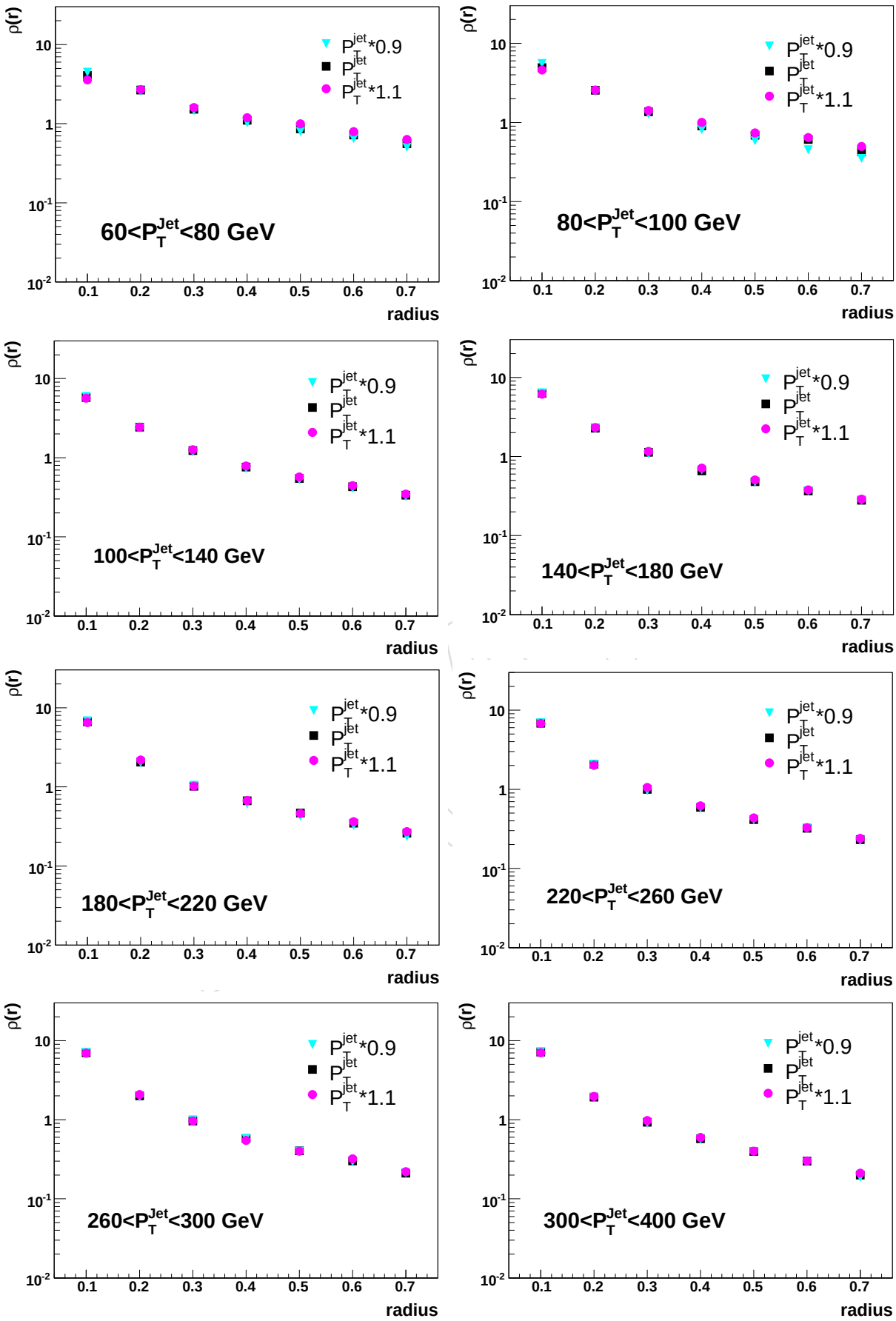

Figure 66: Differential jet shapes for ±10% changes in energy scale for selected P_T bins. Statistical errors are included.

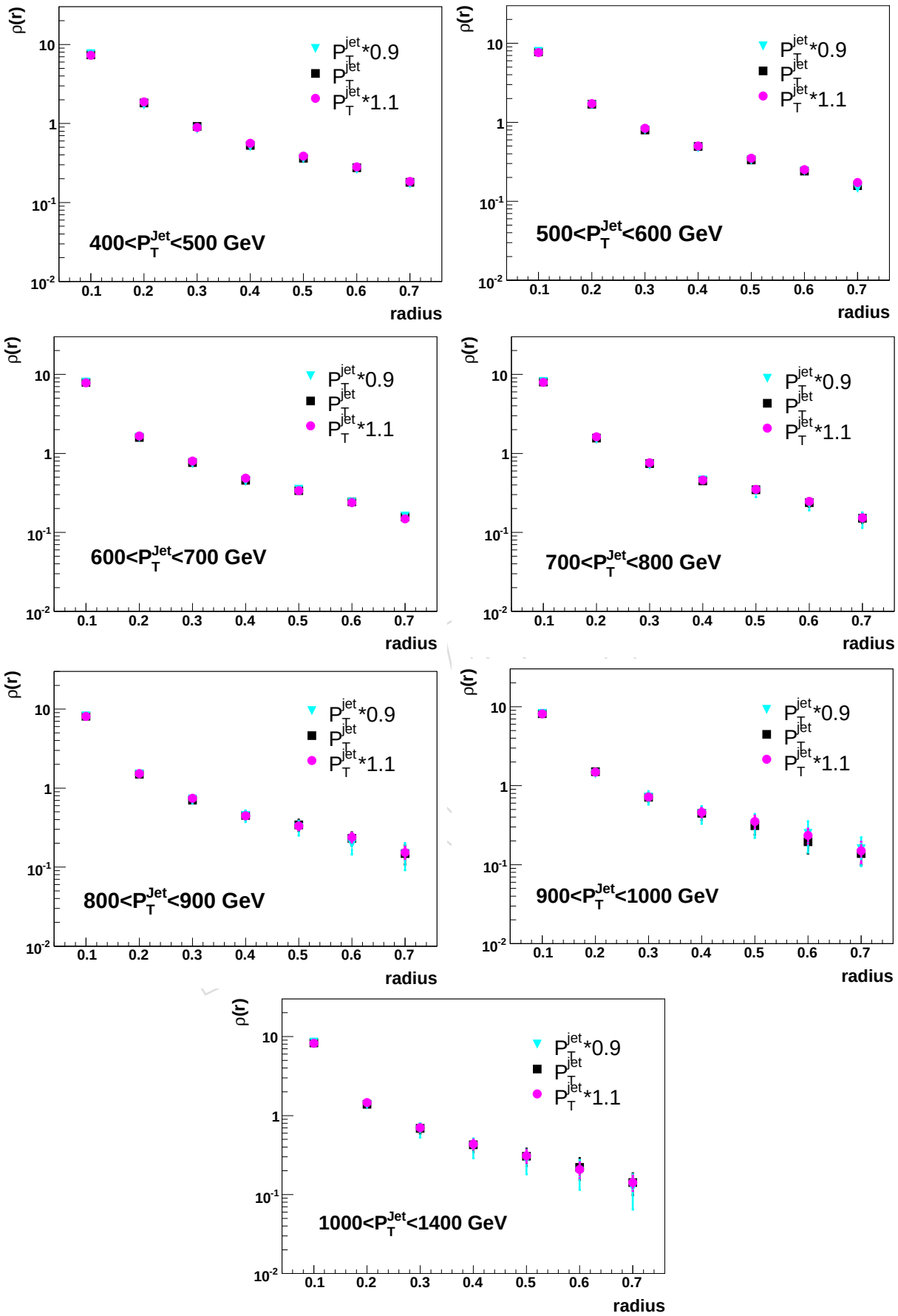

Figure 67: Differential jet shapes for ±10% changes in energy scale for selected P_T bins. Statistical errors are included.

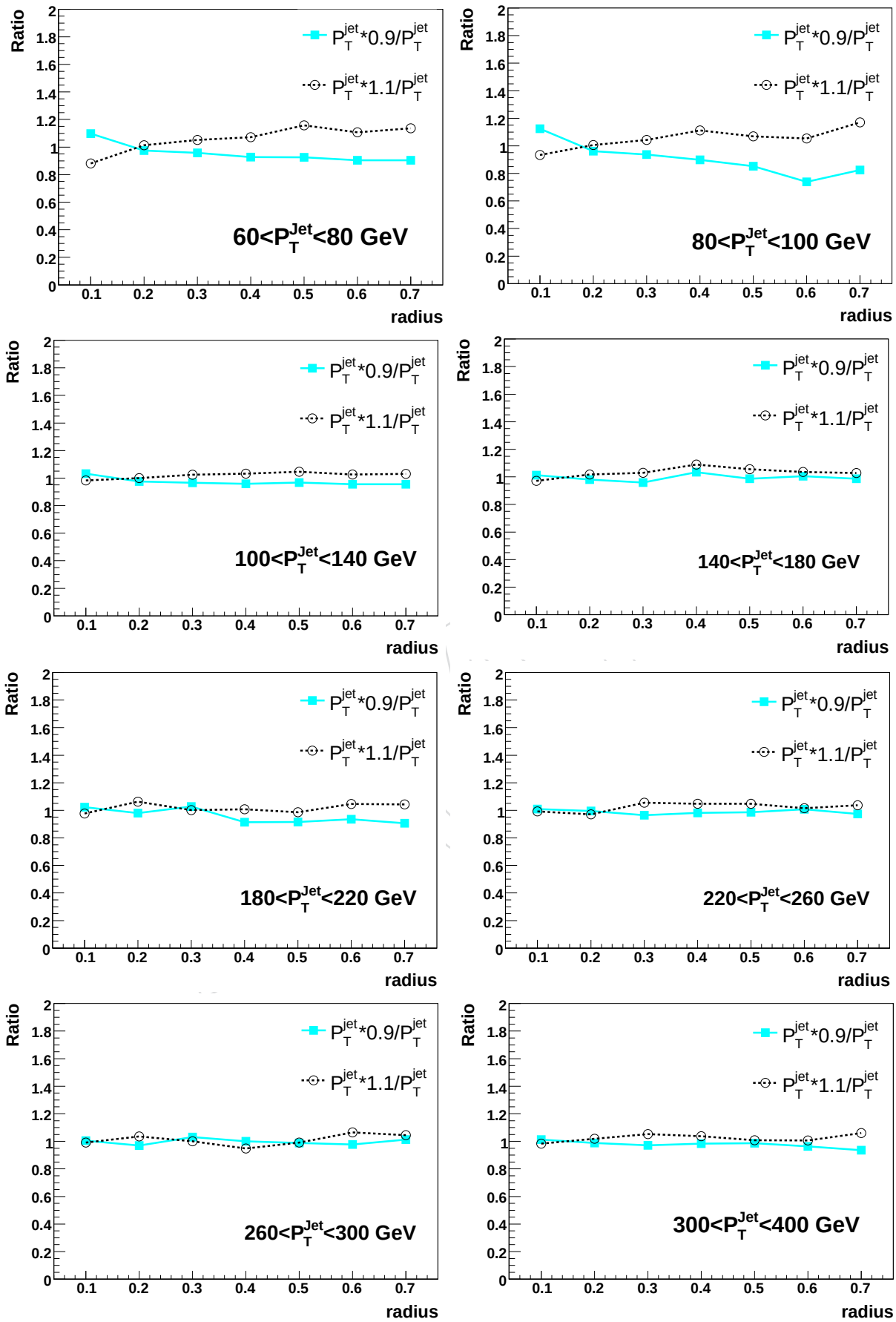

Figure 68: Effect of changing jet energy scale for differential jet shapes for selected P_T bins. Only statistical errors are included.

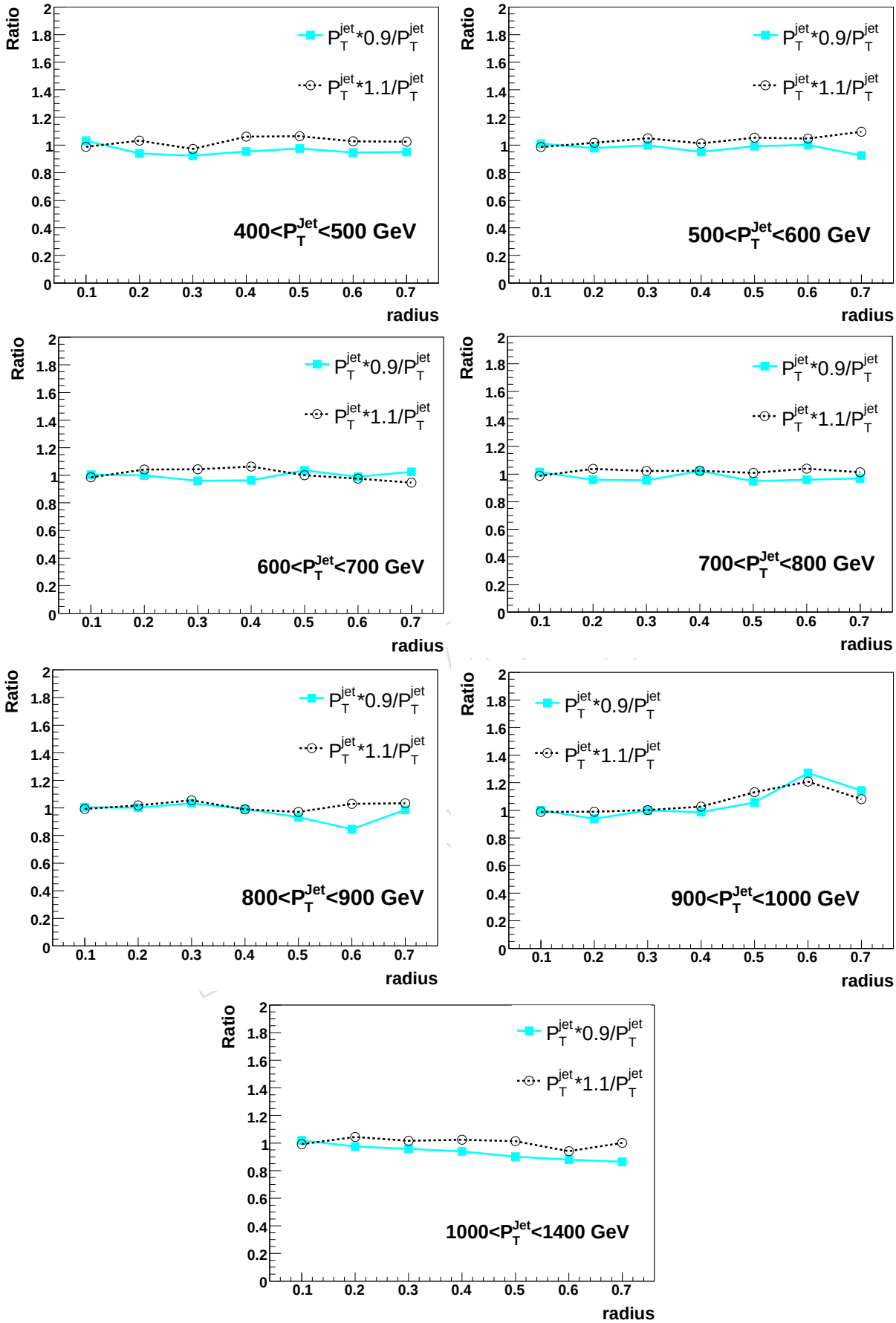

Figure 69: Effect of changing jet energy scale for differential jet shapes for selected P_T bins. Only statistical errors are included.

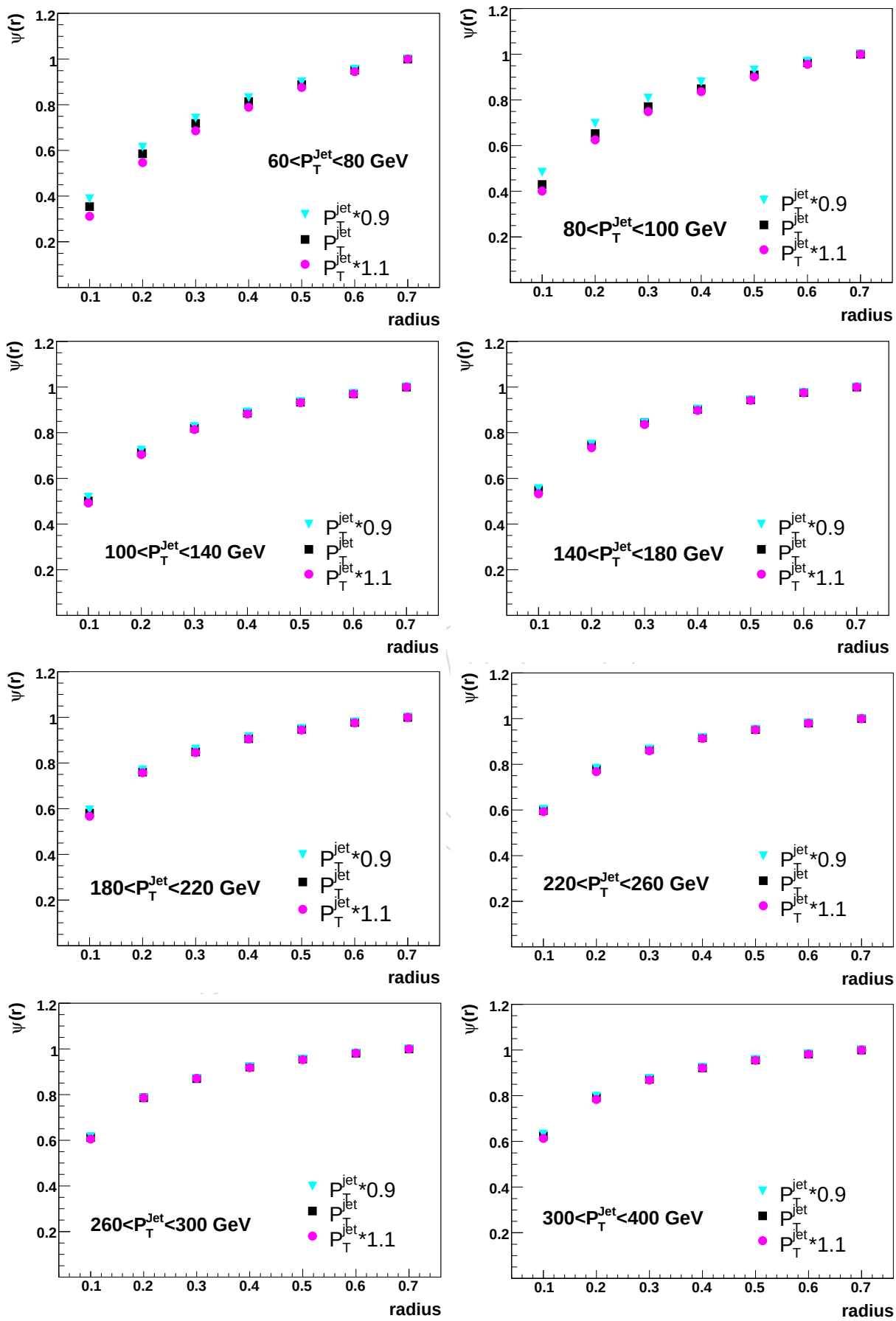

Figure 70: Integrated jet shapes for ±10% changes in energy scale for selected P_T bins. Statistical errors are included.

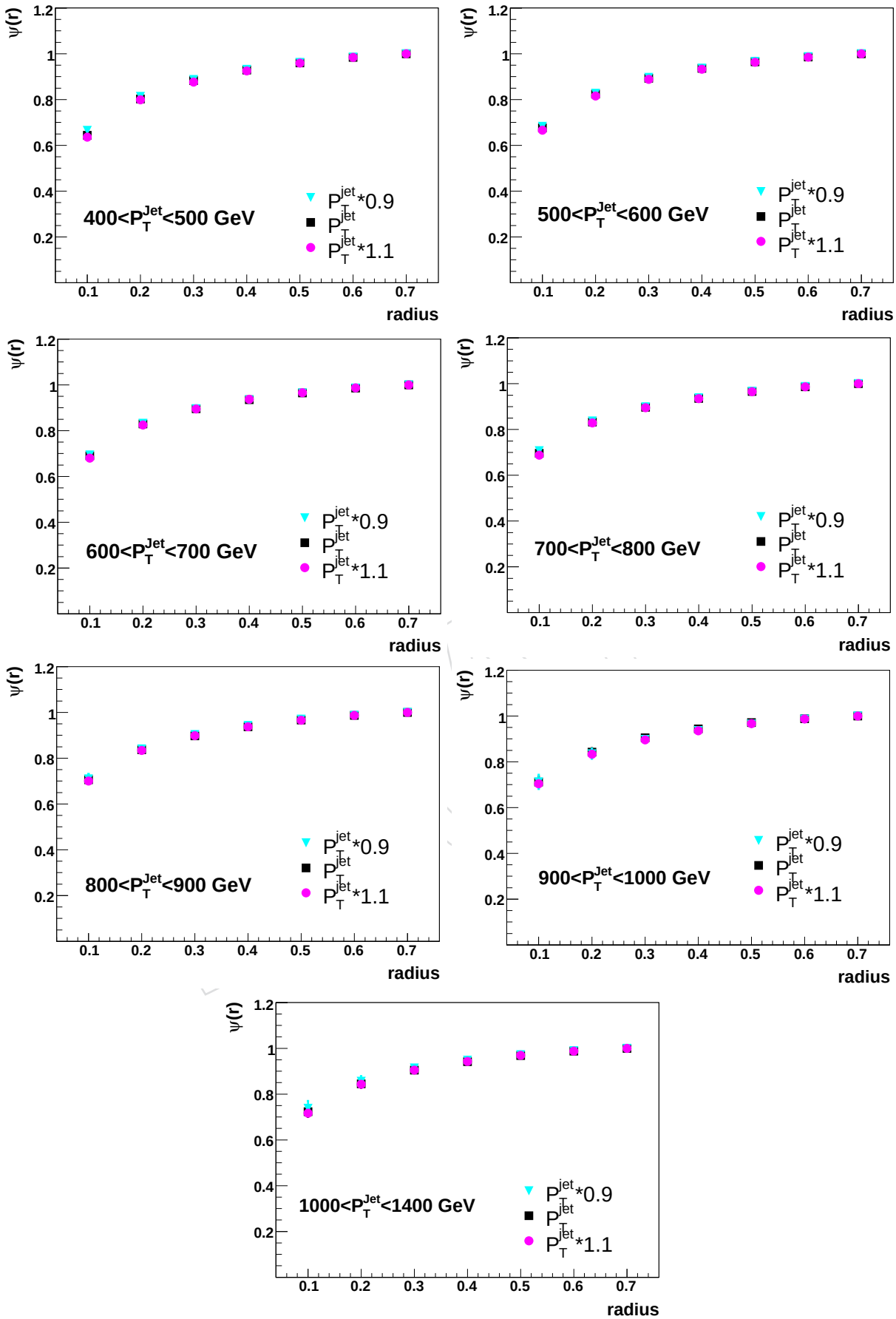

Figure 71: Integrated jet shapes for ±10% changes in energy scale for selected P_T bins. Statistical errors are included.

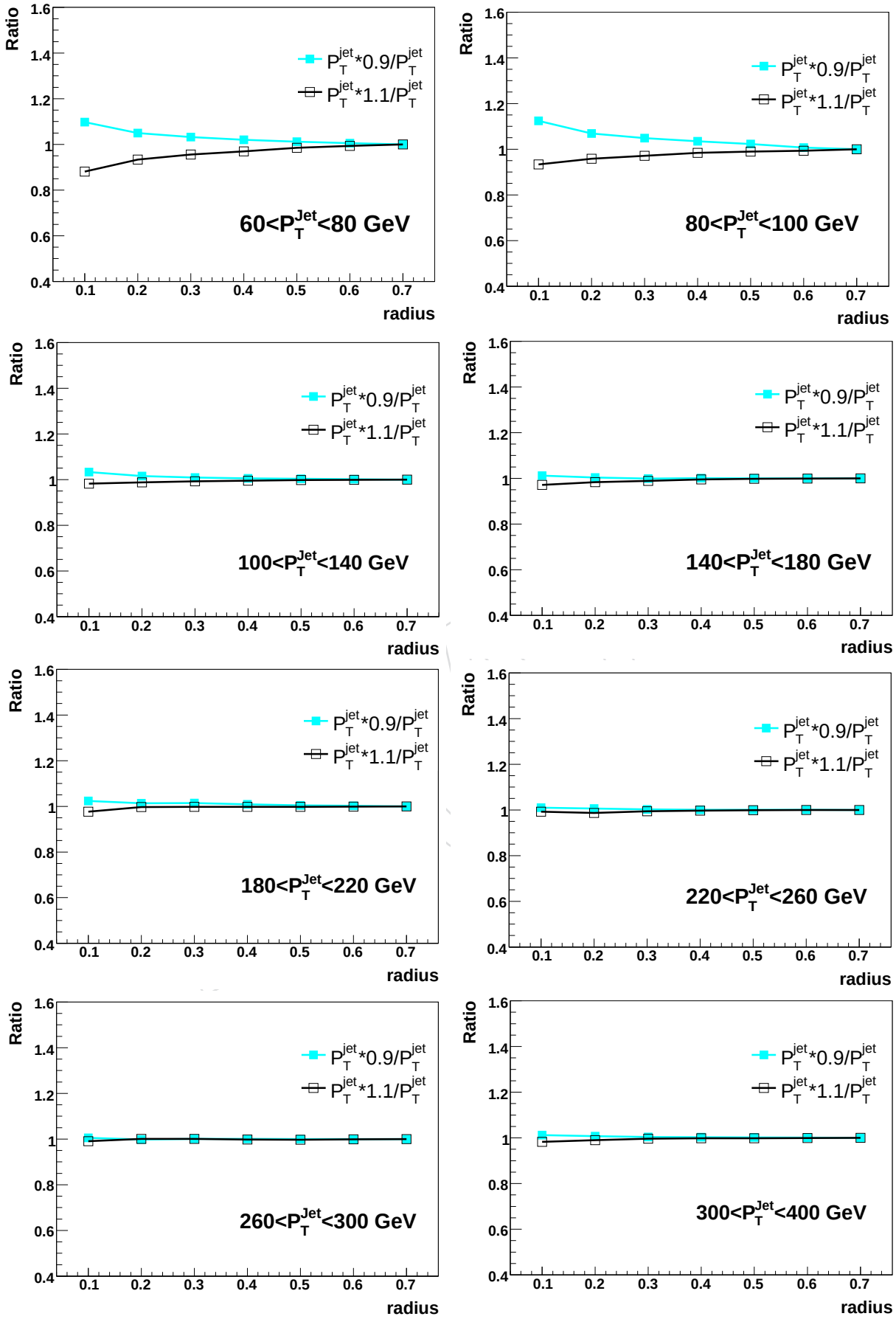

Figure 72: Effect of changing jet energy scale for integrated jet shapes for selected P_T bins. Only statistical errors are included.

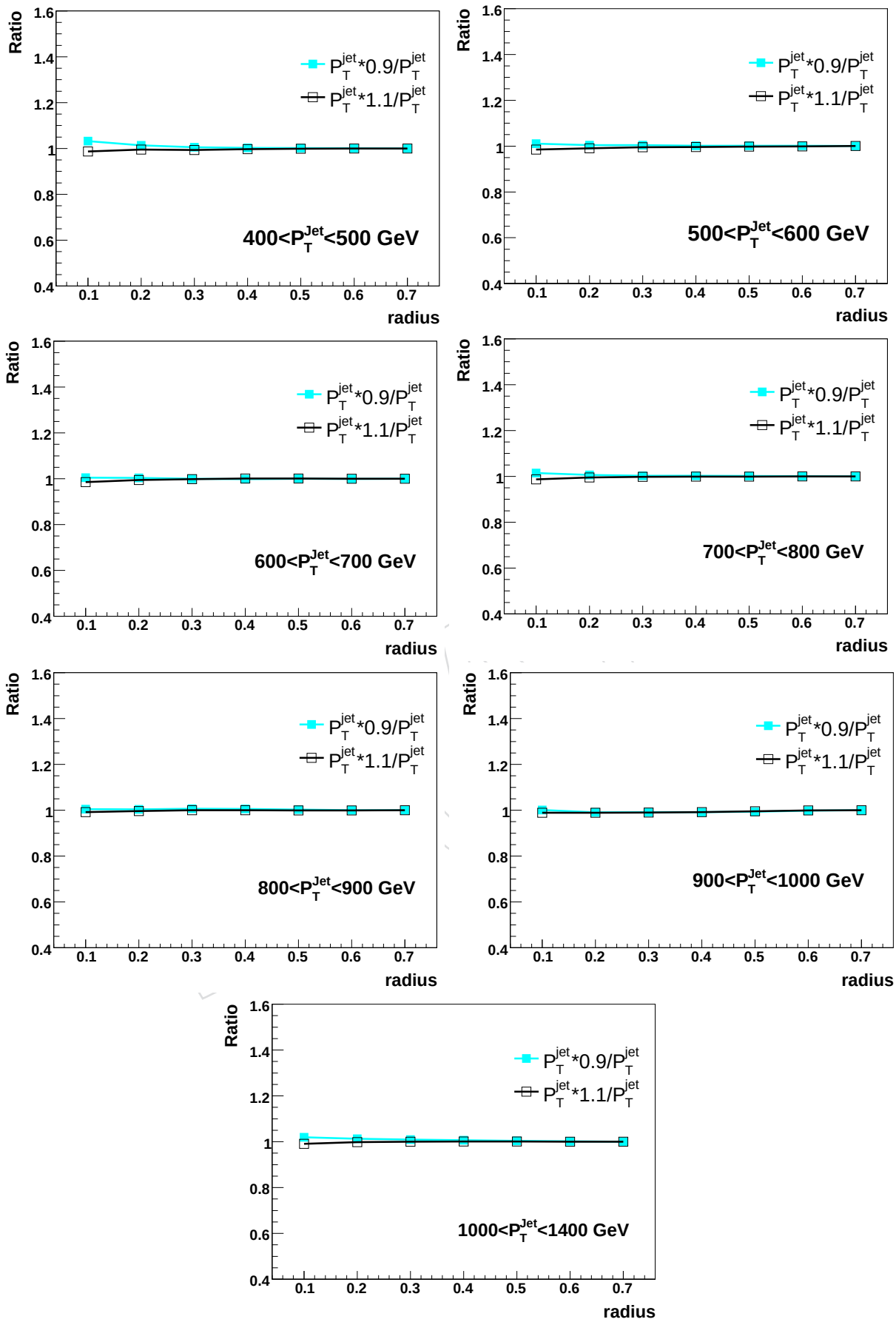

Figure 73: Effect of changing jet energy scale for integrated jet shapes for selected P_T bins. Only statistical errors are included.

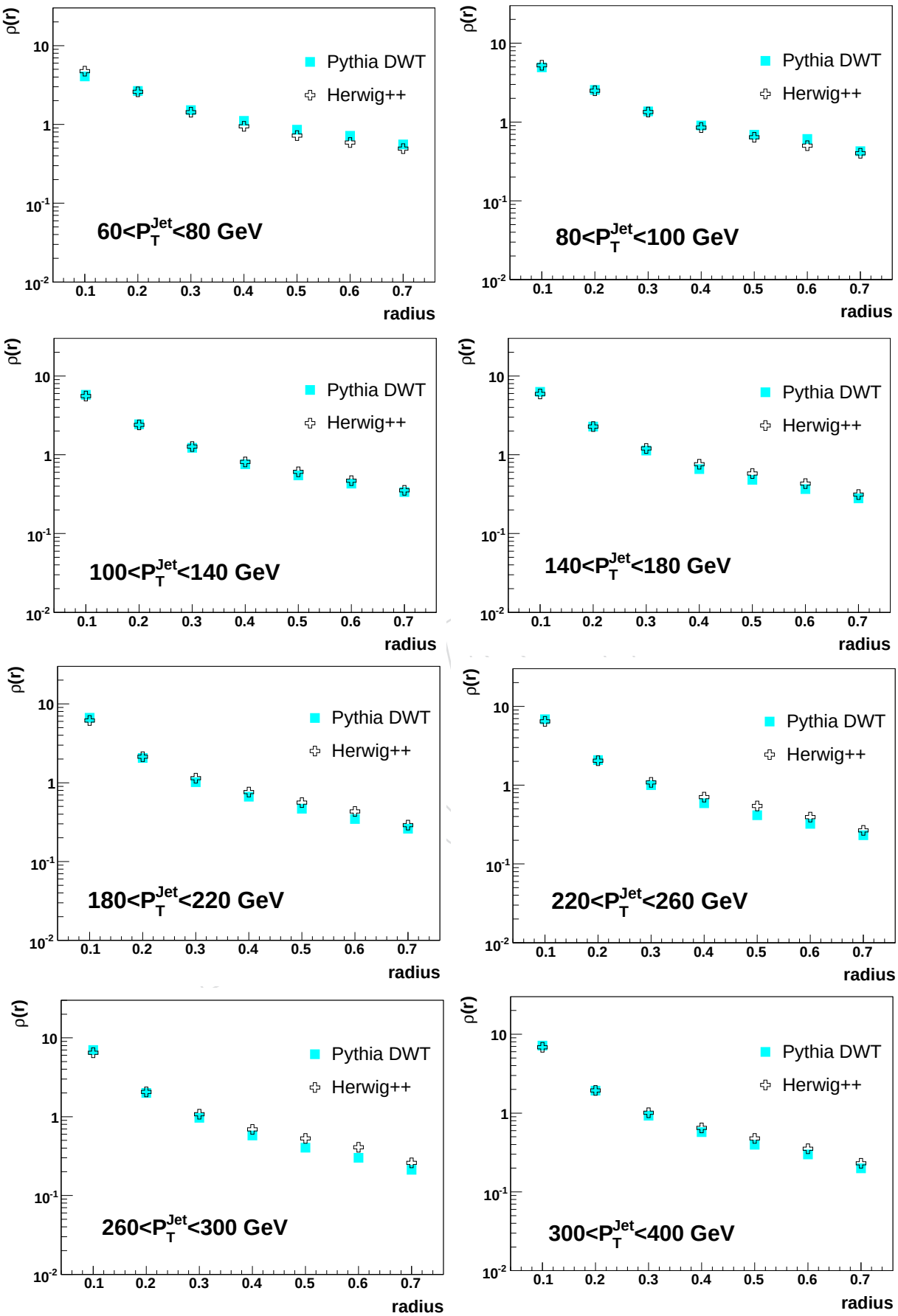

Figure 74: Comparison of particle level differential jet shapes from HERWIG++ and PYTHIA for selected P_T bins. Statistical errors are included.

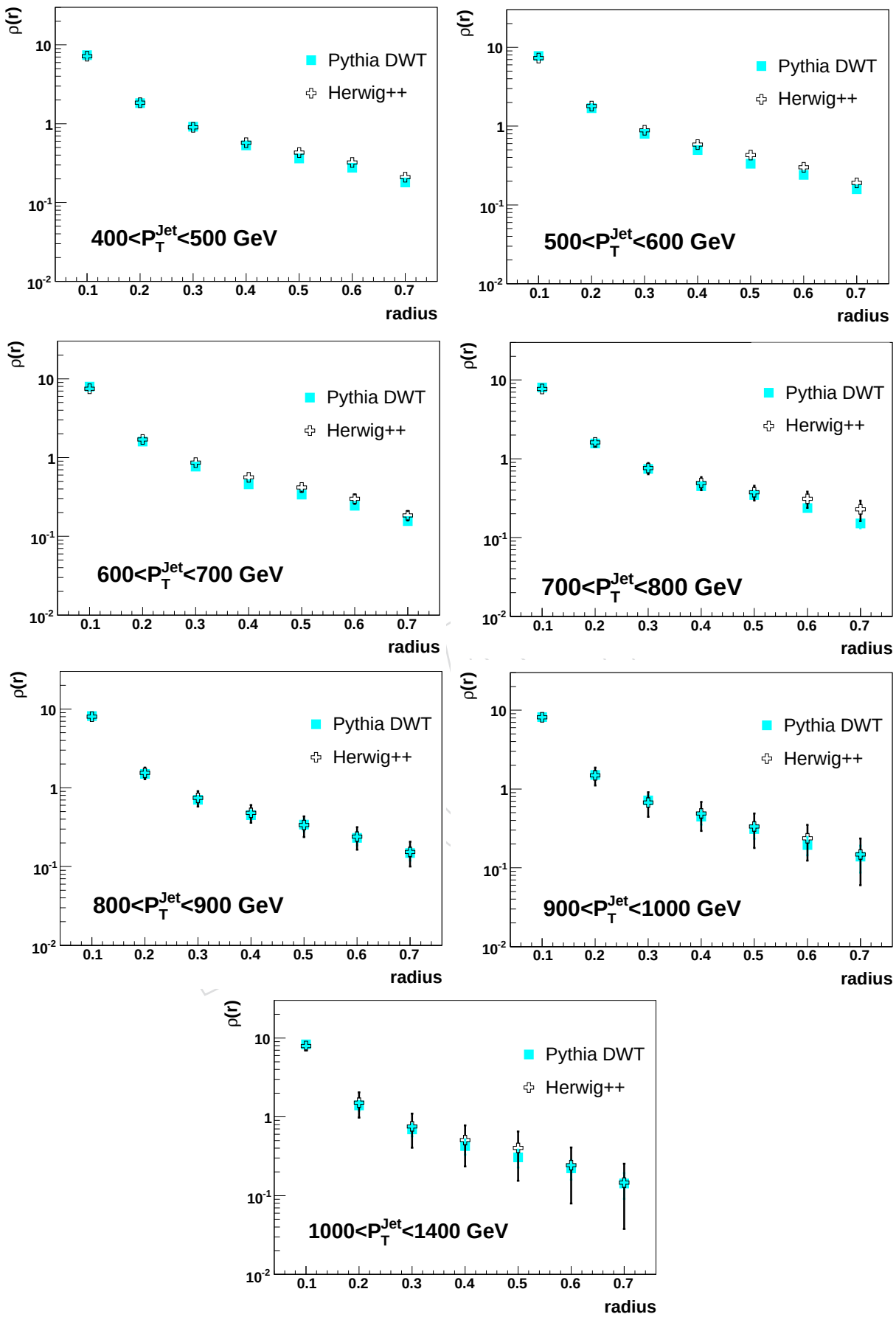

Figure 75: Comparison of particle level differential jet shapes from HERWIG++ and PYTHIA for selected P_T bins. Statistical errors are included.

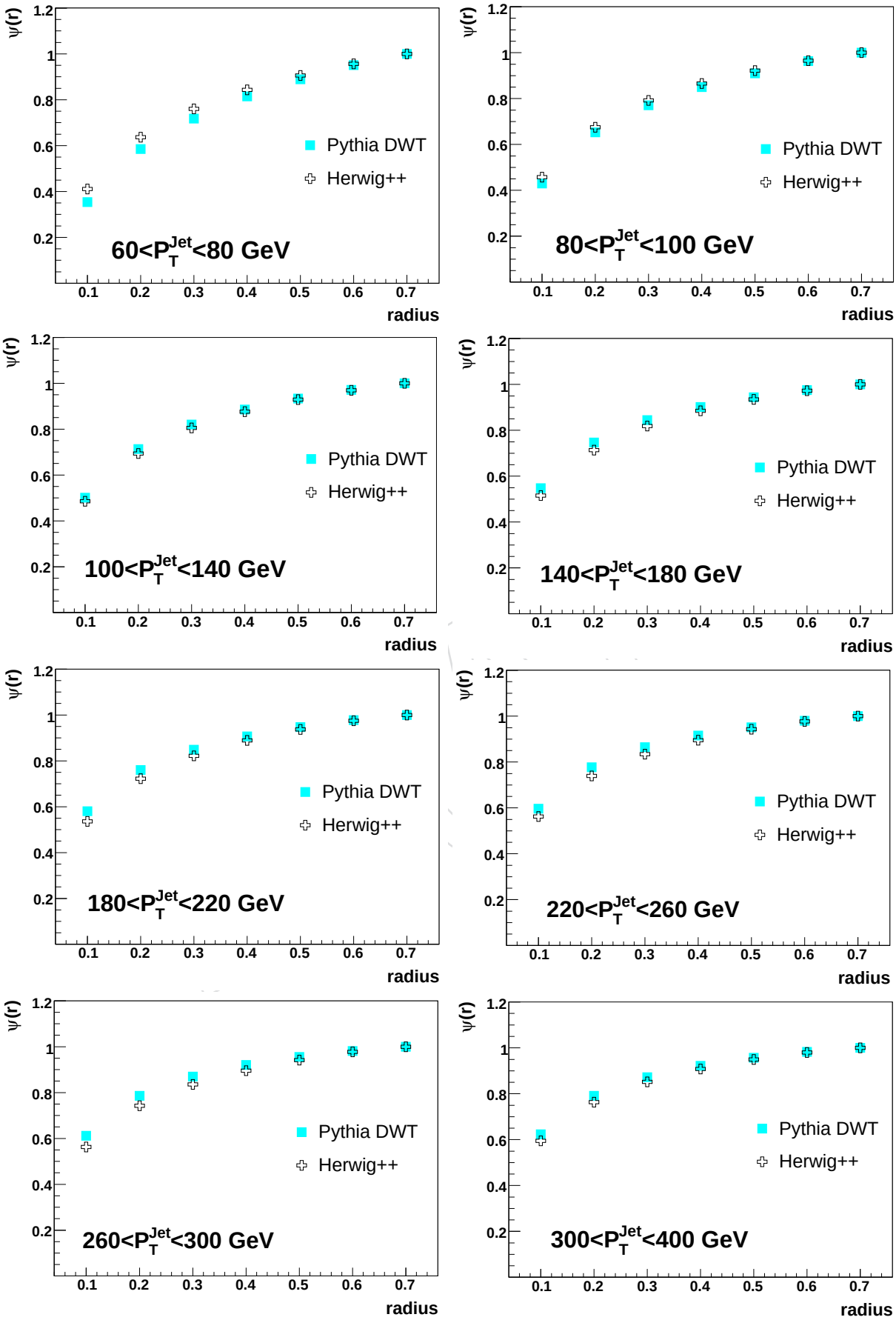

Figure 76: Comparison of particle level integrated jet shapes from HERWIG++ and PYTHIA for selected P_T bins. Statistical errors are included.

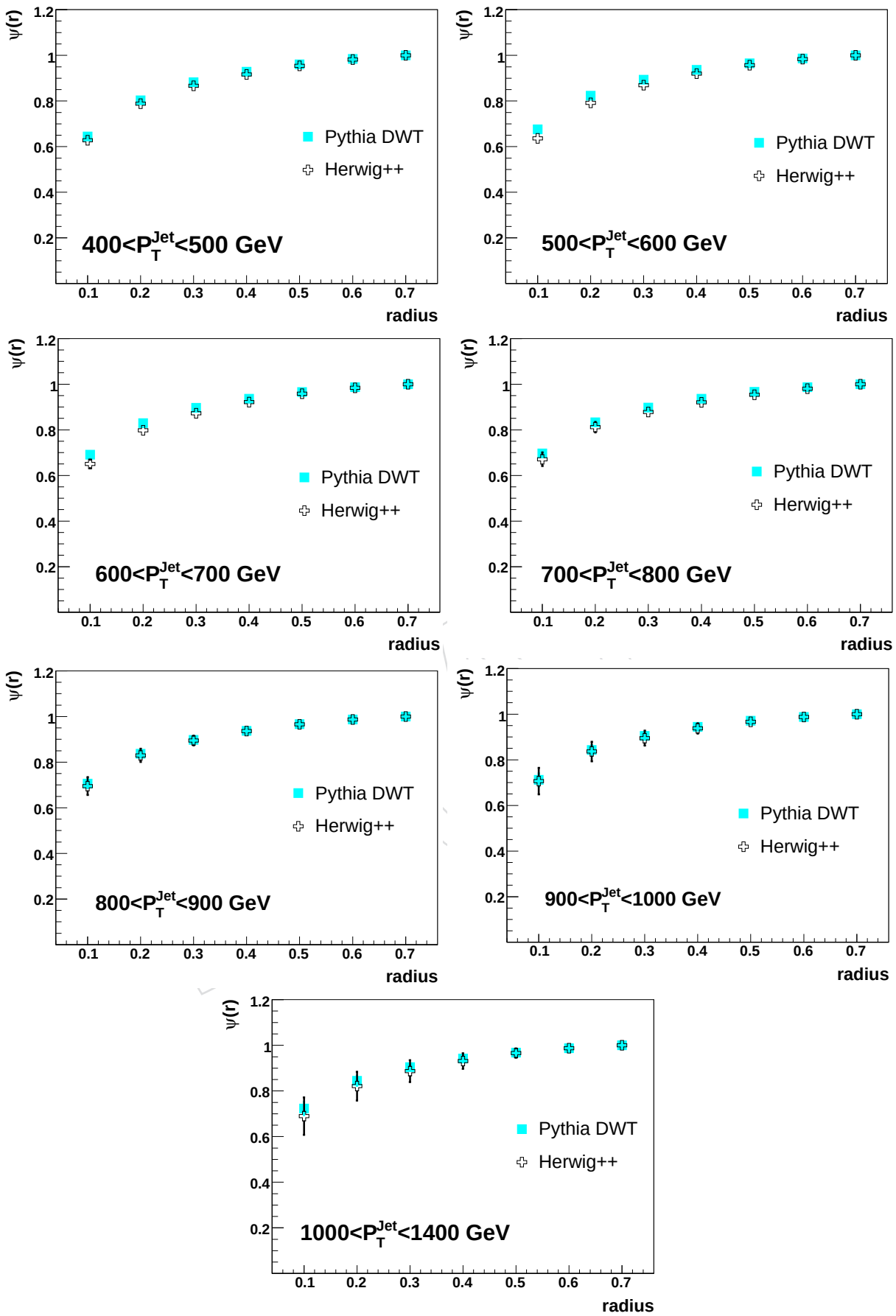

Figure 77: Comparison of particle level integrated jet shapes from HERWIG++ and PYTHIA for selected P_T bins. Statistical errors are included.

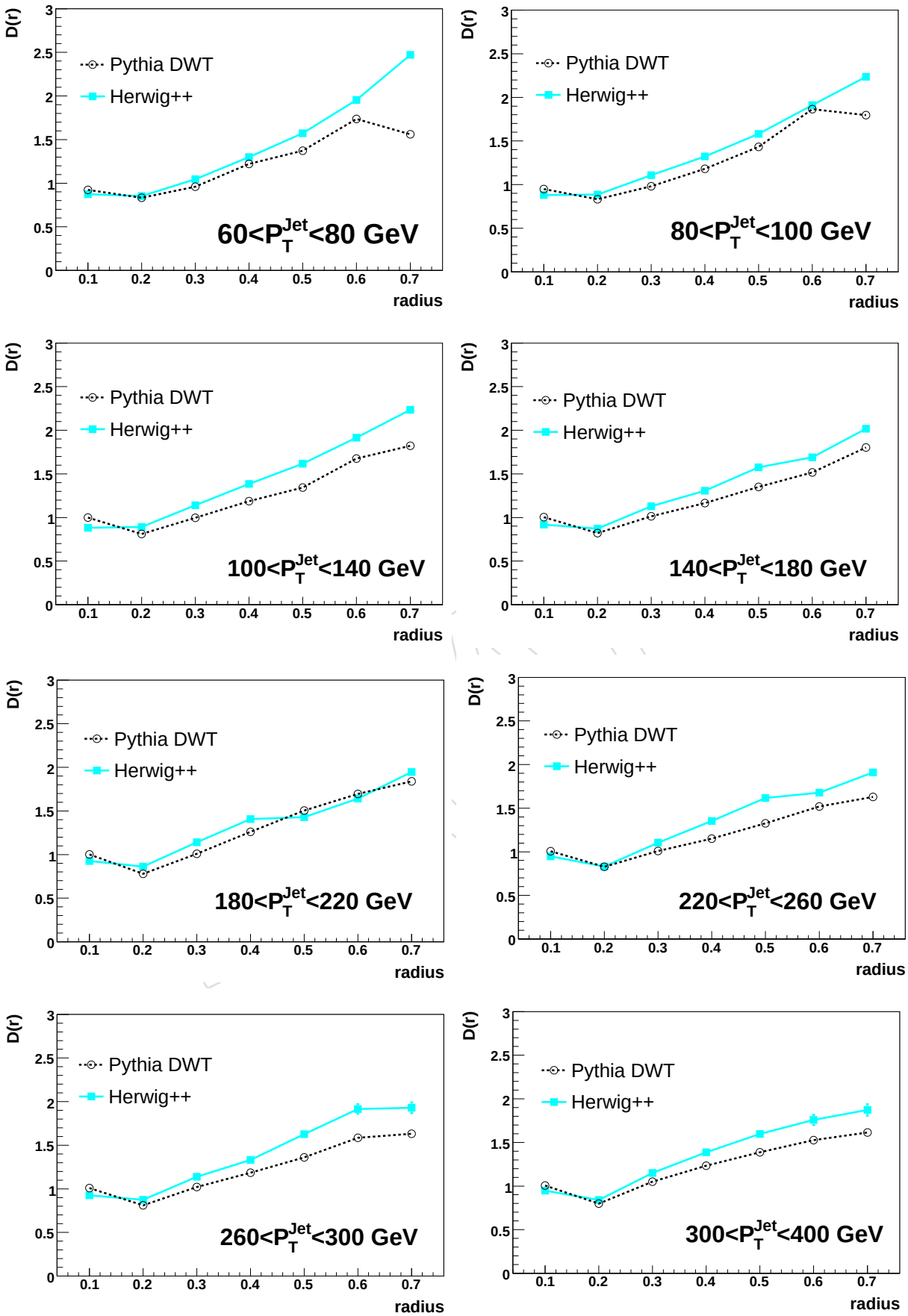

Figure 78: Comparison of the correction factors for differential jet shapes using PYTHIA DWT and HERWIG++. Statistical errors are included.

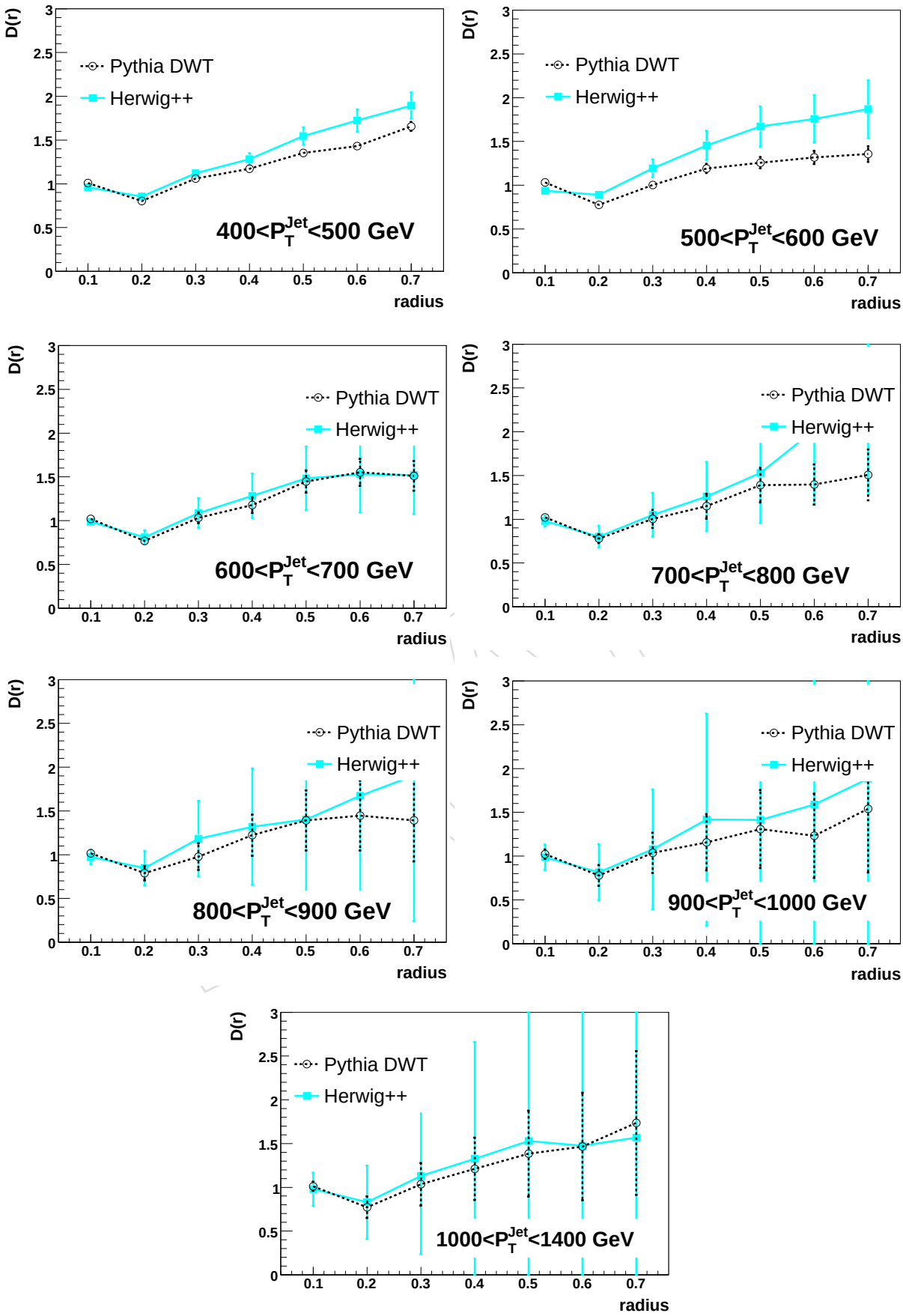

Figure 79: Comparison of the correction factors for using differential jet shapes using PYTHIA DWT and HERWIG++. Statistical errors are included.

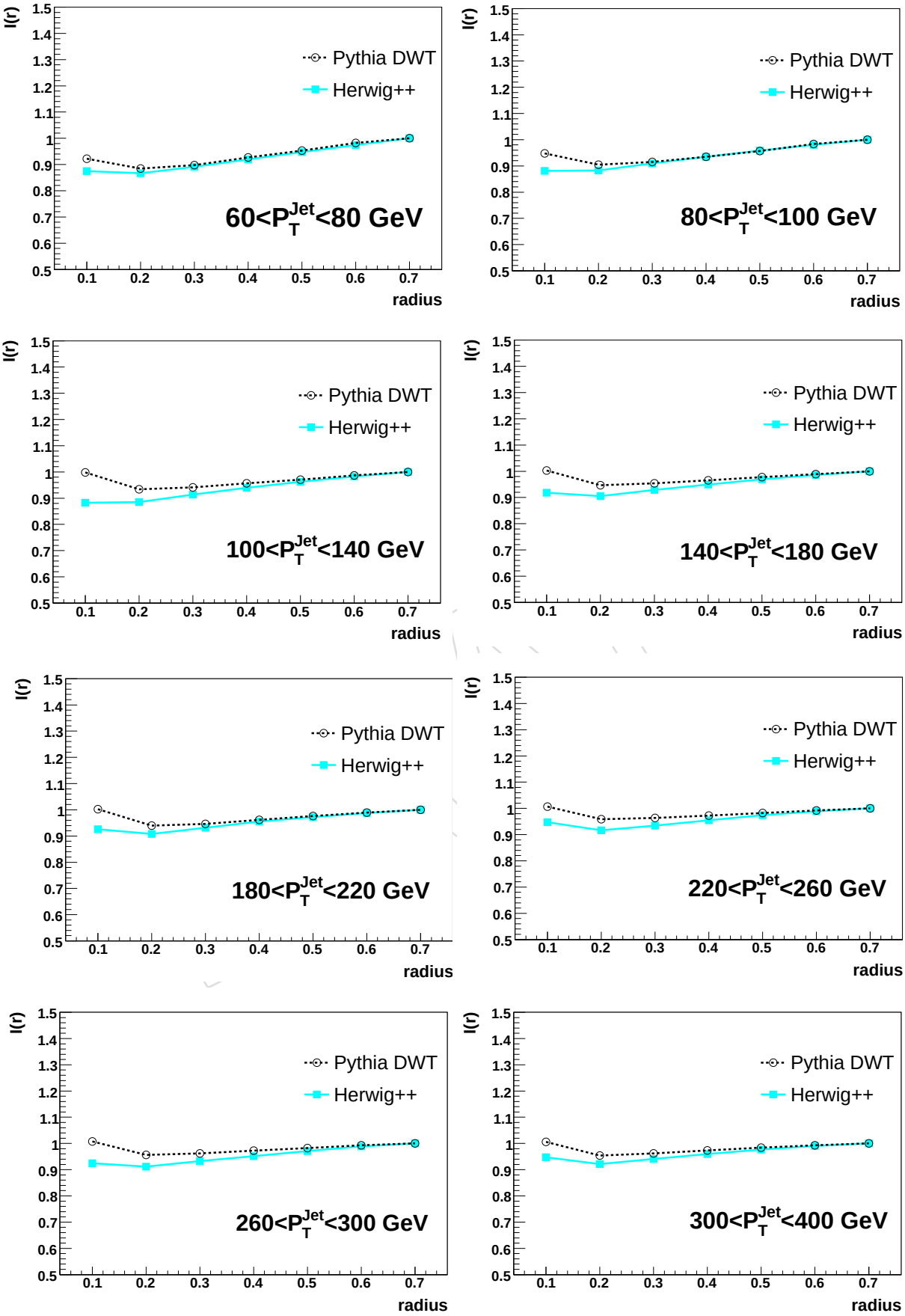

Figure 80: Comparison of the correction factors for integrated jet shapes using PYTHIA DWT and HERWIG++. Statistical errors are included.

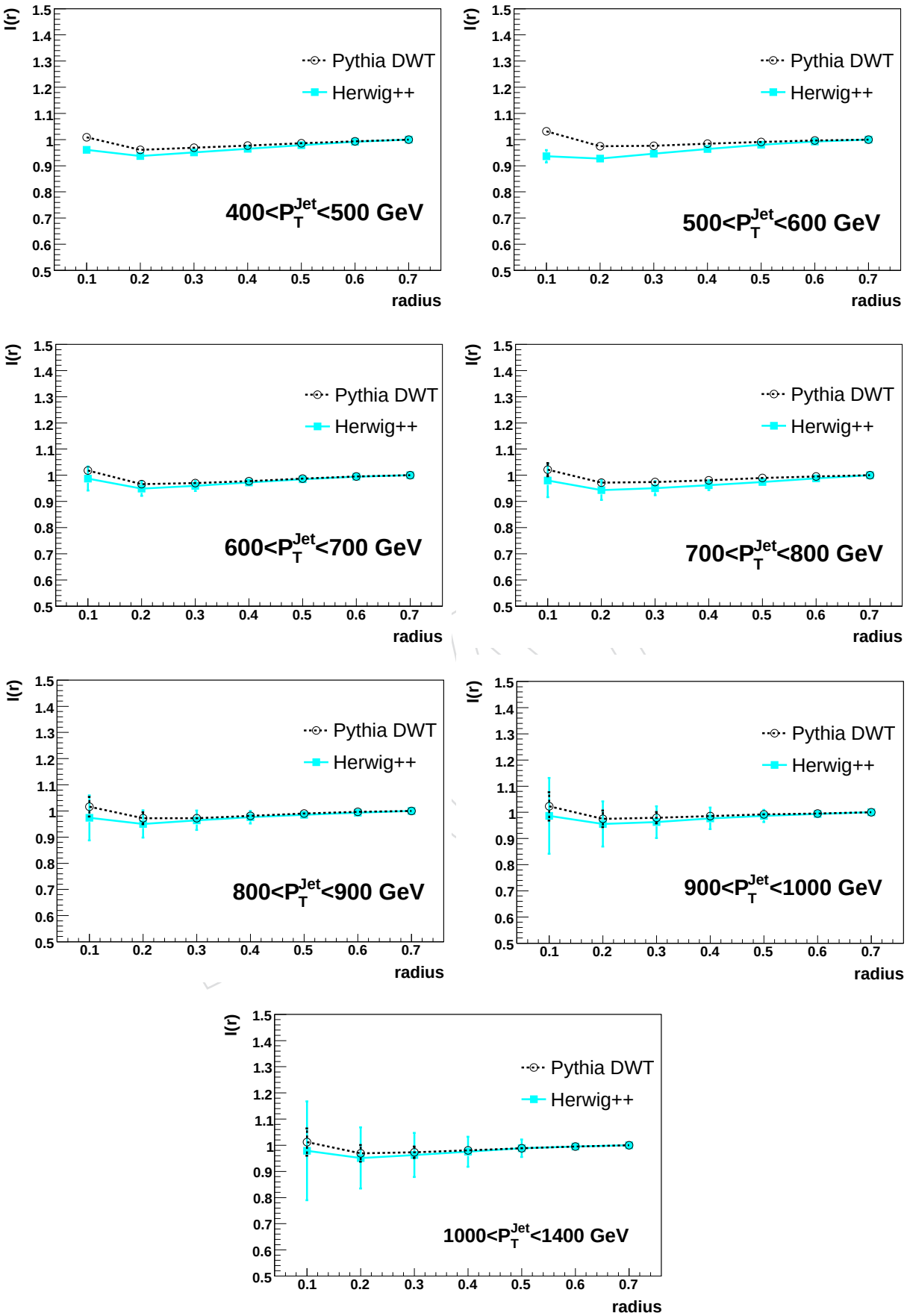

Figure 81: Comparison of the correction factors for integrated jet shapes using PYTHIA DWT and HERWIG++. Statistical errors are included.

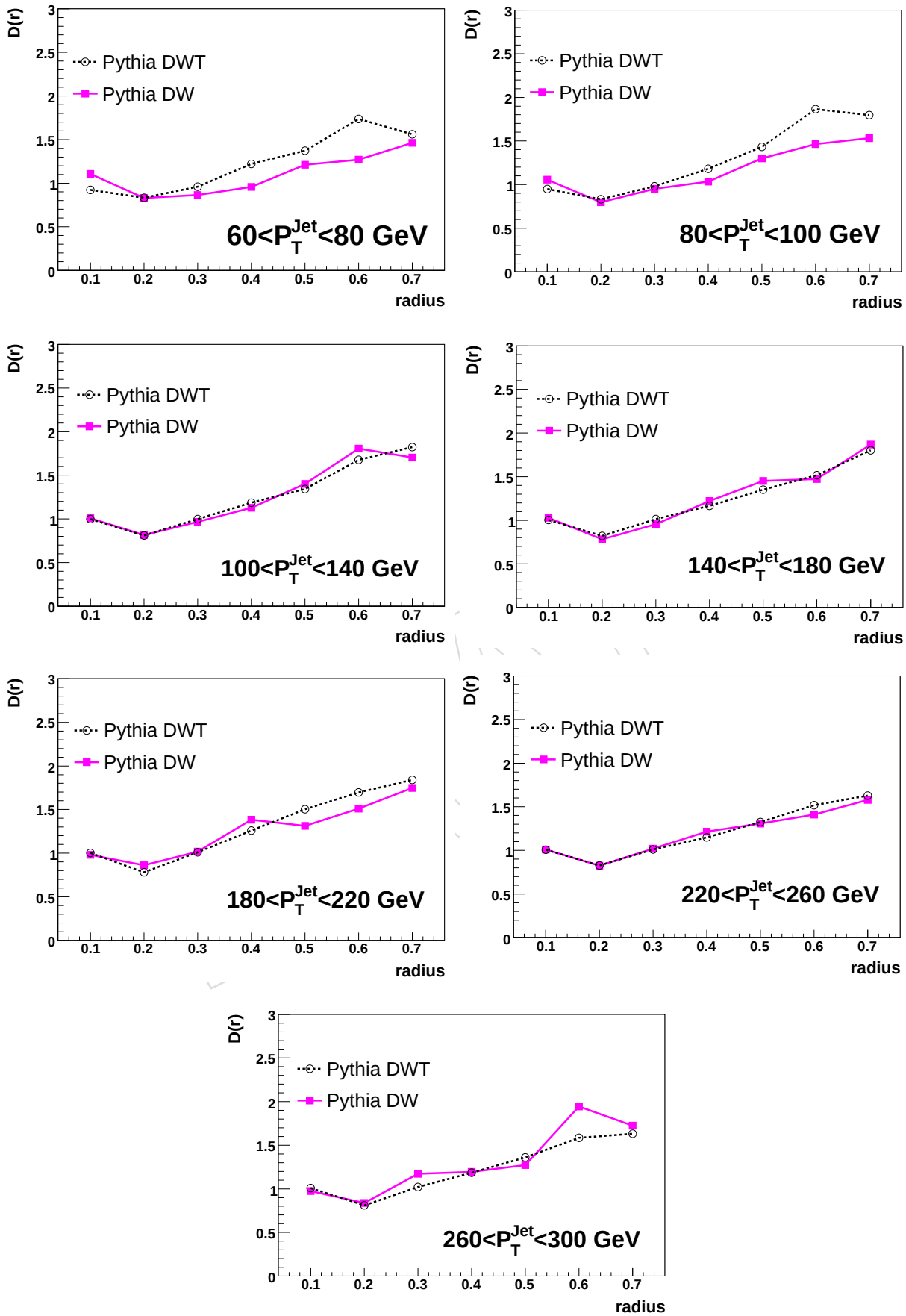

Figure 82: Comparison of the correction factors for differential jet shapes using PYTHIA DWT and DW tunes. Statistical errors are included.

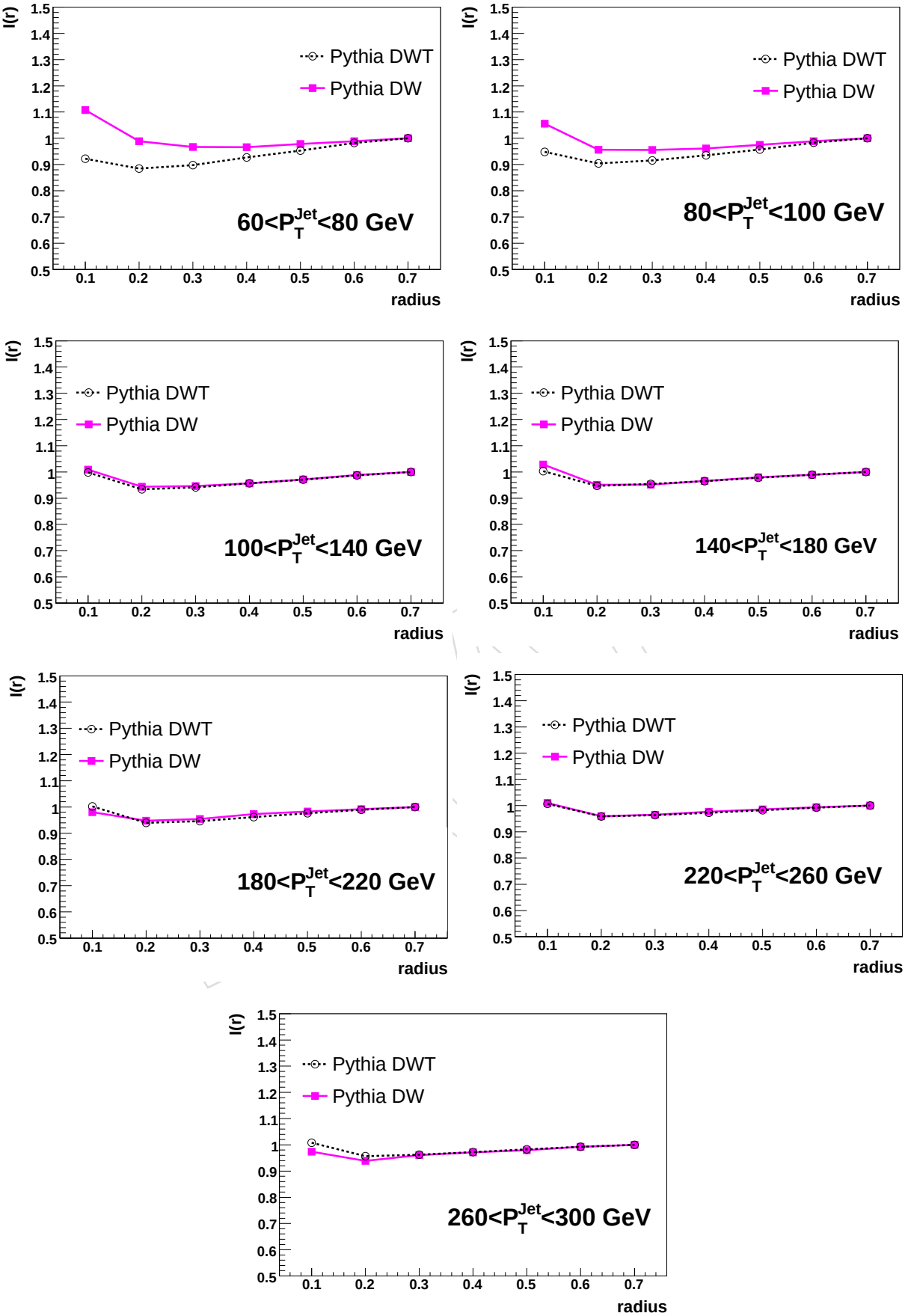

Figure 83: Comparison of the correction factors for integrated jet shapes using PYTHIA DWT and DW tunes. Statistical errors are included.

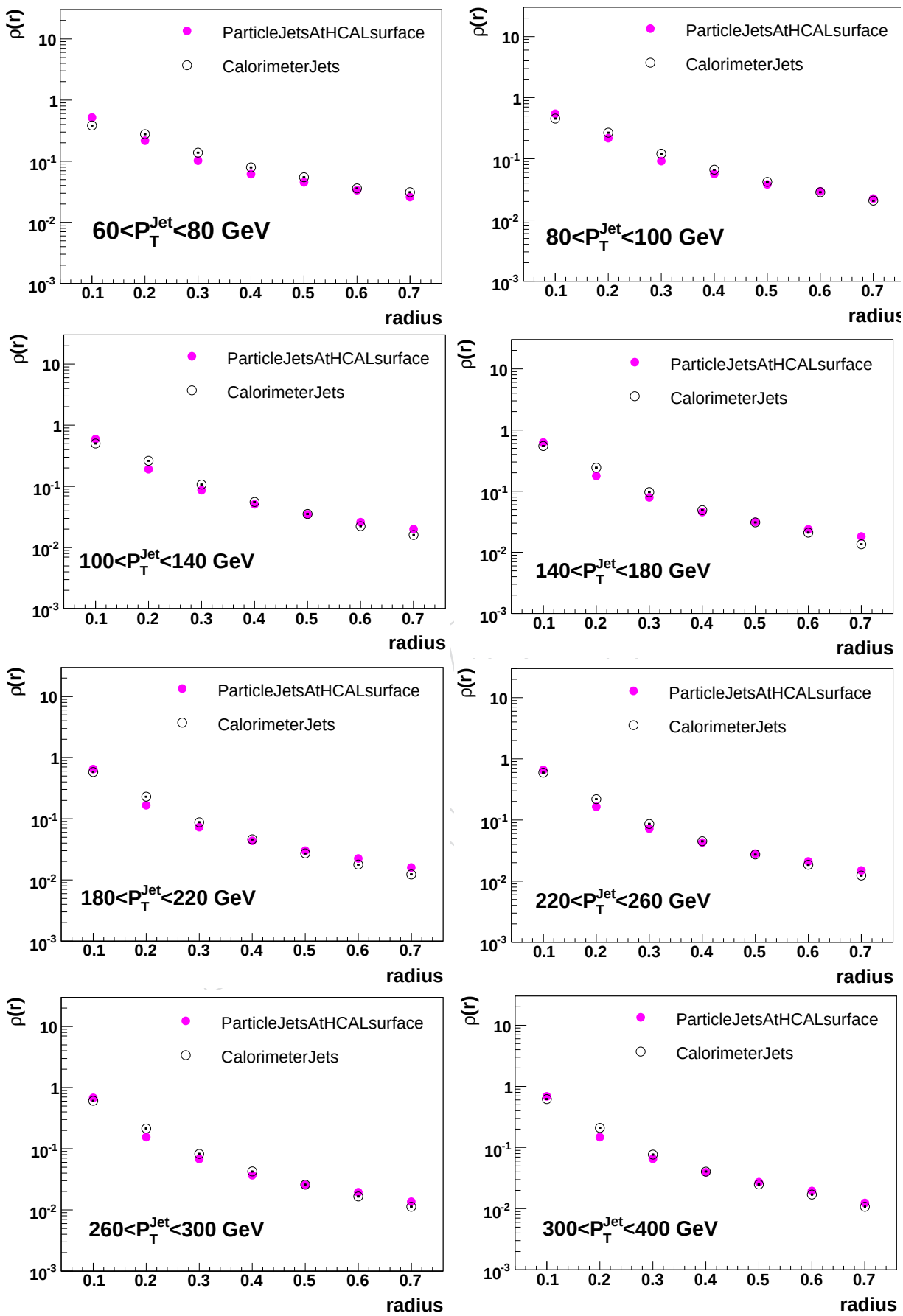

Figure 84: Effect of the transverse showering spread for the differential jet shapes. Only statistical errors are included.

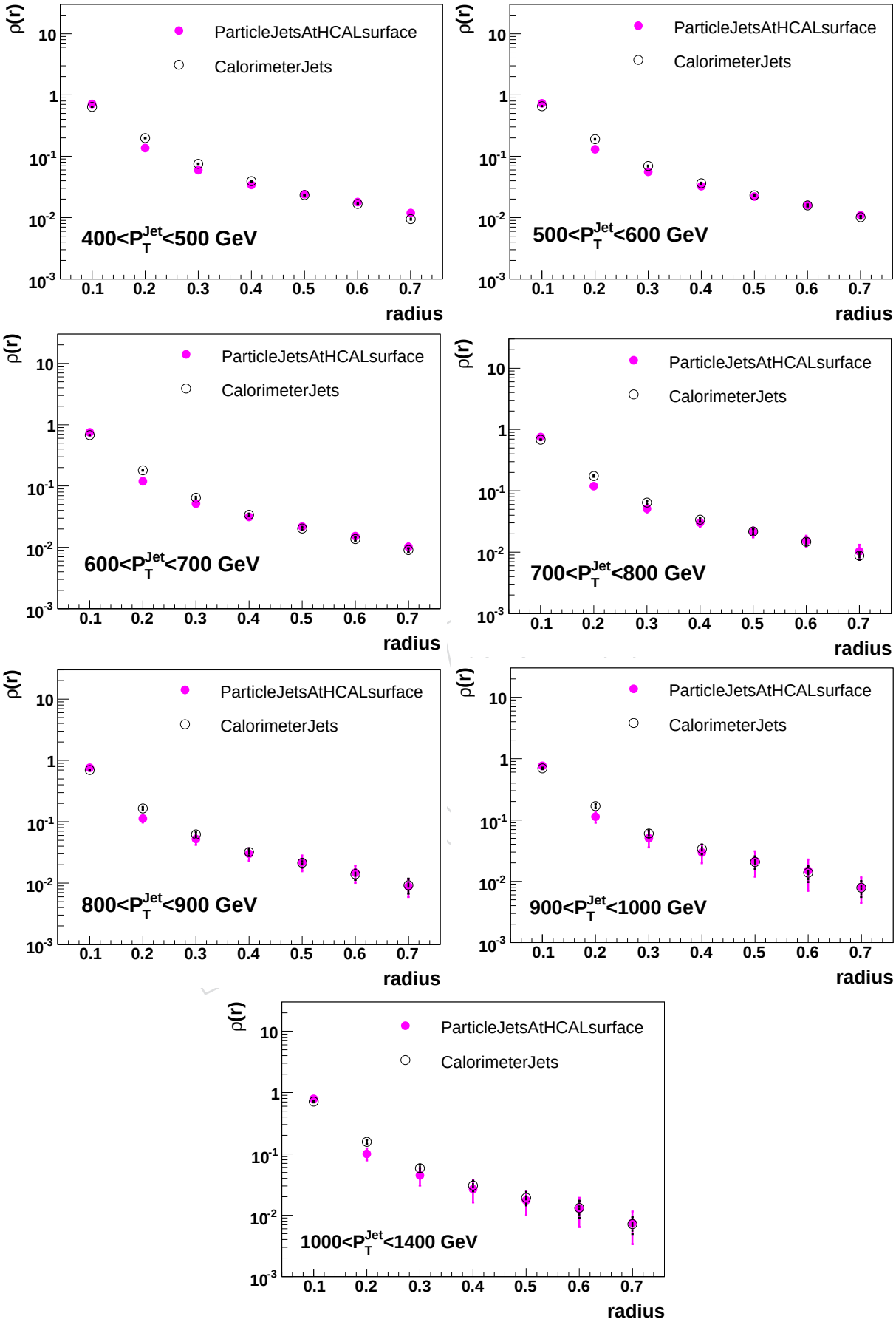

Figure 85: Effect of the transverse showering spread for the differential jet shapes. Only statistical errors are included.

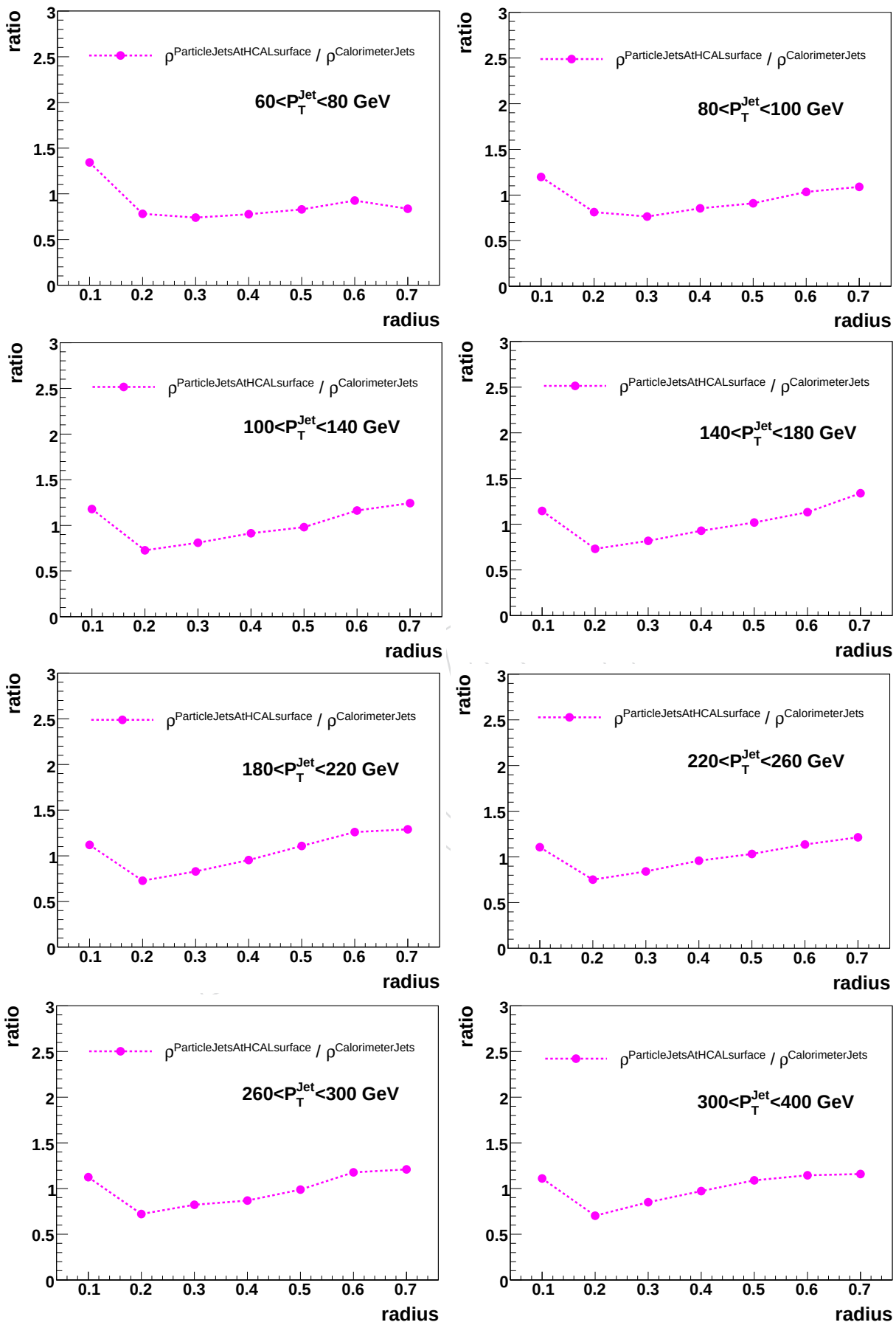

Figure 86: Ratio of the differential jet shapes obtained using parameterized response (without transverse showering) to those from full simulation.

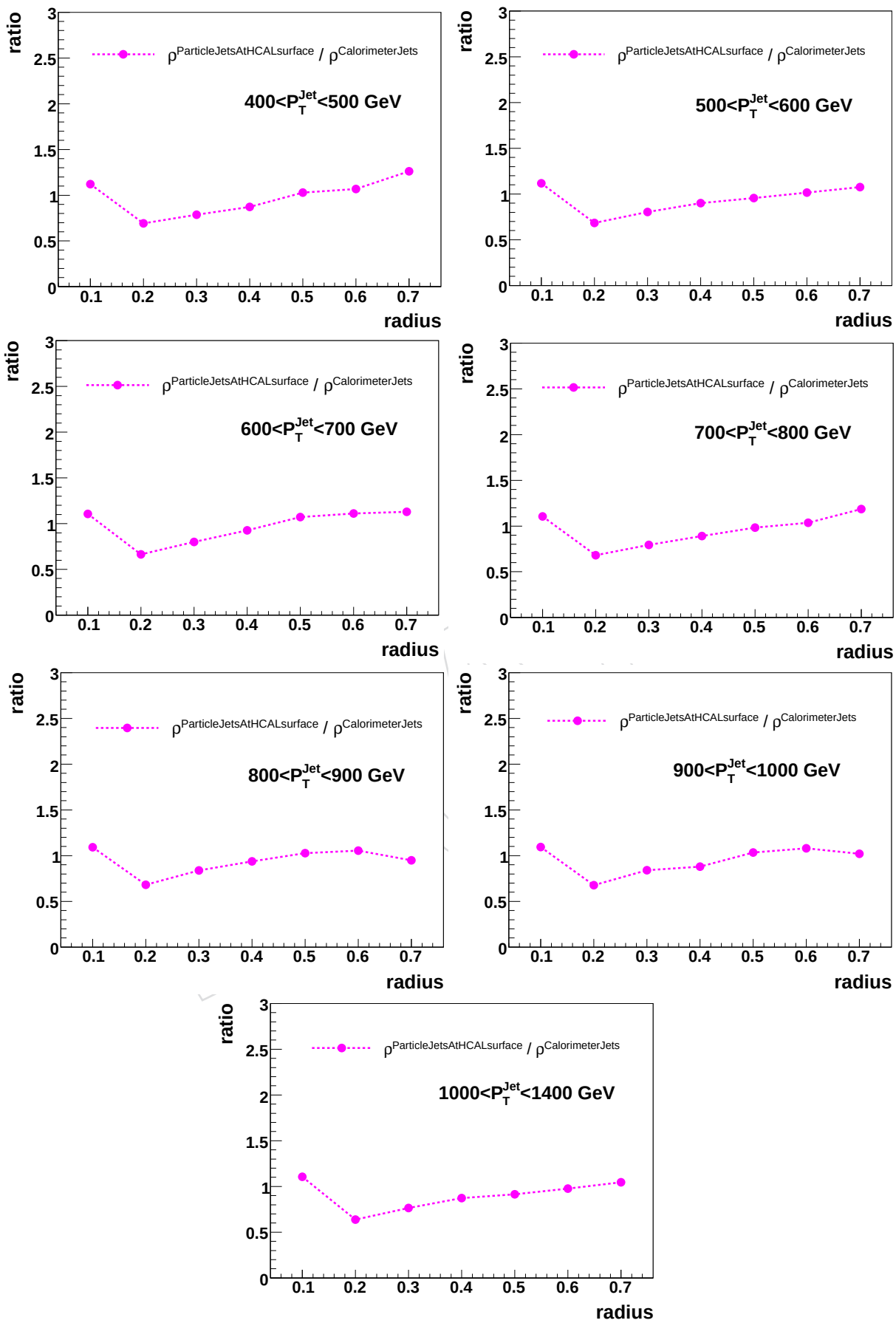

Figure 87: Ratio of the differential jet shapes obtained using parameterized response (without transverse showering) to those from full simulation.

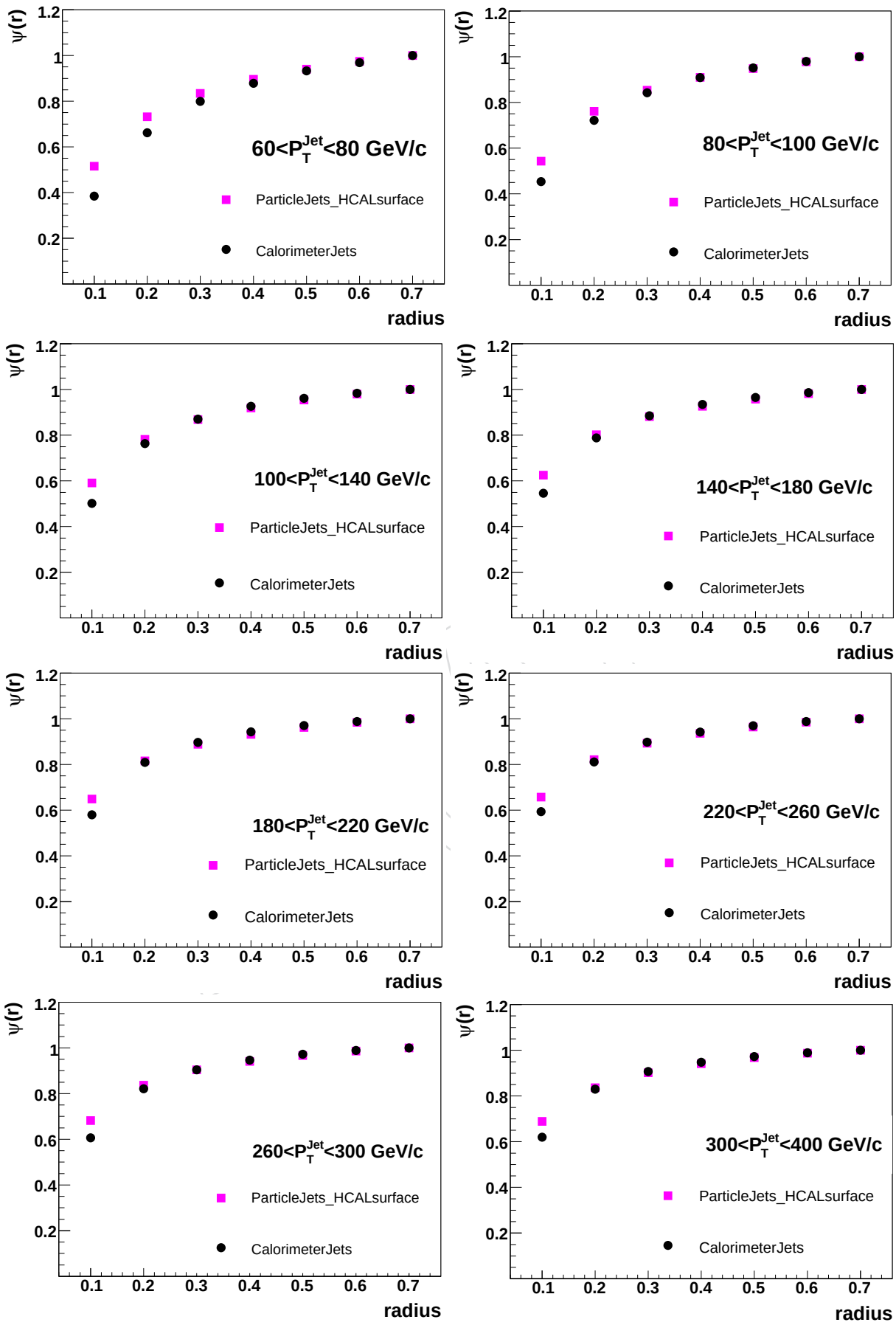

Figure 88: Effect of the transverse showering spread for the integrated jet shapes. Only statistical errors are included.

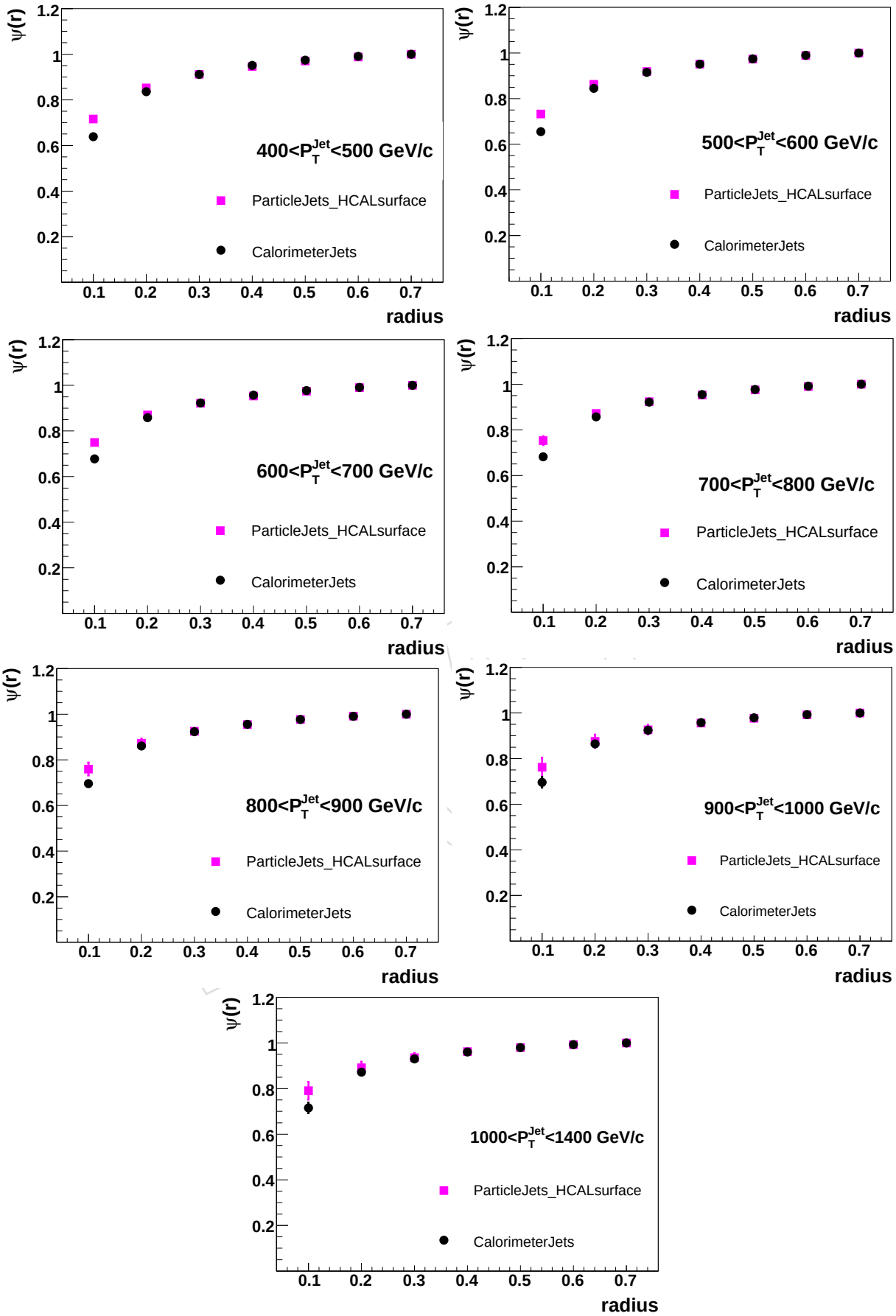

Figure 89: Effect of the transverse showering spread for the integrated jet shapes. Only statistical errors are included.

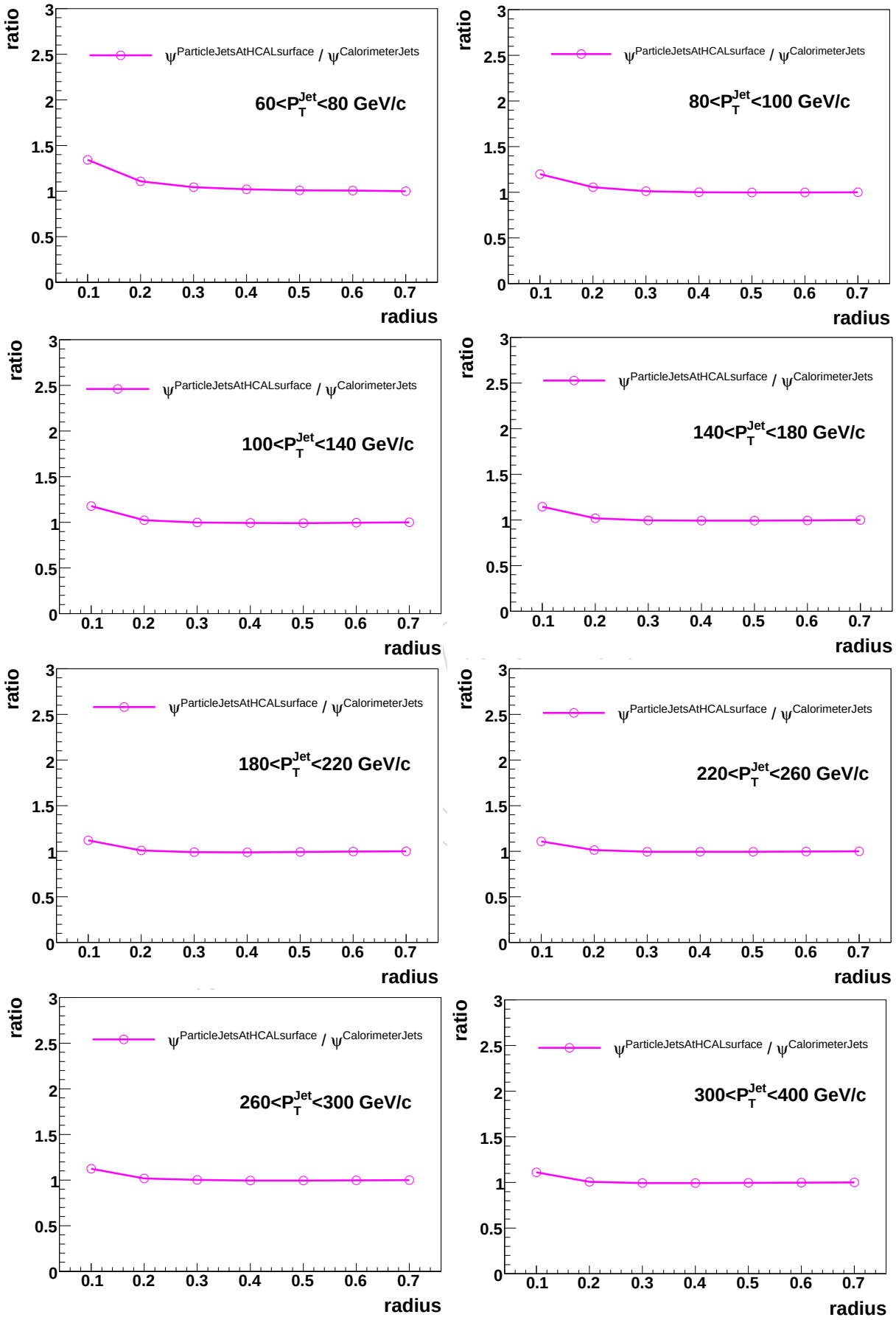

Figure 90: Ratio of the integrated jet shapes obtained using parameterized response (without transverse showering) to those from full simulation.

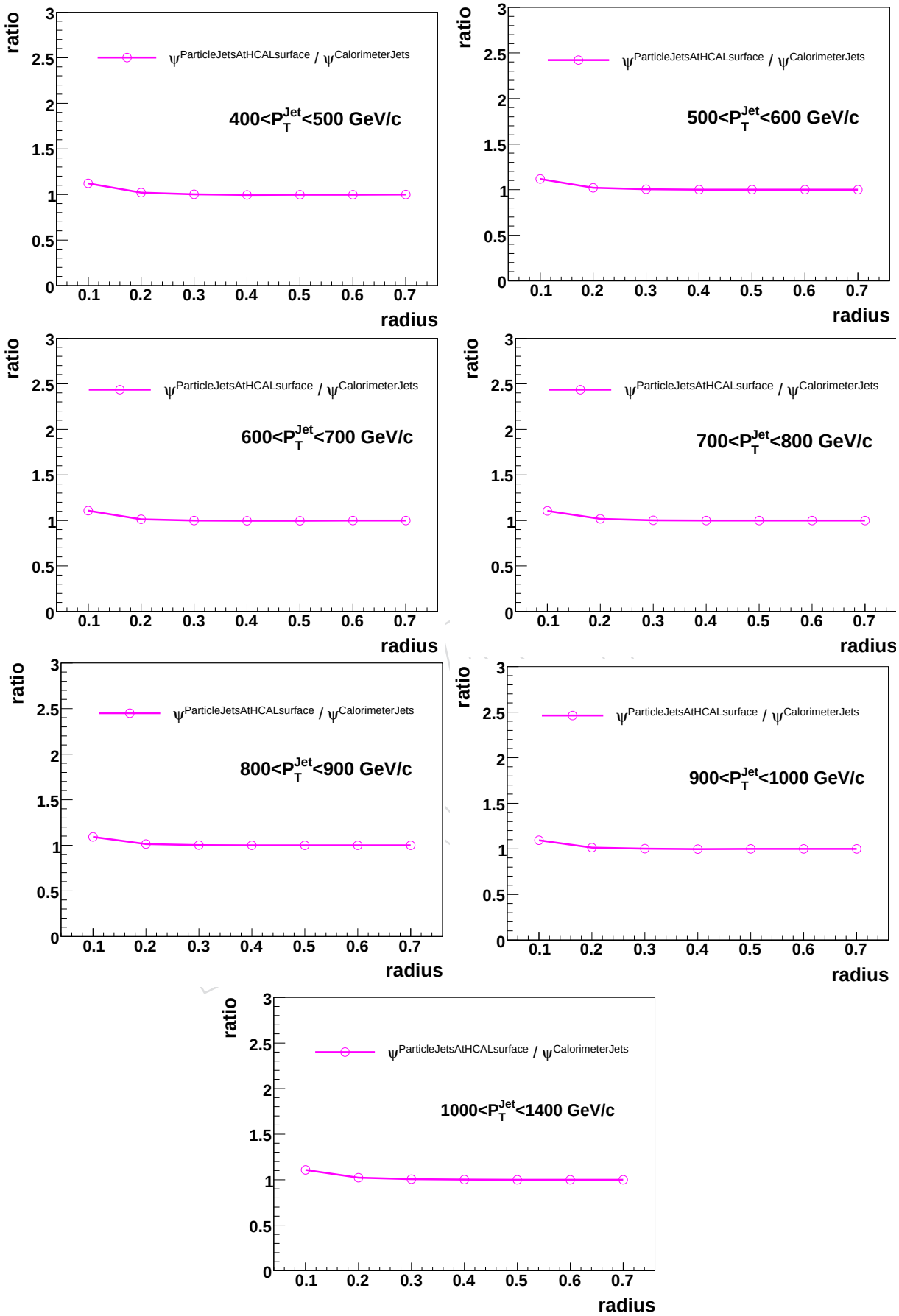

Figure 91: Ratio of the the integrated jet shapes obtained using parameterized response (without transverse showering) to those from full simulation.

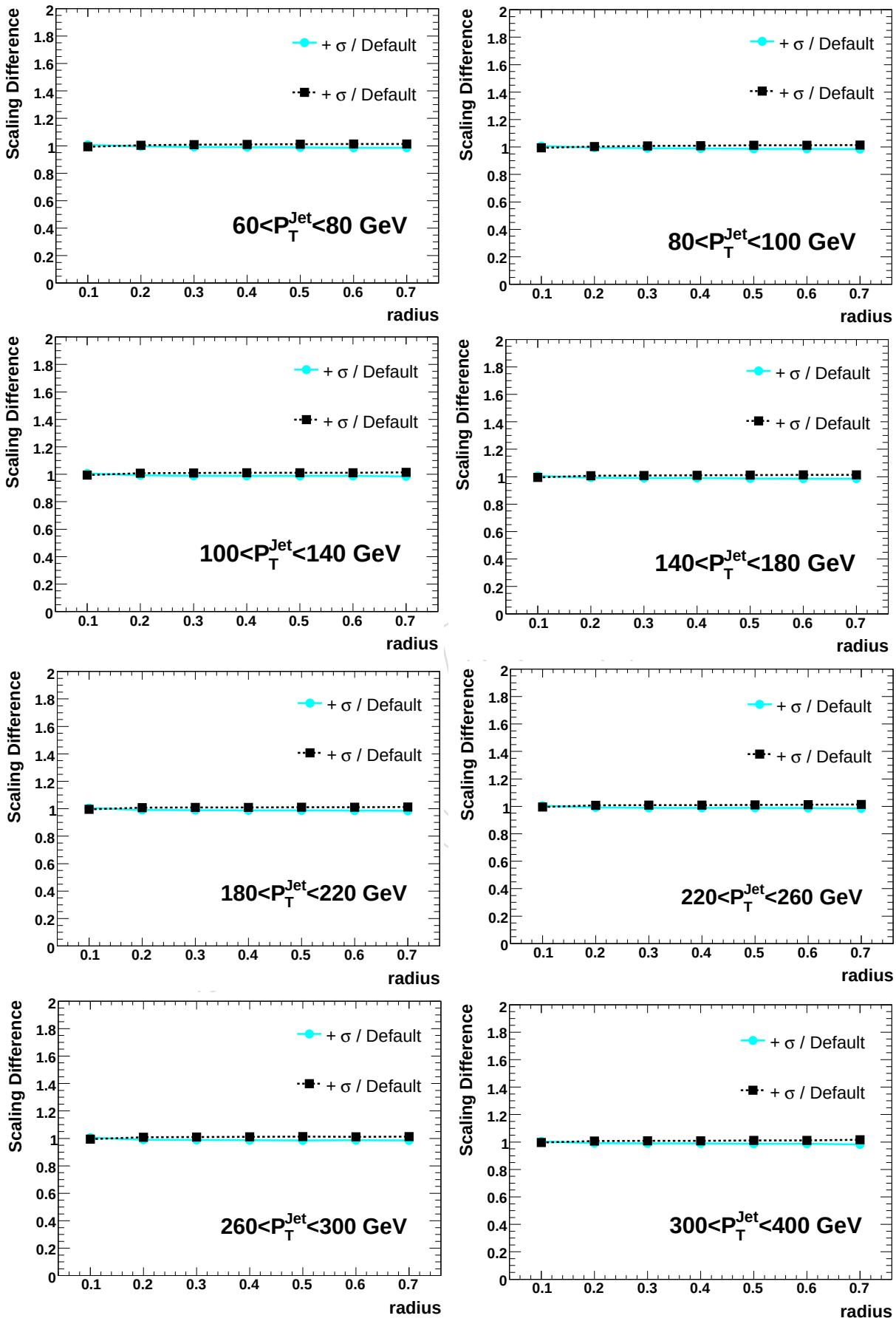

Figure 92: The scaling difference due to $\pm 1\sigma$ variation of E/p for differential jet shapes for selected P_T bins.

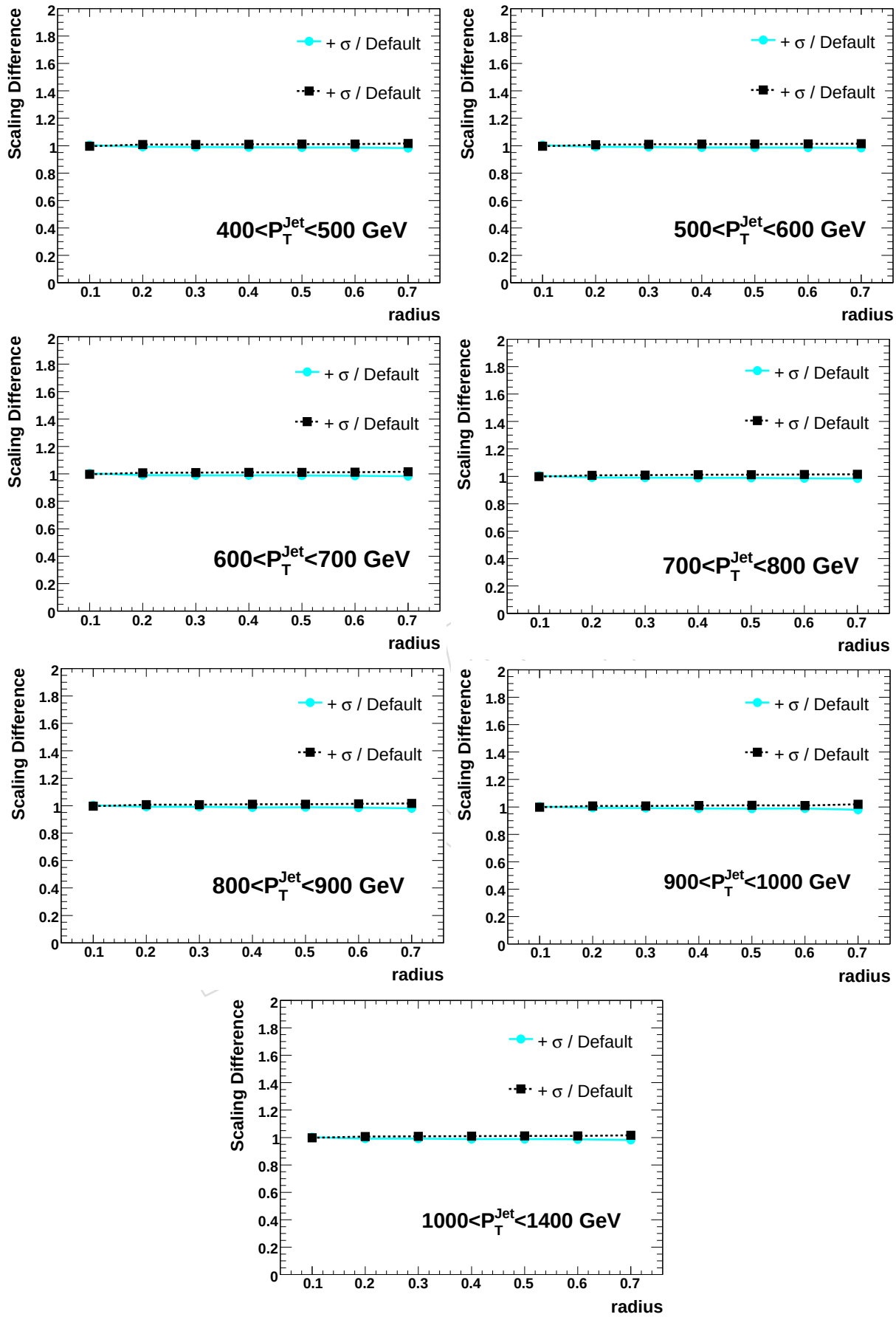

Figure 93: The difference due to $\pm 1\sigma$ variation of E/p for differential jet shapes for selected P_T bins.

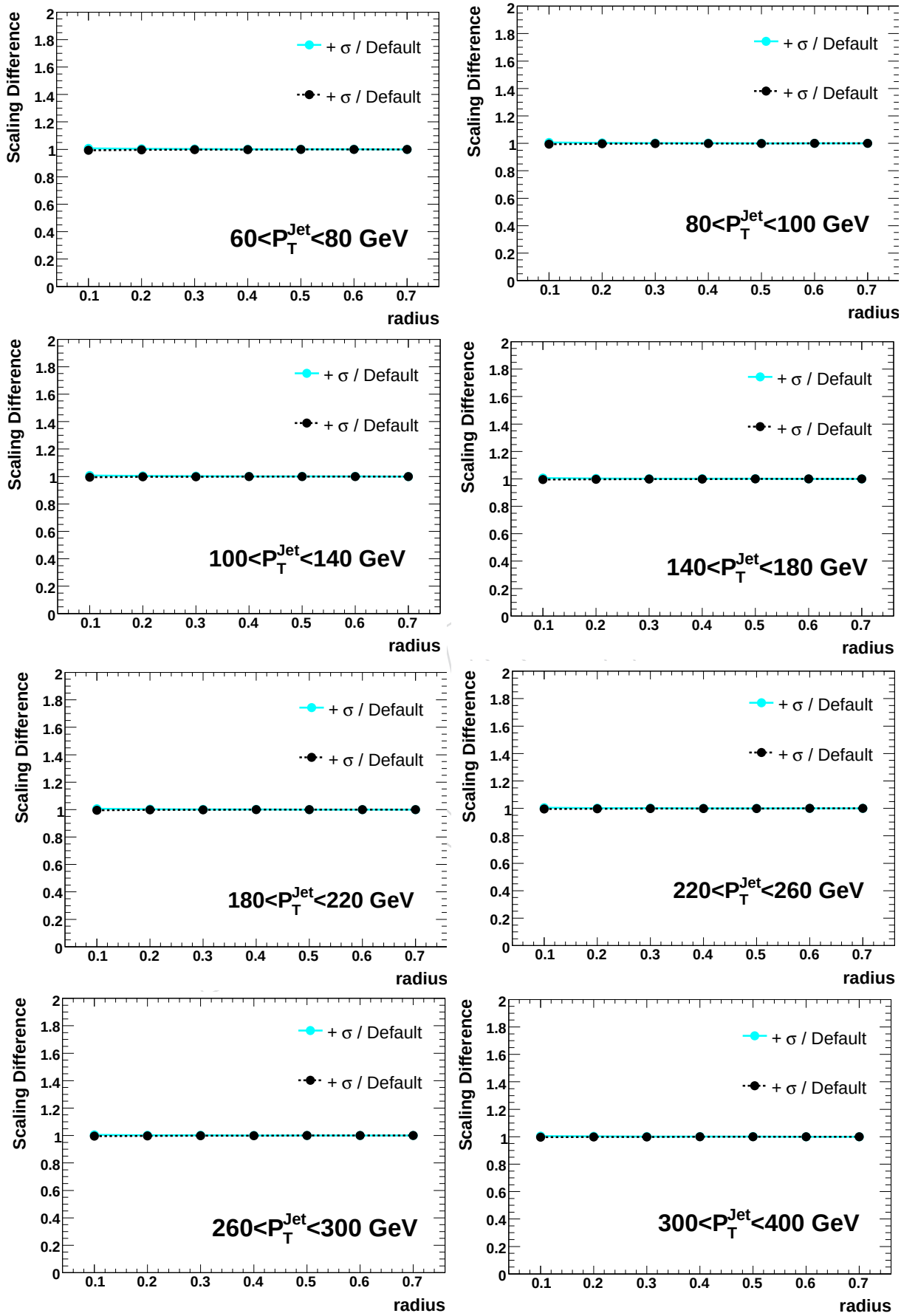

Figure 94: The scaling difference due to $\pm 1\sigma$ variation of E/p for integrated jet shapes for selected P_T bins.

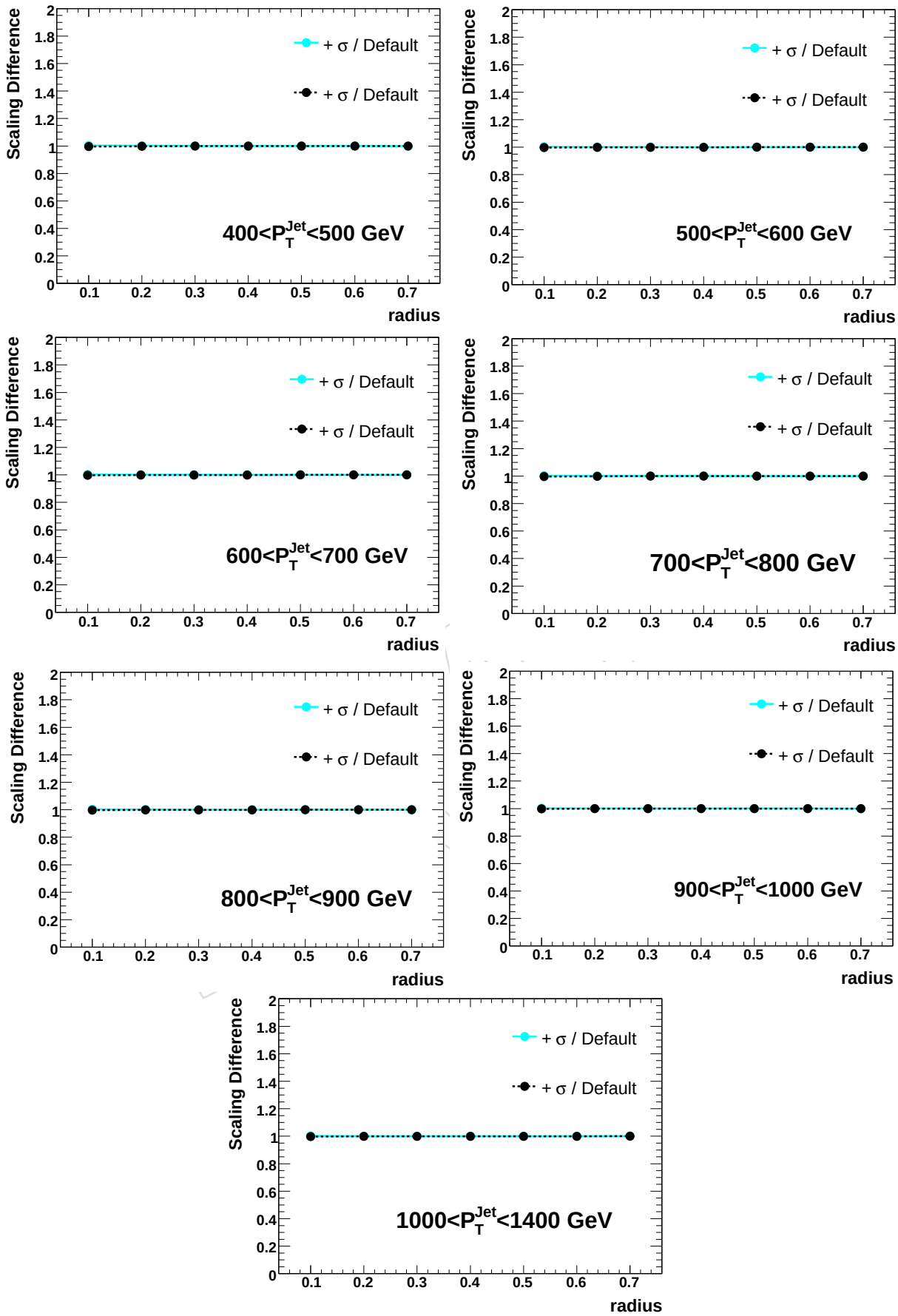

Figure 95: The scaling difference due to $\pm 1\sigma$ variation of E/p for integrated jet shapes for selected P_T bins.